UNIVERSITY OF SOUTHAMPTON

FACULTY OF ENGINEERING, SCIENCE AND MATHEMATICS

Optoelectronics Research Centre

Bragg Grating Filters for Optical Networks

by

Mohd Ridzuan Mokhtar

Thesis submitted for the degree of Doctor of Philosophy

January 2005

DECLARATION OF AUTHORSHIP

I, **Mohd Ridzuan Mokhtar**,

declare that the thesis entitled

Bragg Grating Filters for Optical Networks

and the works presented in it are my own. I confirm that:

- this work was done wholly or mainly while in candidature for a research degree at this University;
- where any part of this thesis has previously been submitted for a degree or any other qualification at this University or any other institution, this has been clearly stated;
- where I have consulted the published work of others, this is always clearly attributed;
- where I have quoted from the work of others, the source is always given. With the exception of such quotations, this thesis is entirely my own work;
- I have acknowledged all main sources of help;
- where the thesis is based on work done by myself jointly with others, I have made clear exactly what was done by others and what I have contributed myself;
- parts of this work have been published as: (*see list of publications*)

Signed: .....

Date: .....

To

Mokhtar Yahya
&
Rabiah Yaacob

Contents

UNIVERSITY OF SOUTHAMPTON

ABSTRACT

Faculty of Engineering, Science and Mathematics

Optoelectronics Research Centre

Doctor of Philosophy

Bragg Grating Filters for Optical Networks

by Mohd Ridzuan Mokhtar

This thesis focuses on the exploitation of fibre Bragg gratings in optical communication networks. New designs, as well as procedures for dynamically altering grating characteristics are proposed for several important functions. We begin with designing gratings for flattening the gain profile of an erbium-doped fibre amplifier. The design process uses an alternative method to the inverse scattering method, but produces a similar spectral response quality. These gratings have either modulated refractive index or chirp rate. Then, we propose a reconfigurable phase-code encoder. The device is composed of a uniform grating, with a number of equidistant fine wires for the purpose of modulating the phase via the thermo-optic effect. Error free data transmission is demonstrated in several optical code-division multiple access architectures. The characteristics of the device are also theoretically modelled. Next, we construct a simple package for continuous tuning of fibre gratings, which adopts the beam bending technique. It demonstrates over 110 nm tuning range and the operational wavelength can be accurately predicted. Its spectral response and limitations are also studied. This device has been incorporated into several optical systems, which include tunable distributed feedback fibre laser, add-drop multiplexer and high power fibre laser. Finally, we present a package for varying the dispersion of a fibre grating. The package deforms a beam into a cubic function shape with a contra-flexure point at the middle. Consequently, this allows changes in the grating delay characteristic without shifting its centre wavelength. This device has achieved dispersion compensation of an 80 km non-zero dispersion-shifted fibre in a 10 Gb/s system. Additionally, since its bandwidth also changes with the stress gradient, it has also been utilised as a bandwidth-variable bandpass filter at the receiving terminal of a spectrum-sliced wavelength-division multiplexed system.

Acknowledgements

It is my most pleasant task to acknowledge the help that I have received from numerous individuals in the writing of this thesis. In particular, I am deeply indebted to Dr. Morten Ibsen for his constant guidance, assistance and understanding. I am also greatly appreciative of Prof. David J. Richardson for his generous support, technically and financially. I thank my colleagues Dr. Peh Chiong Teh, Dr. Libin Fu, Mr. Micheal Roelens, Dr. Fabio Ghiringhelli, Dr. Benn Thomsen, Mrs. Anoma McCoy, Mr. Paulo Almeida, Mr. Zhaowei Zhang, Mr. Albert Canagsanay, Miss Nyuk Yoong Voo and Mr. Raja Kamarulzaman Raja Ibrahim for many enlightening discussions and stimulating collaborations. I humbly acknowledge the vast assistance from Mr. Simon Butler and Mr. Timothy McIntyre. A special thank to Mrs. Eve Smith for her friendly help and administrative support throughout my study. I am also indebted to Dr. Eleanor Tarbox for her advice and constructive comments on this thesis. Not to forget, everybody within the ORC who has helped me directly or indirectly with my study. Thanks also to my housemates Dr. Fazly Salleh Abas, Dr. Yusoff Alias, Dr. Zulfadzly Yusoff, Dr. Mohammad Faizal Ahmad Fauzi and Mr. Jeffry Mohamad Noor, Dr. Hafizal Mohamad and his family, my fellow MMU colleagues and the whole Malaysian community that have made me feel like home here. I acknowledge the support of MARA for their studentship and my employer MMU for granting my study leave. Last but not least, my utmost gratitude to my parents and sisters for their love and support.

Abbreviations

ADM	Add-Drop multiplexer
ASE	Amplified spontaneous emission
ASK	Amplitude-shift keying
BER	Bit-error-rate
BPSK	Bipolar phase-shift keying
BW	Bandwidth
CW	Continuous wave
dB	Decibel
DBR	Distributed Bragg reflector
DCF	Dispersion compensating fibre
DFB	Distributed feedback
DGD	Differential group delay
DS-OCDMA	Direct sequence optical code-division multiple access
EAM	Electro-absorption modulator
EDFA	Erbium-doped fibre amplifier
EOM	Electro-optic modulator

eV	Electron volt
FBG	Fibre Bragg grating
FH-OCDMA	Frequency hopped optical code-division multiple access
FM	Frequency modulation
fs	Femtosecond
FWHM	Full width at half maximum
Gb/s	Giga bits per second
GFF	Gain flattening filter
GHz	Gigahertz
GVD	Group velocity dispersion
ISI	Inter-symbol interference
kHz	Kilohertz
km	Kilometre
mm	Millimetre
ms	Millisecond
NA	Numerical aperture
nm	Nanometre
NOLM	Non-linear optical loop mirror
ns	Nanosecond
OCDMA	Optical code-division multiple access

PDL	Polarisation dependent loss
pm	Picometre
PMD	Polarisation mode dispersion
ps	Picosecond
PSK	Phase-shift keying
QPSK	Quaternary phase-shift keying
rad	Radian
RF	Radio frequency
RZ	Return to zero
SNR	Signal-to-noise ratio
SOA	Semiconductor optical amplifier
SSFBG	Superstructure fibre Bragg grating
TDM	Time-division multiplexing
UV	Ultra violet
WDM	Wavelength-division multiplexing
μm	Micrometer
μs	Microsecond

Chapter 1

Introduction

1.1 Overview

The first observation of permanent periodic change of the refractive index in an optical fibre in 1978 [1] marked the beginning of a significant breakthrough in optical telecommunication and sensor system development. This historical discovery of the fibre Bragg grating (FBG) has triggered exhaustive studies in an attempt to understand the foundation of fibre photosensitivity. Concurrently, these activities inspire the FBG fabrication technology, which over time has advanced to the point where complex grating structures are now feasible [2]. The flexibility offered in the design and fabrication of FBGs lays down broad and important roles in various applications that concern optical systems. FBGs may well perform the same functions as the existing alternative devices or become the enabling devices of various formerly impractical technologies. Evidently, FBGs have been recognized as key components in modern optical telecommunication systems [3]. Nevertheless, conventional FBGs and their related devices are not entirely compatible with future optical architectures, which often demand dynamic components to enable reconfigurable traffic networks. On these accounts, we dedicate this research to utilise FBG technology to enhance system performance and possibly acquire tunability in novel devices, thus assuring their place in the future optical telecommunication systems.

We intend to begin by identifying a number of potential aspects in a wavelength-division multiplexed (WDM) system in which FBG technology can be adopted to enhance the performance and capacity of the system. Subsequently, we will propose novel devices with all efforts focussed to incorporate dynamic features to those devices by exploiting the physical natures of a fibre. Reliability,

simplicity and cost are taken as the prime attributes of these devices. All devices will also be theoretically analysed to facilitate prediction of their responses and therefore allowing them to be tailored to a desired design. The theoretical analyses will be verified through characterisations of the proposed devices. Positive preliminary tests on the devices will then proceed with demonstrations in applicable systems to validate their reliability.

Our research lays emphasis on WDM as it is currently the most viable solution to the congestion on installed optical fibre in long distance links. WDM relieves the need to overlay new fibre cables as new channels are added by simply extending the information bandwidth. Transmission of these channels over thousands of kilometres is made possible only by the support of fibre amplifiers. The channels will have to traverse through a cascade of erbium-doped fibre amplifiers (EDFAs), in which each intrinsically has a non-uniform gain spectrum. Consequently, this will cause variation in the signal-to-noise (SNR) performance of the relayed channel signals. Various approaches to fix this critical problem have been reported, involving tweaking the operating conditions or geometry [4-9], alteration of material compositions of the fibre amplifier [10, 11] and the use of loss-inducing filters [12-21]. However, the first two approaches can still produce noticeable gain variation of several decibels. The latter approach includes a range of filter types, among which the FBG appears as the most elegant device. Nevertheless, a circulator is required in this configuration and its dispersion characteristic must be managed attentively. We propose the use of a FBG as a gain equalising transmission filter to alleviate these inconveniences. The FBG can be readily spliced in line with the isolator that is always incorporated in a reputable EDFA, thus minimizing insertion loss and preventing stray reflection feedback. In-band chromatic dispersion is completely avoided as the signals do not experience distributed reflection in this configuration. Refractive index or period modulation may be manipulated to yield the necessary losses to equalise and enhance the maximum bandwidth of EDFAs.

We also consider optical code division multiple access (OCDMA) as an overlaying means to attain larger capacity transmission. Technologies comprising waveguides with delay lines [22] or phase shifters [23] and an arrayed waveguide

grating (AWG) [24] have been utilised for realising this type of system. Despite the impressive demonstrations, grating technology is effortlessly identified to be well applicable of this performance using cascades of FBGs [25-27] and superstructured FBGs [28]. However, some of the technologies which showed tunability, display lack of compactness and possess high fabrication complexity and cost. On the contrary, we aim to fashion OCDMA signals by simply introducing impermanent phase shifts to the information-bearing lightwaves that are being spatially dispersed by a weak uniform grating. We expect that this will result in duplications of each signal pulse into a sequence of bits with embedded phase codes, thus signifying a unique channel. We propose to use the thermo-optic effect for changing the phase of each bit, which can be easily induced by a fine electrical heating element. We intend to present thorough characterisations both theoretically and experimentally for this novel device to accurately perform its designed function. This may well proceed with deployment of the device in experimental OCDMA systems to illustrate its prospective performance.

Optical add/drop multiplexers essentially define a WDM system. Clearly, having these components tunable will enable flexible traffic management. There are many types of filter such as dielectric thin-film, Fabry-Perot and acousto-optic filters [29], yet FBG prevails over all competing technologies as it exhibits impeccable spectral characteristics as well as compactness. Tunability of FBG filters has been successfully demonstrated which was principally achieved through application of axial strain using a large and complex assembly [30-32]. In contrast, we wish to design a truly simple and compact tuning package for a FBG which also require no electrical power to remain at a chosen operating condition. We are determined to ensure the preservation of the FBG pristine characteristics for all operating wavelengths. In order to shift the reflection spectrum, we utilise the beam bending technique [33] for applying the elasto-optic effect onto the FBG. In view of the fact that the signals' wavelength window is diffusing into the short (S-band) and long (L-band) wavelength regions, we aim to achieve the widest ever tuning range for a fibre filter. Additionally, detailed characterisations of the device in operation will be acquired.

Light pulses inevitably experience chromatic dispersion in single-mode fibres. This causes severe system penalties when engaging high data rate transmission in long haul fibre links. Typically, the distortion is corrected by using long lengths of dispersion-compensating fibre [34]. It has been shown that compensation is also achievable by using various types of interferometers [35-38], expensive optical phase conjugators [39] and complicated electrical signal processing [40]. Nevertheless, the FBG offers a more compact solution in which it can exert frequency dependent delays to the reflected spectral components [41]. It has assisted in the demonstration of a long distance WDM transmission of up to 8×20 Gb/s [42]. Nonetheless, some long-haul transmission links employ a ring configuration in order to cope with cable failure. At the time of breakdown, the light signals will be automatically re-routed to a different optical path. Consequently, they are broadened by a different magnitude of dispersion. Likewise, in reconfigurable systems where channels are added at various locations along the optical links, the receiving terminal will thus see differently broadened channels. In both aforementioned circumstances, a tunable dispersion compensator becomes a necessity to allow real time adjustment. We again propose to impose the elasto-optic effect via mechanical means to shape the time delay property of a FBG for compensating varying second-order dispersion. The device will be fully characterised and its performance in compensating dispersion of single-mode fibres will be assessed.

1.2 Organisation of the Thesis

The following part of this Chapter gives a concise fundamental background of fibre Bragg gratings that is relevant to the research and summarises the main concepts of the numerical tools used for device simulations. In the next Chapter, we propose several gain-flattening filters based on fibre Bragg gratings operated in transmission. These devices have either a modulated period and a uniform refractive index change, or a uniform period and a modulated refractive index change. Their performances are theoretically analysed through extensive simulations using the transfer matrix method. Any possible improvements to the design are also investigated and theoretically demonstrated.

We have also devised a phase encoder/decoder based on a uniform fibre Bragg grating. Detailed construction of the device is described in Chapter 3. This device has been deployed in several system configurations to demonstrate its reliability in code generation and recognition. The test systems range from a simple code-decode setup to an advanced bi-lateral coherent optical code-division multiple access system with add/drop capability. The device performances are assessed through the auto-/cross-correlation traces and bit-error-rate measurements. This Chapter also presents the results obtained from multi-level phase coding operations. An increase in the number of producible channels has also been obtained by expanding the number of bits of code sequence. These experiments are then supported by theoretical modelling, which clearly verifies successful operation of the device, but exposes potential improvements.

Chapter 4 will describe a package for continuous wideband tuning of a fibre Bragg grating. This device adopts the beam bending technique to produce compressive stress in the grating, which could then alter its properties. Very good agreement between the accompanying theoretical analysis and the experimental measurements demonstrates the ability of the device to accurately tune the operational wavelength. All the unwanted effects that could arise directly from the bending action are also studied to evaluate its stability and to learn the limitations of the device. In addition, the device is deployed in several optical systems to verify its reliability. The systems demonstrated are the distributed feedback fibre laser, add-drop multiplexer and high power fibre laser.

Finally, in Chapter 5, we will present a variable dispersion compensator based on mechanical parts. The proposed assembly allows displacement of the ends' level of a fixed beam, giving symmetrical stress distribution along the beam. The resulting contra-flexure at the mid-span will set the central wavelength to remain constant for all dispersion magnitudes. Characterisation of the device through calculations and measurements are shown. We demonstrate the dispersion compensation of high bit rate signals having propagated through long lengths of single-mode fibres. Additionally, it is shown that the device can also function as a bandwidth-variable filter for a spectrum-sliced WDM system.

1.3 Fundamentals of Fibre Bragg Gratings

1.3.1 Photosensitivity in Optical Fibres

Photosensitivity in optical fibre invariably refers to a permanent change in the index of refraction of the fibre core induced by exposure to light radiation. Its discovery has resulted in a revolutionary proliferation of the fibre Bragg grating structure. Extensive studies of this effect on an optical fibre host have subsequently allowed absolute control of the characteristic of the refractive index grating.

The fibre drawing process will always end up with an imperfect molecular structure of the glass waveguide due to non-uniform chemical reactions and difference in the thermal expansion coefficients between the cladding and the doped core regions. The presence of these defects causes multiple absorption bands within the UV spectrum. Based on several independent measurements of the electron spin resonances (ESR) and optical intensity absorptions of optical fibres and preforms, there is now a clear consensus on the absorption peaks assignment for a variety of defect species [43, 44].

Essentially, Ge(n) defect centres are recognised to be the major contributor to the photo-induced index changes in these fibres. These defects are the germanium (Ge) sites that can trap electrons. They can be in the form of germanium oxygen-deficient centres (GODCs) in which a germanium atom (or silicon atom) is directly bonded to another germanium atom due to the absence of an oxygen atom (wrong bond), which are also formerly identified as Ge(0) and Ge(3). Absorption bands at 242 nm (5.1 eV) and 330 nm (3.51 eV) have been correlated to this type of defect centre. Other defect centres observed are the Ge(1) and Ge(2) electron trap centres, which take the form of normal four coordinated Ge atoms, with distortion of the tetrahedral structure. The 281 nm (4.4 eV) and 213 nm (5.8 eV) bands have been assigned to these centres, respectively. In addition, large atomic displacement as the fibre glass cools on drawing also results in drawing-induced defects (DID). This defect is responsible for the 630 nm absorption band. Other defects include the nonbridging oxygen

hole centre (NBOHC) and the peroxy radical (P-OHC). They are responsible for the absorption bands at 260 nm and 160 nm, respectively.

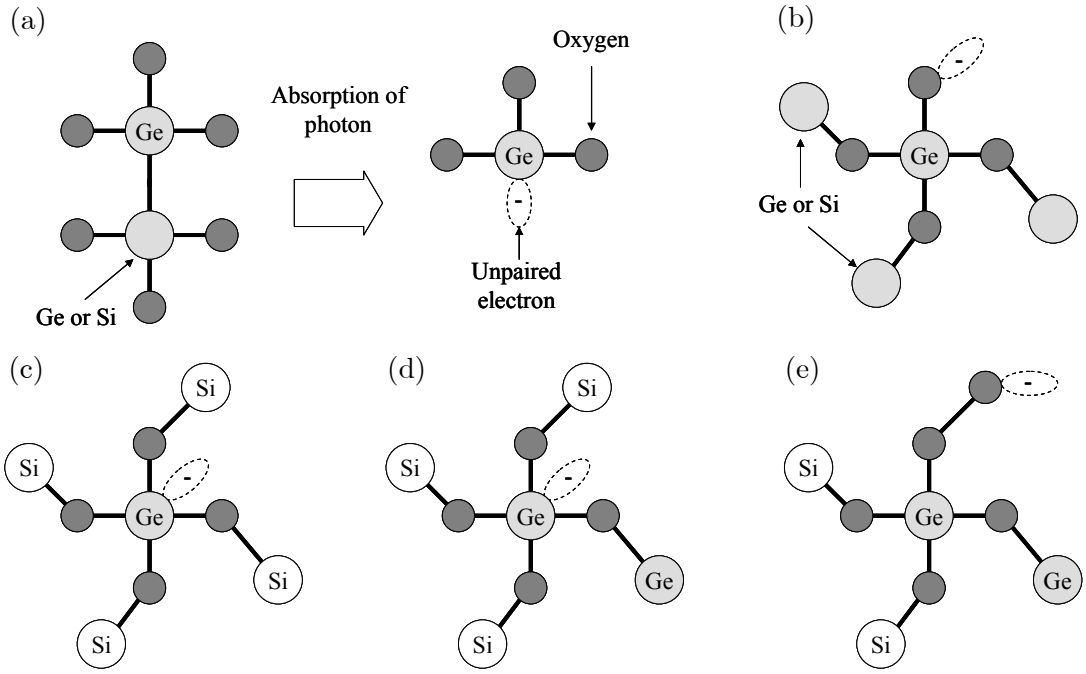

Fig. 1.1. A schematic of Ge (or Si) defects of germanosilicate fibre (Ge: germanium atom; Si: silicon atom; small sphere: oxygen atom). (a) GODC wrong bond that produces a GeE' centre through photon absorption, (b) NBOHC, (c) Ge(1), (d) Ge(2), and (e) P-OHC.

Various mechanisms, comprising photo-chemical, photo-mechanical and thermo-chemical may give rise to the change of refractive index of a silica fibre. It is documented that their relative contribution will be fibre dependent and also influenced by the irradiation condition such as wavelength, intensity and total dosage of irradiating light [43]. The bleaching of the Ge-Si/Ge-Ge wrong bonds, induced by exposure to UV radiation, forms the GeE' hole trap centres (i.e. $\mathrm{Ge}(0)^-$ or $\mathrm{Ge}(3)^-$), which constitute the largest absorption peak at 195 nm (6.35 eV). Each GODC releases an electron that assists the formation of new defect centres, $\mathrm{Ge}(1)^-$ or $\mathrm{Ge}(2)^-$, as electrons are retrapped at some other defect sites.

It is certain that this photochemical conversion of GODCs into GeE' centres contributes to a large portion of the photo-induced refractive index changes in germanosilicate glass [43], as a direct consequence of the associated transformation of the local electronic properties and also reconfiguration of the structure of the germania molecules that alters the density of the material [45]. Moreover, the interaction of the absorbed photons with the glass will also give rise to alterations in the absorption spectrum. Consequently, this will change the index of refraction at modal wavelength λ, as described by the Kramers-Kronig relationship [44],

$$\Delta n(\lambda) = \frac{1}{(2\pi)^2} \sum_i \int_{\lambda'_1}^{\lambda'_2} \frac{\Delta\alpha_i(\lambda')}{1-(\lambda'/\lambda)}\, d\lambda' \tag{1.1}$$

where the summation is over discrete wavelength intervals ($\lambda'_1 \le \lambda' \le \lambda'_2$) around each of the i changes in measured absorption, α_i.

A pure silica fibre requires certain core dopants for appreciable photosensitivity. Investigations on dopants such as germanium, phosphorus, nitrogen, aluminium and fluorine have revealed that germano-silicate optical fibre demonstrates the most pronounced photosensitivity [43]. Photosensitivity in this fibre increases with increasing concentration of the germanium. As large germanium content will also increase the numerical aperture (NA) of the waveguide, boron (B) may be included in order to neutralise the effect, thus preserving the original relative index difference between the core and cladding. Alternatively, tin (Sn) can substitute for some of the germanium to lower the NA but maintain the photosensitivity. These two co-dopants also facilitate the photo-induced densification process of the glass, thus further increasing the photosensitivity. Recently, it is found that high photosensitivity can also be obtained in germanium-free alumino-silicate optical fibre by co-doping with antimony (Sb) [46].

Photosensitivity of the fibre core can also be significantly enhanced through hydrogenation of the fibre before grating inscription [47]. Hydrogen molecules will react with the host material in a slightly pressurised atmosphere (150-200 atm.) producing more GODC centres under modest thermal stimulation (20-100 °C). It

is believe that a by-product defect species, GeH centre, also contributes to the photosensitivity enhancement. This technique has even successfully caused phosphosilicate fibre to demonstrate some photosensitivity, a composition which would otherwise have bleached wrong bonds. Nonetheless, this technique produces excessive absorption losses in the optical communication window at 1240 nm, 1390 nm and 1410 nm due to molecular hydrogen, Si-OH and Ge-OH respectively. These loss peaks can be shifted to longer wavelengths (∼1900 nm) by using a deuterium (D_2) substitute [48]. Another similar technique that forces hydrogen diffusion into the fibre core at high temperature is known as flame brushing [49]. High temperature is provided by a flame fuelled with hydrogen and a small amount of oxygen.

1.3.2 Properties of Fibre Bragg Gratings

A fibre Bragg grating (FBG) is a periodic perturbation of the refractive index along the fibre length, which is formed by exposure of the core to an intense optical interference pattern. The Bragg condition which governs its operation, is simply the requirement that satisfies both energy and momentum conservation [43]. If this condition is satisfied, the reflected light from each of the subsequent planes accumulates constructively in the backward direction.

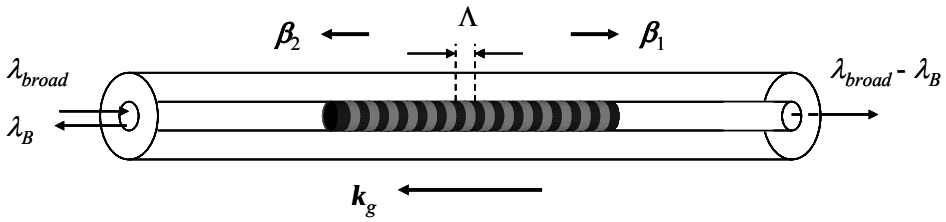

Fig. 1.2. Illustration of a uniform Bragg grating with the incident, diffracted and grating wavevectors.

Energy conservation requires that the frequency of the incident radiation and the reflected radiation is the same. Momentum conservation requires that the

incident wavevector $\boldsymbol{\beta}_1$ plus the grating wavevector $\boldsymbol{k}_g$, equal the wavevector of the scattered radiation $\boldsymbol{\beta}_2$. This is simply stated as

$$\boldsymbol{\beta}_1 + \boldsymbol{k}_g = \boldsymbol{\beta}_2 \tag{1.2}$$

where $\boldsymbol{k}_g$ has a direction normal to the grating planes with a magnitude $\left|\boldsymbol{k}_g\right| = 2\pi / \Lambda$ (where Λ is the grating spacing). The magnitude of the mode propagation vector (where $\beta = \left|\boldsymbol{\beta}\right|$) of a light ray with wavelength λ (in a vacuum) is given by

$$\beta = \left(\frac{2\pi}{\lambda}\right) \cdot n_{eff} \tag{1.3}$$

where n_{eff} is the effective refractive index of the guided mode. In the case of a Bragg grating (also referred to as a *reflection* or *short-period* grating), the diffracted wavevector is equal in magnitude, but opposite in direction to the incident wavevector. Hence, the above momentum conservation condition becomes

$$\lambda_B = 2n_{eff}\Lambda \tag{1.4}$$

where the Bragg grating wavelength λ_B is the free space centre wavelength of the input light that will be back-reflected from the Bragg grating. Conversely, a *long-period* grating (also called a *transmission* grating) will diffract a core mode into a co-propagating cladding mode with a different propagation constant.

The longitudinal profile of the index of refraction along a fibre grating with an amplitude of photo-induced refractive index perturbation Δn, can be expressed as

$$n(z) = n_0 + \Delta n \cdot \cos\left(\frac{2\pi}{\Lambda} \cdot z\right) \tag{1.5}$$

where z is the distance along the fibre axis and n_0 is the average refractive index, incorporating the mean refractive index change $\overline{\Delta n}$.

Coupled-mode theory has been used to accurately model the optical properties of most gratings [44, 50]. In the presence of a dielectric perturbation

associated with the fibre Bragg grating, a mode of amplitude $A_+(z)$ is coupled into an identical counter-propagating mode of amplitude $B_+(z)$ according to

$$\frac{dA(z)}{dz} = i\zeta A(z) + i\kappa B(z) \tag{1.6}$$

$$\frac{dB(z)}{dz} = -i\zeta B(z) - i\kappa^* A(z) \tag{1.7}$$

where $A(z) = A_+(z)\cdot\exp(i\delta z)$, $B(z) = B_+(z)\cdot\exp(-i\delta z)$, $\zeta = \delta - (2\pi/\lambda_B)\overline{\Delta n}$ is a general DC self-coupling coefficient, and $\delta = \beta - \pi/\Lambda$ is the detuning wavevector. The coupling coefficient κ, for sinusoidal variation of index perturbation along the fibre axis is given by

$$\kappa = \frac{\pi}{\lambda_B}(\eta\cdot\Delta n) \tag{1.8}$$

where η is the fraction of the fibre mode power contained in the fibre grating.

A solution of the coupled-mode differential equations 1.6 and 1.7 for a uniform fibre grating of length L, can be found by assuming that $A(-L/2) = 1$ and $B(L/2) = 0$. The amplitude reflection coefficient ρ, of a grating is given by $\rho = B(-L/2)/A(-L/2)$. This results in the following expression [51]:

$$\rho = \frac{-\kappa\cdot\sinh\sqrt{(\kappa L)^2 - (\zeta L)^2}}{\zeta\cdot\sinh\sqrt{(\kappa L)^2 - (\zeta L)^2} + i\sqrt{\kappa^2+\zeta^2}\cdot\cosh\sqrt{(\kappa L)^2 - (\zeta L)^2}} \tag{1.9}$$

The square of the *magnitude* of the complex amplitude reflection coefficient gives the power reflection coefficient R. On the other hand, the group delay and dispersion of the reflected light can be extracted from the associated *phase* θ. The time delay of the light reflected from a grating can be obtained by differentiating this variable with respect to the angular frequency ω of the reflection mode, which results in

$$\tau_g = \frac{d\theta}{d\omega} = \frac{d\lambda}{d\omega}\cdot\frac{d\theta}{d\lambda} = -\frac{\lambda^2}{2\pi c}\cdot\frac{d\theta}{d\lambda} \tag{1.10}$$

The dispersion D_g which is the rate of change of delay with wavelength, is thus given by differentiating the previous equation against the wavelength, producing

$$D_g = \frac{d\tau_g}{d\lambda} = \frac{d\omega}{d\lambda} \cdot \frac{d\tau_g}{d\omega} = -\frac{2\pi c}{\lambda^2} \cdot \beta'' \tag{1.11}$$

where β'' is defined as the group velocity dispersion (GVD) parameter (second derivative of the propagation constant with respect to frequency).

The grating period can be monotonically varied to produce a *chirped* Bragg grating. As a result, a wider band of wavelengths will be reflected along the structure. The grating may also be *apodised*, to suppress the adjacent sidelobes accompanying the main peak in the reflection spectrum. The term "apodisation" refers to a gradual decrease of the coupling coefficient from the centre towards both ends of the grating.

Fibre Bragg gratings may be divided into three distinct types, depending on their growth dynamics upon UV irradiation [43, 44]. Gratings that show monotonic temporal evolution of the index of modulation are referred to as Type I Bragg gratings. Often, subsequent UV light irradiation onto high Ge-content, small core fibres, will gradually erase this positive refractive index change and introduce a new Bragg grating species called Type IIA. Structural reorganisation is deemed to be responsible for these gratings exhibiting highly negative refractive index change with increased mean index change as exposure time continues. When physical damage has occurred due to irradiation at massive energy densities, Type II Bragg gratings are formed. Very large refractive index changes have been demonstrated by these types of fibre Bragg gratings. Furthermore, in comparison, by measurement of thermally induced decay, Type II Bragg gratings show the best temperature stability, followed by Type IIA and finally Type I Bragg gratings [43].

1.4 Simulation Methods of Fibre Bragg Gratings

1.4.1 Transfer Matrix Method

This piece-wise uniform approach is considered flexible and accurate for modelling non-uniform gratings. It is based on multiplication of 2 by 2 matrices for each uniform section of the grating to obtain a single 2 by 2 matrix that describes the whole grating. The propagation through a uniform section k, is described by a matrix T_k, defined such that [51]

$$T_k = \begin{bmatrix} \cosh(\Omega \cdot \Delta L) - i\frac{\zeta}{\Omega}\sinh(\Omega \cdot \Delta L) & -i\frac{\kappa}{\Omega}\sinh(\Omega \cdot \Delta L) \\ i\frac{\kappa}{\Omega}\sinh(\Omega \cdot \Delta L) & \cosh(\Omega \cdot \Delta L) + i\frac{\zeta}{\Omega}\sinh(\Omega \cdot \Delta L) \end{bmatrix} \tag{1.12}$$

where $\Omega = \sqrt{\kappa^2 - \zeta^2}$, ΔL is the section length, κ and ζ are the local coupling coefficients for the k-th uniform section.

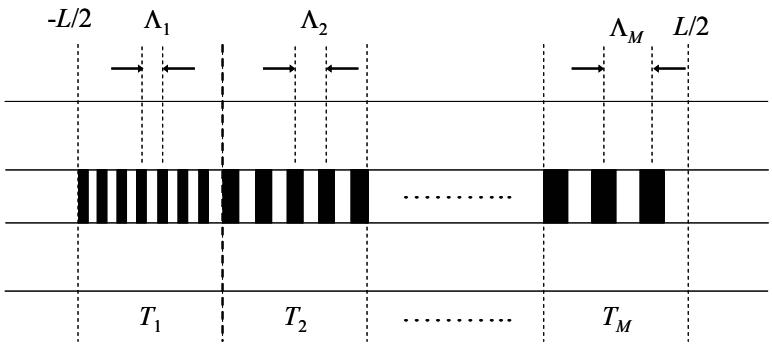

Fig. 1.3. Piece-wise uniform simulation which divides a non-uniform grating of length L into a series of M uniform gratings with different periods Λ_k and coupling coefficients κ_k, represented by their respective transfer matrix T_k.

A forward and backward propagating fields can be written as $A(z)\cdot\exp(i\delta z)$ and $B(z)\cdot\exp(-i\delta z)$, respectively, where δ is as defined in Section 1.3.2. $A(z)$ and $B(z)$ are slowly varying amplitudes of the mode travelling in the $+z$ and $-z$ directions, respectively. The output field amplitudes after traversing M sections is given by,

$$\begin{bmatrix} A(-L/2) \\ B(-L/2) \end{bmatrix} = \prod_{k=1}^{M} T_k \times \begin{bmatrix} A(L/2) \\ B(L/2) \end{bmatrix} \tag{1.13}$$

At the end of a reflection grating, the input field amplitude $A(L/2)$, is normalized to unity, and the reflected field amplitude $B(L/2)$, is zero since there is no perturbation beyond this margin. The amplitude reflection coefficients ρ, of the whole gratings is thus obtained by normalizing the total reflected field over the initial input field, both being evaluated at the leading edge of the grating frame, such that

$$\rho = \frac{B(-L/2)}{A(-L/2)} \tag{1.14}$$

and the reflectivity is calculated from the square of its magnitude $|\rho|^2$. Additionally, the amplitude transmission coefficient t, is simply expressed as follows

$$t = \frac{1}{A(-L/2)} \tag{1.15}$$

1.4.2 Layer-Peeling Inverse Scattering Method

Further approximation of the previous transfer matrix of the piecewise uniform simulation will result in discrete perception of the grating construction. By allowing the magnitude of the coupling coefficient κ, to be infinity while retaining the product with the segment length constant, the mode coupling occurs at a single point. This will lead to a simplified matrix describing a discrete reflector, such that

$$T_k^{\rho} = \frac{1}{\sqrt{1-|\rho_k|^2}} \cdot \begin{bmatrix} 1 & -\rho^* \\ -\rho & 1 \end{bmatrix} \tag{1.16}$$

The propagation matrix between two of such coupling points can be obtained by letting this same parameter assumes a value very close to zero. The original matrix will then become

$$T_k^{\Delta} = \begin{bmatrix} \exp(i\delta\Delta L) & 0 \\ 0 & \exp(-i\delta\Delta L) \end{bmatrix} \tag{1.17}$$

where the discrete complex reflection coefficient is given by

$$\rho = -\frac{q^*}{|q|} \cdot \tanh(|q|\Delta L) \tag{1.18}$$

The forward and backward propagating fields $A_k(\delta)$ and $B_k(\delta)$ respectively, at the k-th reflector can be transferred to the next section by multiplying them with the two transfer matrices product $T_k^{\rho} \cdot T_k^{\Delta}$. Normalizing both fields to the forward propagating field produces

$$R_{k+1}(\delta) = \exp(-2\delta\Delta L) \cdot \frac{R_k(\delta) - \rho_k}{1 - \rho_k^* R_k(\delta)} \tag{1.19}$$

where $R_k(\delta) = B_k(\delta) / A_k(\delta)$. The spectrum reflectivity $R_k(f)$, can be written as a Fourier transform of the time response $\rho(t)$, evaluated at the periodic discrete reflectors [52]

$$R_k(f) = \int_{-\infty}^{\infty} \exp(-j2\pi ft) \sum_{n=-\infty}^{\infty} \rho_k(t)\,\partial(t - n\tau)\, dt \tag{1.20}$$

where τ is the sampling period and $\partial(t)$ is the delta function, defined as $\partial(t) = 0$ $(t \neq 0)$ and $\int_{-\infty}^{\infty} \partial(t)\,dt = 1$. The above equation can be converted into a function with the wavenumber detuning δ, by substituting the frequency term with $c\delta / 2\pi n_{eff}$. The inverse of the Fourier transform of this expression will then give the ρ_k at those discrete points [53],

$$\rho_k = \frac{1}{M}\sum_{m=1}^{M} R_k(m)\exp\left(j\delta(c/n_{eff})(k\tau)\right) \tag{1.21}$$

where $R(m)$ is the sampled power reflection coefficient in the frequency domain.

By considering the impulse response for $t = 0$ (i.e. $k\tau = 0$), the first reflector will effectively be the sole reflector for the entire stack, as light does not have sufficient time to propagate to and from the adjacent reflectors. Therefore, the amplitude reflection coefficient for the first reflector is given by

$$\rho_0 = \frac{1}{M}\sum_{m=1}^{M} R_0(m) \tag{1.22}$$

This value can be inserted in Equation (1.19) to complete the transfer of both the forward and backward propagating fields $A_k(\delta)$ and $B_k(\delta)$, respectively. Consequently, the layer can be totally ignored (i.e. peeled off) when evaluating the next reflector.

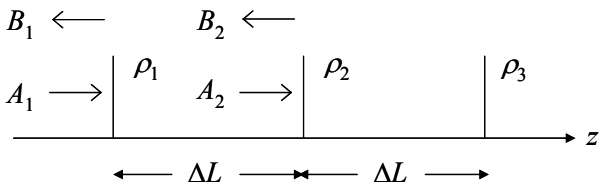

Fig. 1.4. Discrete model of a fibre grating.

Finally, taking the unit time frame to be equal to the "round trip" propagation length of one layer ($\tau = 2n_{eff}\Delta L/c$), the layer thickness ΔL, and detuning window δ_w, must be related by

$$\Delta L = \frac{\pi}{\delta_w} \tag{1.23}$$

1.5 Bragg Grating Inscription

An interference fringe of UV light is required to induce a periodic perturbation in the refractive index of a fibre via the photosensitive effect. Conventionally, the interference fringe is produced by the holographic method, in which UV light is passed through a beam splitter and reflected by mirrors to intersect at a mutual angle of θ. Minute adjustment to the angle of the mirror can alter the grating characteristic through the following relationship [54],

$$\Lambda_g = \frac{\lambda_{UV}}{2n_{UV}\sin\left(\theta/2\right)} \tag{1.24}$$

where Λ_g is the period of the grating, n_{eff} is the effective mode index in the fibre, n_{UV} is the refractive index of silica and λ_{UV} is the wavelength of the writing radiation.

On the other hand, the phase mask technique is regarded as the most effective method to inscribe Bragg gratings [55, 56]. Incident light is divided into two beams of different order after passing through the phase mask and these then overlap to create the desired interference pattern. "Phase mask" refers to a piece of transparent bulk material with grooves etched into it at a regular spacing, which may be formed by electron beam lithography. This structure is thus able to alternately shift the phase of light wavefronts, such that the lightwave leaving the grooves will have different phase relative to those that travel through the full depth. Moreover, as the lightwave passes through narrow spaces with sharp edges, it will naturally diffract. The incident and diffracted orders satisfy the principle of interference, which dictates that the geometrical path difference between light from adjacent grooves must be equal to some integral multiple of the wavelength of the light for a constructive interference [57], such that

$$\Lambda_{pm}\left(\sin\left(\theta_i\right)+\sin\left(\theta_r\right)\right) = r\lambda_{UV} \tag{1.25}$$

where r is an integer signifying the diffraction order, Λ_{pm} is the period of the phase mask, θ_i is the incidence angle and θ_r is the diffraction angle.

The phase mask can be employed in two configurations. In one configuration, light incident at an angle is diffracted partially only into the minus first order, provided that $2\Lambda_g / 3 \leq \lambda_{UV} \leq 2\Lambda_g$. This condition is deduced by appreciating the wave behaviour of light, such that diffraction must occur ($\left|\sin(\theta_{-1})\right| \leq 1$) when the diffracted angle equals the incidence angle ($\theta_i = \theta_{-1}$) and the second order must not exist [58]. Self-interference between the minus first order and the undiffracted zero order creates an interference pattern with a pitch equal to the phase mask pitch (derived by solving Equations (1.24) and Equations (1.25)). When a phase mask is operated in the other configuration, the UV light is normally incident on the grating ($\theta_i = 0$). The phase mask is optimized to diffract light equally and maximally into the plus first and minus first orders, while the intensity carried in the zeroth order is suppressed. Self-interference between these two orders creates an interference pattern with half the pitch of the phase mask pitch. This geometry however can still generate additional unwanted orders, but these are often minimized. The phase mask greatly reduces the complexity of the fibre grating fabrication system. The simplicity of using only one optical element provides a robust and an inherently stable method for reproducing fibre Bragg grating. Since the fibre is usually placed directly behind the phase mask in the near field of the diffracting UV beams, sensitivity to mechanical vibrations and, therefore, stability problems are minimized.

Efficient grating inscription can only be realised when the wavelength of the writing radiation coincides with any peak of absorption spectrum in the UV region of the photosensitive host fibre. There are already several lasers that can efficiently operate in this wavelength region, which include excimer lasers, frequency mixed fibre/diode lasers and frequency doubled dye lasers or optical parametric oscillators. In order to produce high quality gratings, the laser sources should have excellent temporal and spatial coherence. Low spatial coherence causes a variation in fringe visibility and hence the grating strength. Light with low temporal coherence can produce interference fringes with reduced visibility if the paths of the two interfering beams are not equal. This requirement is however relaxed in the phase mask technique. Sources with poor features can be improved by frequency mixing using nonlinear crystals (e.g. beta barium borate) and spectral filtering using etalons, intracavity prisms or diffractive gratings. Some

examples of good sources are KrF (248 nm), XeCl (308 nm), ArF (193 nm), 1064 nm Nd:YAG (frequency quadrupled to 266 nm), 1048nm Q-switched Nd:YLF (frequency quadrupled to 262 nm) and 302 nm or 514/488 nm Argon ion (frequency doubled to 257/244 nm). There are also frequency doubled dye lasers which use either excimer (XeF or XeCl) or frequency tripled Nd:YAG lasers as pump sources.

An advanced fabrication system that is truly flexible has been developed at the *University of Southampton*. It is referred to as the *continuous grating writing technique* as the planes of the grating are written continuously by high precision relative positioning of the phase mask and the fibre host with synchronised exposure of UV radiation [59]. The fabrication setup for performing this technique is illustrated in Fig. 1.5.

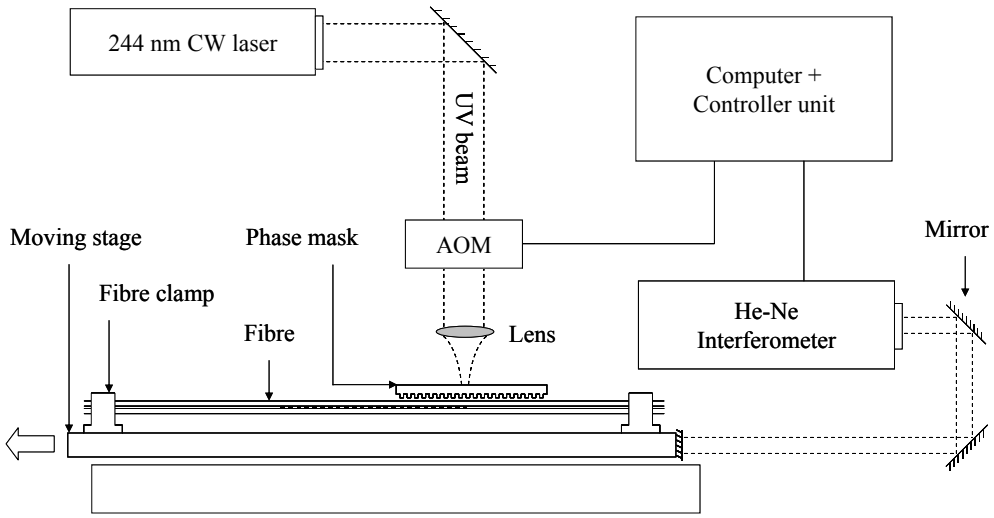

Fig. 1.5. Fabrication setup for continuous grating writing technique (AOM: Acousto-optic modulator).

The writing UV radiation is provided by a frequency doubled Argon ion laser system operating with continuous wave (CW) light at 244 nm. It can deliver a UV beam with a power of up to 100 mW. An intermediate acousto-optic modulator (AOM) is deployed across the beam path to regulate the exposure

duration of the UV light on the fibre. A cylindrical lens is used to focus the beam, as well as producing constant fluence and exceptional spatial coherence. The height of the lens is routinely adjusted to yield maximum fluence by monitoring the trapped interfering beams which are weakly guided in the fibre. The photosensitive fibre host is held in a straight line by a pair of fibre clamps fixed on an air-cushion supported movable carriage. Deuterium loaded germanosilicate fibres are often used as the host due to the fact that they are adequately photosensitive to obtain the required refractive index change and also environmentally stable. This type of fibre is typically a standard telecom compatible fibre with numerical aperture (NA) of approximately 0.12. The translation platform is moved at a constant velocity parallel to the fibre axis under computer control, with its position being tracked by an interferometer attached to the moving part (with sub-nanometre precision). A uniform pitch phase mask is fixed exactly at the focal point of the cylindrical lens. This arrangement ensures that the UV light falls normally onto the surface of the phase mask. Subsequently, it generates interference fringes from $+1$ and -1 orders of the diffracted UV light. Despite the uniform pitch, the fabrication apparatus still offers the capability to write a grating with complex refractive index and/or period modulation, owing to the plane-by-plane writing procedure.

An apodisation technique based on dithering of the grating fringes is used for modulating the refractive index. The visibility (or contrast) of the refractive index modulation can be modified by delaying the exposure of the interference fringes for less than, or equal to, one half of the interference fringes period Λ. This process is able to retain zero mean change of refractive index ($\overline{\Delta n} = 0$) and thus avoids variation in the average refractive index n_0. On the other hand, chirping of the grating period from $\Lambda - \Delta\Lambda/2$ to $\Lambda + \Delta\Lambda/2$ can be achieved by delaying the subsequent exposures by a fraction of a grating fringe $\delta\Lambda = \Delta\Lambda / N$, where N is the total number of grating planes in the entire grating [59].

In essence, this fabrication process imprints overlapping gratings. Consequently, it inherits the advantage of averaging any jitter and variations in the transverse beam profile between exposures. Additionally, the length of the grating is only limited by the length of the translation platform bearing the fibre

and not by the length of the phase mask. Nevertheless, the quality of the fabricated gratings may still be dependent on the stability of laser fluence, the quality of the phase mask and the fibre host and occurrence of mechanical vibrations in the writing setup. These may cause stitching error (unwanted sudden phase change between adjacent grating planes) and variations in fringe visibility that will lead to random artificial chirps along the grating. As a consequence, the grating reflection spectrum acquires multiple peaks and chirp, while considerable fluctuations are introduced in the time delay response [59, 60].

1.6 Characterisation of Fibre Bragg Gratings

The measurement of the complex amplitude reflection/transmission coefficient of a grating is realizable if a signal detected from the device can produce an electrical signal at the photo-detector that carries its optical phase and amplitude information. This can be practically achieved by means of passing a continuous light modulated at an RF frequency (a few hundred of megahertz) through the device. The power reflection/transmission coefficient is thus directly proportional to the amplitude of the received signal, while the time delay can be extracted from the measured relative phase.

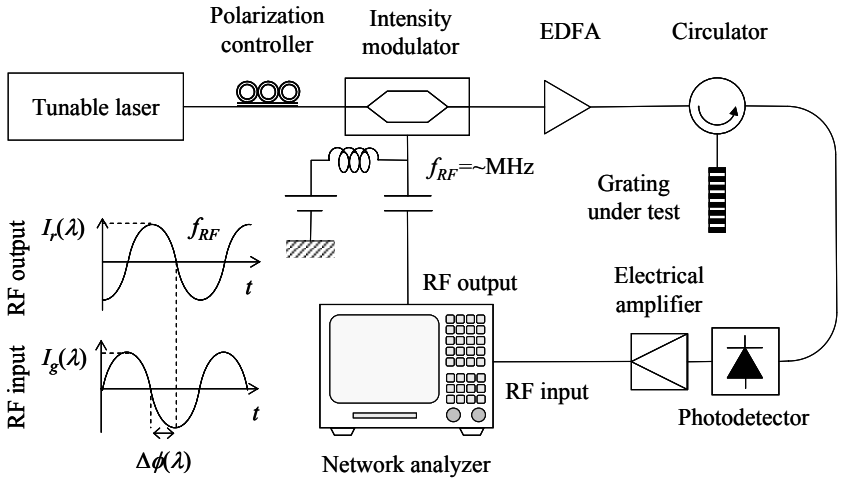

Fig. 1.6. Experimental setup for measuring characteristics of fibre gratings.

A simple, yet reliable experimental setup for measuring the characteristics of a fibre grating is illustrated in Fig. 1.6. An RF sinusoidal signal of frequency f_{RF}, from a network analyzer drives an $LiNbO_3$ modulator which modulates the light intensity from a tunable single-frequency source. The modulated light is optically amplified using an erbium-doped fibre amplifier (EDFA), to compensate for the considerable insertion loss introduced by the modulator, and subsequently launched into a grating under test. The transmitted light or reflected light collected via a circulator/3-dB coupler is captured by a photodiode. The detected signal is introduced into the RF input port of the network analyzer, after amplification. Using the network analyzer, the intensity ratio $\Delta I(\lambda)$, and phase difference $\Delta\phi(\lambda)$, between the modulation and the input signals are measured at each carrier wavelength. The relative delay time $\tau(\lambda)$, of the fibre grating is obtained from $\Delta\phi(\lambda)$ as

$$\tau(\lambda) = \frac{1}{f_{RF}} \cdot \frac{\Delta\phi(\lambda)}{2\pi} \tag{1.26}$$

This data is acquired quickly, with minimum processing, under computer control. The use of this technique relies on the temperature being constant over the wavelength region of interest. Nevertheless, errors initiated by temperature variations can be reduced by minimizing the optical path from the modulator to the fibre grating. Another possible source of error is polarization variation of the input field to the modulator. Several other techniques have included attempts to keep these errors to minimum. In one demonstration [61], a measurement setup based on the vector-voltmeter optically generates a frequency reference after the modulator. This ensures that any amplitude and phase changes are common to both the reference and the signal. In another demonstration based on an all-fibre Michelson interferometric technique, the system incorporates a control signal at a fixed wavelength far outside the measurement range [62]. It provides feedback for adjusting the optical path of one interferometer arm with a fibre grating to precisely equalize any path change in the other arm.

1.7 Review on Applications in Optical Networks

The fibre Bragg grating is capable of executing many functions in optical communication networks as it features an ideal filtering property and tailorable spectral or phase response. It may function to improve the performance of system components, as well as a unit performing essential networking tasks. There are already numerous successful demonstrations illustrating these functions, which include the frequency stabilisation of semiconductor lasers, fibre lasers, fibre amplifier optimisation, gain equalization, add/drop multiplexers, dispersion compensation, phase conjugators, wavelength converters and fibre sensors; some of these will be briefly described in this section.

A fibre Bragg grating is used as a feedback mirror to form an external cavity for stabilizing a Fabry-Perot diode laser [63]. A weak grating with 1-10% reflectivity is adequate to achieve robust stabilization and maximize the laser output. This grating, with a narrow bandwidth, reflects a wavelength within the gain bandwidth of the semiconductor material, setting the lowest loss lasing mode at the Bragg wavelength. Furthermore, it suppresses undesired resonances and narrows the spectrum of the lasing mode. This assembly reduces the sensitivity of the diode laser to the temperature variation through the massive increase in the total optical cavity length.

Fibre Bragg gratings are also used to conveniently define wavelength and limit lasing to a single frequency in rare-earth doped fibre lasers. In a distributed Bragg reflector (DBR) laser configuration, a few metres of erbium-doped fibre provides the gain medium, while the intracore Bragg reflectors establish the wavelength-selective resonator mirrors [64]. The doped fibre is optically pumped at either 650 nm, 980 nm or 1480 nm. Typically, one of the mirrors is a broadband 100% reflectivity grating, while the other is a narrowband grating with 80% reflectivity, which also becomes the output coupler. By incorporating a sampled grating in a ring configuration, the erbium-doped fibre is thus configured as a multiwavelength laser. In this configuration, the grating serves as a comb filter to promote lasing at the peak reflection wavelengths [65]. It is also possible

to realize a single-mode operation by introducing a $\pi/2$ phase shift in the middle of a single grating inscribed in a gain medium [66]. This structure describes the distributed feedback (DFB) fibre laser. In addition, a fibre laser can also be constructed using a length of highly nonlinear fibre with a set of highly reflecting grating pairs. Lasing is achieved via stimulated Raman scattering, which downshifts pump frequency yielding Stokes signals at longer wavelengths [67]. The laser output is extracted from a partially reflecting fibre grating (~20%) at the final Raman shift stage.

The performance of fibre amplifiers can be enhanced considerably by redirecting the residual pump light back into the gain region or passing the signal lights into the doped fibre for the second time for further amplification. These processes can easily be accomplished by utilizing highly reflecting fibre gratings operating at the pump and signal wavelengths [68]. Reflecting only the pump light may increase the amplifier saturated output power, while double passing only the input signal may increase the small-signal gain. Undesirable bandwidth narrowing may occur in optical links with a series of optical amplifiers due to their uneven gain spectrum. In order to maximize the useful gain bandwidth, fibre grating filters, with a loss spectrum matching the erbium gain spectrum at a nominal operating condition [18-21], can be placed between these fibre amplifiers.

A low insertion loss and high channel isolation bandpass filter is formed by simply placing a fibre Bragg grating in the second port of a three-port circulator. It is transformed into an optical add/drop multiplexer by connecting another circulator on the transmission end of the grating [69]. Cascading two 3-dB couplers will build up a Mach-Zehnder interferometric arrangement, and inscribing two identical gratings in both mutual arms enables this assembly to perform the same function [70]. Simultaneous separation of N channels can be achieved by placing a pair of gratings in each output port of a single $1:N$ fused fibre coupler. These gratings are designed to reflect all channels except the desired transmission wavelength [71].

Chirped or aperiodic gratings that reflect different wavelengths at different points along the structure have been proposed to compensate for dispersion penalties in operating the 1550 nm band on the installed base of non-dispersion

shifted 1300 nm single mode fibre [41]. The device produces dispersion of opposite sign and equal to that of the transmission fibre by coupling the signal into the longer wavelength end of the grating. Alternatively, a uniform grating placed in line with the transmission fibre can also cancel the anomalous chromatic dispersion. This is effective only when the channel wavelength falls inside the long wavelength edge of the grating stop band [72], so as to exploit the rapid change of the time delay response in this region. Reversing the signal optical spectrum approximately in the middle of the span can also undo the signal distortion associated with dispersion. This is achieved through a process called phase conjugation by utilizing the four-wave mixing effect. In one example of such a nonlinear optical circuit, a fibre Bragg grating has efficiently assisted the construction of a polarization independent optical phase conjugator by functioning as the pump reflector [73].

A fibre Bragg grating may be located at the remote node of a WDM passive optical network (PON) as an optical sensor for detecting temperature-induced drift of the operating wavelengths of the channel router. It will reflect a probe signal back to the central office for determination of the necessary adjustment to the source wavelengths [74]. A fibre Bragg grating has also been used as a filter at the output of a wavelength converter to reject spurious light at the input signal wavelength. This wavelength converter is based on gain saturation of an integrated multi-frequency laser [75]. The grating provides the required high rejection and narrow stopband to prevent crosstalk and signal loss.

From the examples of the applications of fibre Bragg gratings in the optical communication networks given in this section, it can be appreciated that this device is reliable to perform those tasks and potentially many more. It would be definitely advantageous for those devices to become reconfigurable or tunable so as to facilitate the advancement towards realizing true flexibility in channel management of future networks. It is for this reason that our research is manoeuvred parallel to this foreseen evolution.

Chapter 2

Gain Flattening Transmission Filter

2.1 Introduction

Wavelength division multiplexed (WDM) transmission systems are established by allocating communication channels to partitions in the optical frequency domain. These systems are able to increase capacity on installed fibre routes at a lower cost than installing new fibre cables. Additional functionalities are expected when WDM systems incorporate wavelength add/drop capability for optical networking. As a consequence to this evolution in optical communication systems, new critical issues arise and need to be dealt with. These issues include the deleterious effect of fibre dispersion, optical fibre nonlinear interactions between channels and signal-to-noise considerations.

Many optical components contribute crucial roles in enabling WDM. Among them, erbium doped fibre amplifiers (EDFAs) are known to be the key components for the construction of long haul WDM transmission systems [4]. The gain curve of a typical EDFA is however, nonlinear over the operational wavelengths between 1530 nm and 1580 nm. Some channels are preferentially amplified at the expense of another and this effect is accumulated along many amplifier spans. Consequently, the WDM system capacity will be degraded. This characteristic is disadvantageous to the performance of the EDFA and necessitates gain equalisation. On this account, this research is dedicated to designing gain flattening filters (GFFs) in order to address the detrimental effect of gain non-uniformity of EDFAs.

This Chapter will begin with a brief background of the EDFA and be followed with a review of the technologies currently used for gain flattening. Then, our approach for designing the transmission filter based on the fibre Bragg grating will be introduced. Gratings with modulated chirp rate and refractive index change will be synthesized. The device responses will be simulated using the transfer matrix method. Comparison with the layer-peeling inverse scattering method [52] will also be provided for reliability assessment. Finally, the properties of the designed devices will be discussed.

2.2 Erbium-doped Fibre Amplifier and Gain Flattening

2.2.1 Gain Characteristic of EDFA

The EDFA is an optical amplifier that faithfully amplifies lightwave signals purely in the optical domain. It may function as a power amplifier to boost transmitter power, as repeaters or in-line amplifiers to increase system reach, or as pre-amplifiers to enhance receiver sensitivity in optical fibre transmission systems. Furthermore, higher output powers and simultaneous amplification of many wavelengths are possible, thus allowing reduction in the number of system elements from a route design. This lowers system cost and improves system reliability. It also offers the possibility to compensate for transmission loss of signals independent of their modulation format or their channel data rate.

The amplification process is based on the principle of erbium ion stimulation of the erbium-doped fibre by the pump laser [5]. The pump laser provides constant optical energy at a fixed wavelength to excite electrons in erbium atoms to a higher energy state. A portion of this energy is then transferred to the weak incoming optical signal as the excited electrons return to their lower energy state. The direction and phase of the energy emitted from the excited erbium atoms corresponds to that of the incoming optical signal, so the weak optical signal is amplified along its direction of propagation.

The erbium atoms in the EDFA reside in a glass host, an amorphous material that preserves most of the dynamics of the erbium energy states (Fig. 2.1). The differences in local environments of erbium atoms within the glass matrix cause subtle variations in the energy levels of erbium atoms. The multiplicity of the energy levels is sometimes referred to as Stark splitting. This generates a wide spectral bandwidth in the EDFA and thereby renders it suitable for WDM applications. However, the transition probability for stimulated emission to occur in an EDFA depends on the frequency of the photon. This wavelength-dependent probability of amplification that is proportional to the gain factor, explains why the EDFA has a non-uniform gain across its bandwidth.

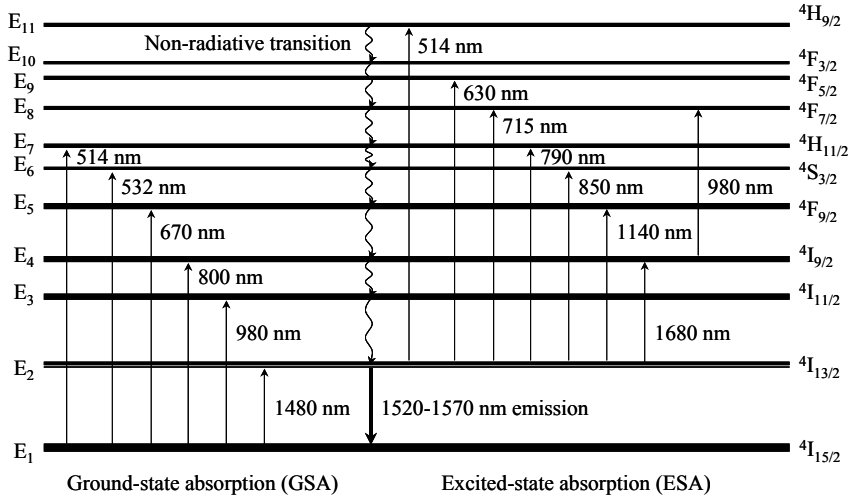

Fig. 2.1. Energy levels of an erbium ion in a silica matrix [5].

The gain shape of an EDFA is also affected by the wavelength response of the system components. Additionally, the amplifier gain uniformity is a function of its operating conditions. The principal parameters include pump power, input wavelengths and input power levels. At low input and high pump powers, the gain peaks between 1530 and 1535 nm and plateaus between 1540 and 1560 nm. The difference in gain between the peak and plateau can exceed 10 dB. However, at higher input powers, the EDFA gain is more uniform.

The gain shape of an EDFA has several peaks and valleys and will not amplify signals that are at different wavelengths with the same gain. In a chain of cascaded amplifiers, the signals near the peak of the gain will grow at the expense of the other signals. The effective gain of the entire amplifier chain narrows as a result of concatenation of gain spectra, which are individually narrowed. The accumulated wavelength gain differences along the amplifier chain may exceed the receiver dynamic range. Consequently, this will result in an imbalance in the signal-to-noise ratios of the channels. Moreover, amplifiers operating at high inversion levels tend to favour a strong ASE peak near 1530 nm, which robs the gain and reduces the signal-to-noise ratios at the longer wavelengths. Filtering of this peak then becomes necessary.

The gain non-uniformity not only can lower the signal strength, but also can raise the power of certain channels. At the event when the total output power and the output power per channel are above certain thresholds, optical nonlinearities may occur [5]. These phenomena can distort the transmission signals and overload the receivers. The substantial difference in signal amplitudes of the channels at the receiver may also result in crosstalk leaking through the demultiplexer from adjacent channels [29].

2.2.2 Gain Flattening Technologies

The erbium-doped fibre amplifier intrinsically exhibits a limited flat gain profile at wavelengths away from the peak gain. Thus, the amplifier can be operated at these wavelengths to have the benefit of equal distribution of powers of the various channels. The bandwidth of operation can be determined through astute choice of pumping conditions [4]. Wavelength range with flat responses of about 12 nm centred near 1550 nm or 30 nm centred near 1585 nm can be achieved. This is, however, restrictive in terms of the available bandwidth and overall channel capacity. Moreover, operating amplifiers at the latter bandwidth region requires longer fibre lengths to achieve reasonable gain due to the lower emission cross section in that region. In fact, this approach is also used for making an L-band amplifier [76].

Considering the complexity of demultiplexing and impairments by four-wave mixing, channels should not be spaced too closely in WDM systems. To maximize WDM capacity, it is desirable that the optical bandwidth of the system be as wide as possible. Amplifiers with flat gain over a substantial spectral range are thus desired. Requisite gain flatness for WDM transmission over long distances can be achieved by imposing pre-emphasis of input signals [6]. The launched powers are adjusted to make the signal-to-noise ratios equal at the output. The usefulness of this technique is limited however, especially as the number of cascaded EDFAs is increased and as channels are added and removed.

A wide flat bandwidth of operation has been implemented by the use of alternating series of high inversion and moderate inversion amplifiers [7]. Nevertheless, due to the fact that the gain flatness in this technique is determined solely by the inversion levels, it shows high sensitivity to system changes, since such changes will alter the operating conditions and thus the inversion levels. A number of similar approaches to this technique have also been demonstrated by using multiple amplification stages, which are either in a cascade or split arm configuration. One of these hybrid methods produces flat gain as a result of superposition of gain spectra arising from amplifiers of different glass hosts or compositions [8]. The same result can also be obtained by cascading a Raman amplifier, which has an inverse gain slope to that of the erbium-doped fibre amplifiers [9]. These last two techniques offer the advantages of having wide bandwidth of amplification and allowing independent optimisation of each amplifier for operation in a given wavelength band.

Change of silica host glass composition can also produce a flatter gain spectrum. High concentration of aluminium or phosphorus co-dopant is introduced in silica fibres to reduce the dip between the 1530 nm peak and the 1550 nm shoulder in the spectrum [10]. Alternatively, the fibre glass host has also been substituted to obtain flat gain operation. A fluoride-based amplifying medium produces significantly larger intrinsic flat bandwidth than silica, that is about 30 nm, from approximately 1530 nm to 1560 nm, where the gain variation is less than 1.5 dB (with an average gain of 26 dB) [11]. However, disadvantages occur due to high fabrication complexity, difficult handling and higher noise

figure due to its main pump wavelength of 1480 nm. Lower noise figure can be achieved with 980 nm pump wavelength at the expense of gain efficiency. In the same respect, tellurite host glass produces wider gain spectrum, but requires the use of an equalizing filter for a flat gain profile. The alteration of glass composition and the substitution of glass host comprise only a quite narrow set of wavelength, span losses and amplifier parameters, thus other solutions have been investigated.

In recent years, a variety of methods to flatten the gain have been implemented by using external passive, or active, filters. These external filters effectively induce transmission loss, matching the inverse gain profile of the EDFA. Thus, they can help to significantly increase the bandwidth of the transmission span. The earliest approach comprises an optical notch filter. The mechanical filter is incorporated within the length of an erbium-doped fibre amplifier. Its principle of operation is based on the resonant coupling between a core propagating mode and a leaky cladding mode [12]. Another approach with the same principle, utilizing D-shaped fibre with an overlay grating, has also been demonstrated [13]. Split-beam Fourier filters [14] and thin film filters can also be used to provide the necessary transmission loss.

A number of approaches that demonstrate loss tunability in gain equalizing filters have been reported. The first demonstration uses an acousto-optic filter [15]. The acousto-optic filter produces a wavelength dependent loss that can be tuned electrically. A Mach-Zehnder filter used for the gain flattening purpose, can also be tuned, in terms of the filter transmittance function, by means of a heater attached to one of the interferometric paths that makes up the Mach-Zehnder filter [16]. Tunable Fabry-Perot etalon filters have also been reported to be used effectively as gain equalizers in long distance transmission systems [17].

Advances in fibre grating technology has resulted in pervasion of this effective narrowband filtering element into the gain flattening application. Different positioning of fibre Bragg gratings within an amplifying medium has produced a pronounced flat gain over a wide bandwidth [18]. This is achieved as a result of the difference in the amount of amplification experienced by each of the reflected wavelength signals. Blazed gratings are also capable of flattening the

gain [19]. The blaze parameters can be designed to couple the fundamental mode of the single mode fibre into cladding modes with a given centre wavelength, bandwidth and loss. Another equally successful demonstration utilising a long-period grating has also been reported [20]. However, because the coupling of light out of the core is obtained through a weak resonance, these gratings are highly bend-sensitive and must be packaged carefully. More recently, a short period fibre Bragg grating with specially designed strength and phase characteristics has also been demonstrated for a similar application, which can also simultaneously perform dispersion compensation of the signals upon reflection [21].

Despite their effective implementations, one common disadvantageous feature of these passive filters is the trade-off between bandwidth and loss. More attenuation needs to be provided at the wavelengths of peak gain in order to obtain a wider bandwidth. This impacts either the noise figure or the output power and gain, depending on the placement of the filter and the pump power available for pumping the amplifier stages.

2.2.3 Fibre Bragg Grating for Gain Flattening

Generally, optical amplifiers are required directly after transmitters for generating adequate power to overcome the optical signal power loss caused by fibre attenuation. Its uneven gain profile however necessitates the addition of a gain-compensating device at the output. Any spectral device that is designed to flatten the output spectrum should impose minimal insertion loss. In this respect, a fibre Bragg grating with an appropriate loss response curve could be operated in transmission to perform the task, while eliminating the need for a circulator.

The transmission loss is found to be a function of the grating refractive index change, as well as being inversely proportional to the chirp rate [21]. This relationship is obtained by fitting the measured transmission loss with varying refractive index modulation, or varying chirp rate through a nonlinear function. It follows that these parameters are related to each other in compliance with the following equations,

$$\Delta T(z) = \left(\eta(z) \cdot \delta n(z)\right)^2 \times \frac{14.78}{\left|CR(z)\right|} \tag{2.1}$$

$$= \left(\eta(z) \cdot \delta n(z)\right)^2 \times \frac{\left|D(z)\right|}{6.5447 \times 10^{-10}} \tag{2.2}$$

where $\Delta T(z)$ is the transmission loss in decibels, $\eta(z)$ is the fraction of modal power in the grating, $\delta n(z)$ is the refractive index modulation, $CR(z)$ is the chirp rate in the grating ($CR(z) \neq 0$), and $D(z)$ is the dispersion at a given position in the grating. These formulas use the basic SI units for all quantities, such that $CR(z)$ and $D(z)$ are in m/m and s/m, respectively. The value of the chirp rate $CR(z)$ must at least produce a grating with a bandwidth larger than that of a uniform grating with the same length. Some or all of the parameters may vary accordingly along the grating to facilitate distributed transmission loss. In other words, the desired transmission loss at a particular operation wavelength is induced at a distinct position in the grating, which has unique values of those parameters. It is also noteworthy that the dispersion in the grating will be of no significant consequence to the transmitted wavelength signals, since it does not cause any path difference, in contrast to those that are reflected. Therefore, each of the transmitted wavelength signals will arrive at the output end of the grating after similar propagation time.

In this thesis, we propose a gain-flattening filter composed of only a single fibre Bragg grating with either a modulated refractive index change and a constant chirp rate, or a modulated chirp profile and a constant refractive index change. The grating with a modulated refractive index and a constant chirp rate is proposed to have its grating strength controlled by varying the "fringe contrast" instead of varying the UV intensity during fabrication, in order to acquire constant average effective refractive index, thus avoiding artificial period variation (chirp). On the other hand, in order to modulate the chirp rate of a grating with a uniform refractive index change, "period" modulation is selected to linearly vary the Bragg wavelength as a function of position along the fibre axis, instead of varying the local effective refractive index by UV treatment. This could maintain constant average effective refractive index and also reduce photo-induced loss.

Several aspects have to be carefully considered in the design. For example, the length of the grating, which may influence the packaging, the practical refractive index change and the size of the fabrication system. Also, a practical amount of refractive index change needs to be properly chosen since it may cause unwanted photo-induced loss in the fibre and high complexity of the fabrication process due to the requirement for higher photosensitivity. There is arguably the necessity for apodisation. Hence, a trade-off between gain flatness and the transmission ripple has to be appreciated. Last but not least, the number of subsections in simulation would also influence the accuracy of the design with the actual prototype.

2.3 Device Simulations

2.3.1 Modulation of Refractive Index Change with Constant Chirp Rate

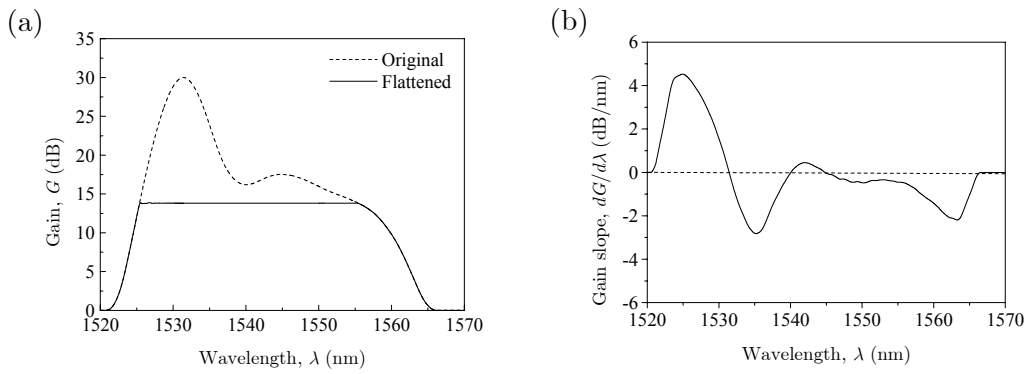

Fig. 2.2. (a) Overlay of the original gain profile of the EDFA and the desired flat gain window, and (b) the corresponding gain slope.

The grating models in the simulation are designed to flatten a 30 nm bandwidth of a highly inverted erbium-doped fibre amplifier in order to demonstrate the worst-case scenario. This condition corresponds to a gain

spectrum with a 15 dB gain variation and the maximum gain slope of 4.5 dB/nm, as illustrated in Fig. 2.2. The wavelength band to be flattened is selected so that the highest possible average gain can be obtained within this bandwidth. Consequently, the derived window of interest is found to be between 1525 nm and 1555 nm.

Initially, a refractive index change profile of a grating with uniform period is deduced from Equation (2.1), which should then provide a transmission loss matched to the inverse of the nonuniform gain profile shown in Fig. 2.2. Nevertheless, abrupt change at the edges of the resulting refractive index modulation triggers broadband reflection, which then interferes with the distributed reflection of the grating. This interference causes the gain amplitude to acquire a ripple as shown by the simulated result in Fig. 2.3(a).

Fortunately, the broadband reflection can be dramatically reduced by apodising the refractive index change profile. The resulting flattened gain profile produced by the apodised grating is shown in Fig. 2.3(b). Also shown is the apodised refractive index change in Fig. 2.4(a). A noticeable hump can be observed at each end of the flattened wavelength band. This arises from the alteration of the refractive index change within the apodisation regions, which is thus unable to provide sufficient transmission loss to their associated wavelength signals.

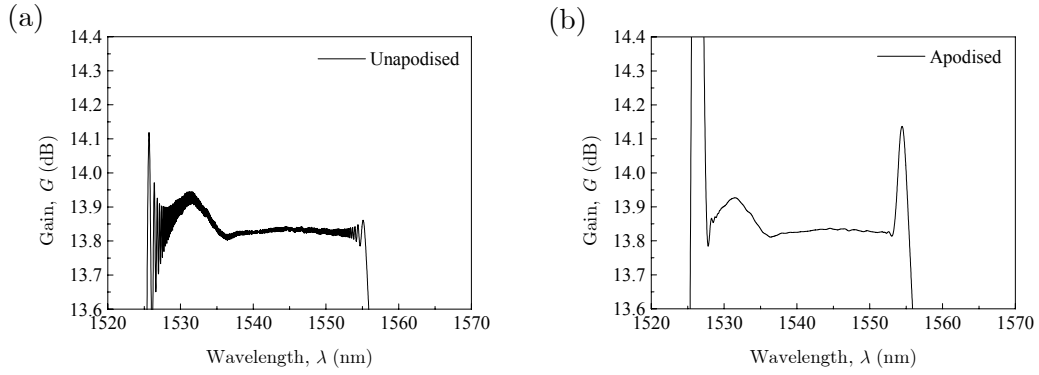

Fig. 2.3. (a) Gain profile flattened by an unapodised GFF, and (b) Gain profile flattened by an apodised GFF.

It can also be appreciated that a further reduction in the amplitude ripples can be obtained by increasing the percentage of the apodisation. Nevertheless, the hump width will monotonically increase as well, thus reducing the flat gain window. The effect of increasing the percentage of the apodisation is illustrated in Fig. 2.4(b).

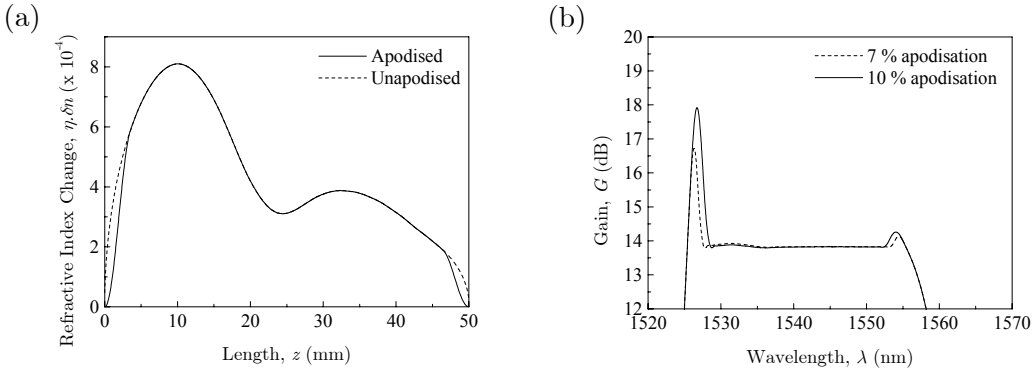

Fig. 2.4. (a) Overlay of refractive index modulations of unapodised and apodised gratings, and (b) Gain profiles flattened by gratings with 7% apodisation (dashed line), and 10% apodisation (solid line) respectively.

Both ends of these simulated 50 mm gratings are apodised to approximately 7% and 10% of their corresponding lengths respectively. As a consequence of this effect, the grating will require a higher chirp rate in order to retain a flat gain profile within the desired range of wavelengths. If the subsequent adjustment is carried out, it would however result in a lower overall gain.

One elegant approach to resolve the effect due to the apodisation process is to modulate the chirp rate itself within the apodisation regions to faithfully provide the exact transmission loss. This approach is validated by the simulation of the filtered gain spectrum, as shown in Fig. 2.5(a), while the revised chirp rate profile is shown in Fig. 2.5(b). Approximately 7% of the total lengths of these 50 mm grating models are apodised at each side.

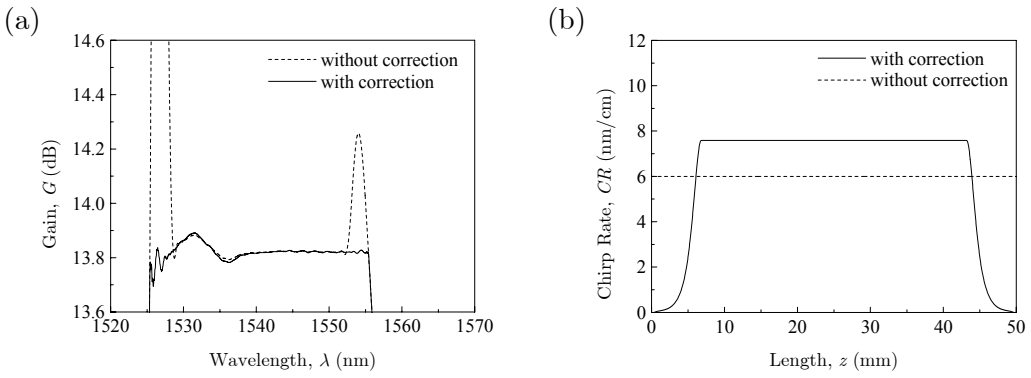

Fig. 2.5. (a) Gain profiles flattened by apodised GFFs with constant chirp rate (large humps) and with chirp rate corrections within the apodisation regions (no humps), and (b) Chirp rate profiles of the GFFs without any correction (constant values) and with corrections within the apodisation regions.

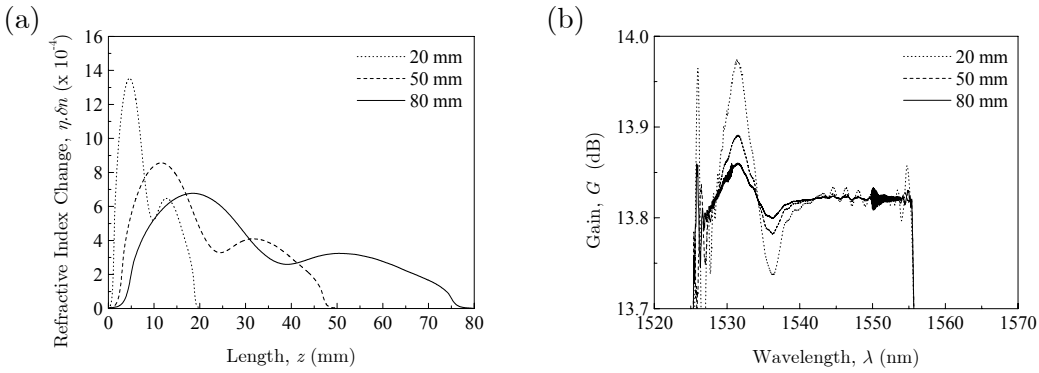

Fig. 2.6. (a) Refractive index modulations of three apodised gratings with lengths 20 mm, 50 mm and 80 mm, and (b) Gain profiles flattened by the three gratings.

A few gratings with different lengths have been simulated in order to demonstrate the importance of astute selection of the grating length. The lengths considered are 20 mm, 50 mm and 80 mm, where all of the gratings are 7% apodised at each end and their chirp rate profiles are also adjusted accordingly. The maximum refractive index change required decreases with increasing grating

length as illustrated by Fig. 2.6(a). It is then concluded that the length of the grating may confine the selection of the type of photosensitive fibres, on which the grating can be written, to only those that allow such a maximum refractive index change. On the other hand, there is only a slight difference in the flattened gain profile (Fig. 2.6(b)), thus this relaxes the constraint. Therefore, a compromise is only required between the achievable maximum refractive index by a particular fibre type and the packaging requirement.

2.3.2 Modulation of Grating Period with Uniform Refractive Index Change

Equation (2.1) also allows the synthesis of a nonlinear chirp rate profile of a grating with a constant refractive index change for providing varying transmission loss. However, having a constant refractive index change would result in ripples in the flattened gain profile, as illustrated in Fig. 2.7(a). Again, this can be explained by considering the internal interference due to the broadband reflection at the grating front and rear edges.

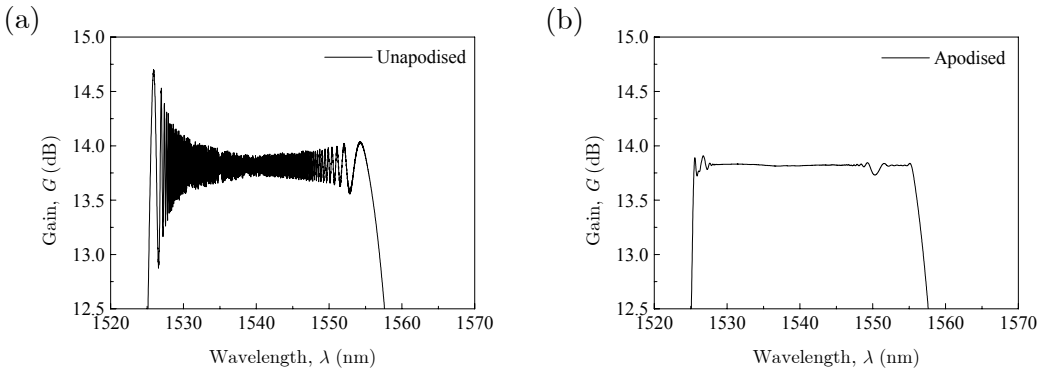

Fig. 2.7. (a) Gain profile flattened by an unapodised GFF, and (b) Gain profile flattened by a GFF with 7% apodisation at each end of the grating.

Apodisation can be applied to minimize the ripples, but corrections on the chirp rate modulation at the affected regions are necessary. The absolute

difference in the flattened gain profiles between the unapodised and the apodised gratings can be clearly seen in Fig. 2.7. Both gratings are 50 mm in length and the second grating is 7% apodised with a raised-cosine function. The necessary amendments to the chirp rate profile are shown in Fig. 2.8(a) for compensating the apodisation process on the refractive index change, shown in Fig. 2.8(b).

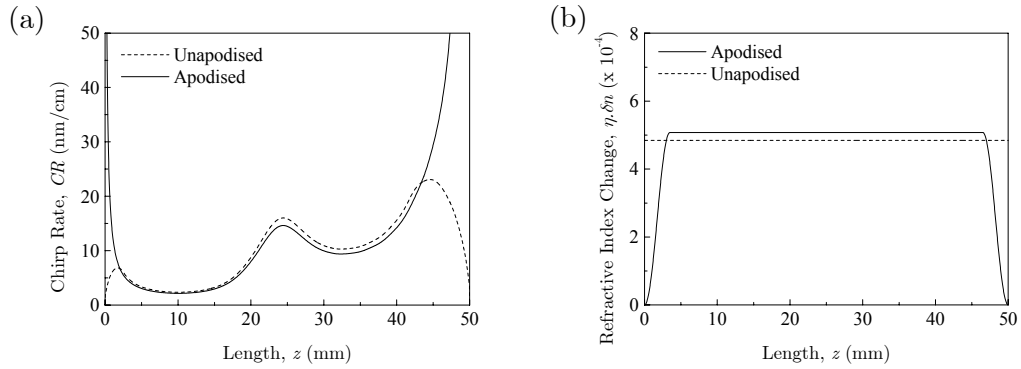

Fig. 2.8. (a) Overlay of chirp rate modulations of unapodised and apodised gratings, and (b) Refractive index profiles of unapodised (constant values) and apodised gratings.

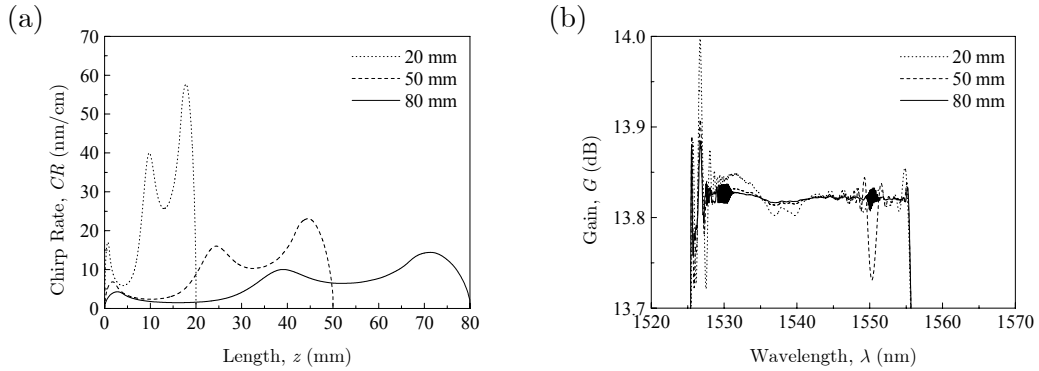

Fig. 2.9. (a) Chirp rate modulations of three gratings with lengths 20 mm, 50 mm and 80 mm, and (b) Gain profiles flattened by the three gratings.

The influence of the length of the grating on the chirp rate modulation profile is also simulated and is illustrated in Fig. 2.9(a), accompanied by the corresponding flattened gain profile (Fig. 2.9(b)). As anticipated, the maximum chirp rate decreases with increasing grating length. Moreover, the longer grating is found to produce a flatter gain profile with less amplitude ripples than the shorter gratings. The latter behaviour is also observed with the GFF from the first design.

The flatter gain profile exhibited by the longer gratings may arise from the reduction in the rate of change of the grating parameters. This corresponds to lower modulation values of the varying parameters. As a result, every point within the grating structure is associated with a narrower local stopband [77]. The overlapping between adjacent bands is reduced, thus decreasing the negative effect of interference. It is due to the same reason that a tiny hump is observed in the spectral region with higher gain slope. This region is associated with the parts of the grating that have relatively higher parameter values than the rest of the structure. Consequently, these parts could not match the desired transmission loss as well as the other parts. Finally, there is also a slight difference in performance between the two differently designed gratings. The grating from the second design noticeably produces a better gain flatness. It could be because the values of refractive index change in this design are lower for a given grating length, thus producing narrower local stopbands than those in the first design. Overall, both designs comfortably satisfy the requirement for WDM operation, which is no more than 0.2 dB.

2.3.3 Comparison of Designs from Transfer Matrix and Layer-Peeling Inverse Scattering Methods

The methodology used in the previous section provides an alternative approach to the renowned layer-peeling inverse scattering method [52]. The algorithms involved in the layer-peeling inverse scattering method need to be strictly followed, otherwise the synthesized grating profile will produce a distorted spectral response [52]. Consequently, there is no definite control of the grating

parameters. The graph in Fig. 2.10(a) shows the refractive index modulation that was obtained from the layer-peeling inverse scattering method. The grating has a constant chirp rate of 14.8 nm/cm and approximately 10% of the total length at each end of the structure was apodised with the Hanning function. Fig. 2.10(b) gives the flattened gain spectrum, which exhibits a gain variation of roughly 0.2 dB. The equivalent results obtained in the previous section are also overlaid in both graphs for the purpose of comparison. It can be seen that they are nearly identical. However, in the layer-peeling inverse scattering method, a longer time is required to process the necessary wide window of the targeted spectrum for avoiding spectral aliasing. Furthermore, in order to synthesize the chirp rate modulation of a grating while trying to retain a constant refractive index change, it would require exhaustive iteration. The higher complexity and processing time may merely produce an insignificant improvement to the gain flatness.

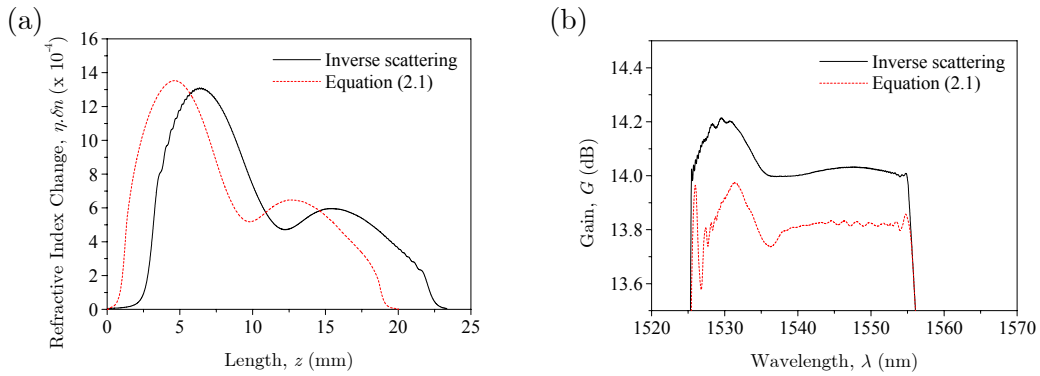

Fig. 2.10. (a) Refractive index modulations synthesized from the inverse scattering method and Equation (2.1) for apodised gratings with lengths around 20 mm and (b) Gain profiles flattened by the two gratings

2.4 Properties of Device

The utilisation of non-blazed short-period fibre Bragg gratings makes the proposed devices advantageous relative to the previous gain flattening approaches

due to their intrinsic features. They exhibit low temperature sensitivity (~10 pm/°C), although further improvement in temperature sensitivity can be obtained by exploiting the standard grating packaging. Also, enhanced thermal stability can be achieved through athermalisation. In comparison to those approaches that utilized blazed or long-period gratings, our approach demonstrates significantly lower sensitivity to fibre bending since the transmission loss required is not obtained through cladding or radiation mode coupling. It is also obvious that our GFFs are very compact indeed. Gain flattening of the entire EDFA spectrum is obtainable by simply using one short fibre grating. Consequently, it produces minimal insertion loss, which is also attributed to the fact that the device is a fibre-based passive component. Additionally, our GFF imposes relatively low fabrication complexity, which also makes it less costly. It is also flexible, in that its spectral response can be tailored to flatten arbitrary gain profiles of EDFA. Furthermore, it is believed to be polarisation insensitive, since fabrications of gratings with polarization dependent loss less than 0.1 dB and polarization mode dispersion less than 0.1 ps are now routine [84]. Last but not least, since the gain flattening operation is in the transmission configuration, its deployment does not require an optical circulator, which makes it reliable and reduces systems cost.

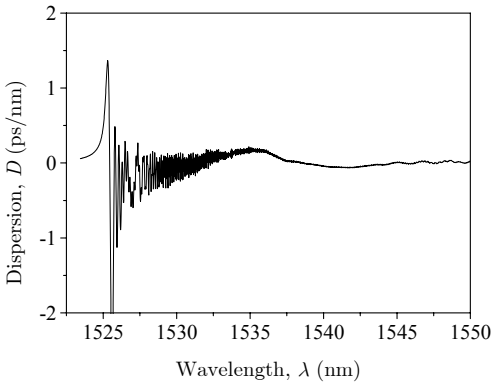

Fig. 2.11. Dispersion characteristic of signals at various wavelengths transmitted from the GFF with a nonlinear period and a uniform refractive index change.

Dispersion is found to be negligible for a majority of the bandwidth. The simulated result in Fig. 2.11 shows that the variation in this parameter is very small, except at the short wavelength edge of the wavelength band. Nevertheless, the relatively large dispersion in this region can be moved further away by expanding the device bandwidth of operation. However, overall gain has to be reduced accordingly to meet the requirement for a smooth transition of the index modulation. There is also an observable ripple, which is due to residual multiple scatterings inside the grating structure, where the wavelength signals are therefore highly delayed. Only the short wavelength signals suffer since they are considerably attenuated. This effect can be reduced by extending the apodisation length.

On the contrary, one may argue that back-reflection might degrade the EDFA and induce co-propagating Rayleigh backscattering [78]. Another potential drawback is that the GFF is only a static device. Therefore, it will be incompatible with optical networks with varying system conditions (e.g. signal power), which may be caused by system reconfiguration through channels adding or dropping and unintended variations in link loss.

Despite these potential drawbacks, some solutions are believed to be in hand. As it is known that an optical isolator is a prerequisite in every EDFA for performance optimisation, back-reflection is no longer a problem. Cladding mode loss can be suppressed through special design of the fibre used to write the grating [43]. This fibre should have a high core-cladding refractive index difference, high confinement factor and high numerical aperture. Alternatively, the fibre may also have a photosensitive cladding. In order to solve the problems caused by varying operating conditions, several trials have been reported. However, it should be noted that these trials concentrate only on the amplifier, none on the gain equalizer. These approaches comprise automatic-gain-control loops using control of the pump power [79] as well as gain locking using an out-of-band laser [80]. Other trials are to decouple the various signal channels by using twin core fibres [81], independent amplification of each signal channel [82] and cooling of the erbium-doped fibre in liquid nitrogen, thus converting it to an

inhomogeneously broadened amplifier [83]. Nonetheless, these techniques are costly and complicated.

2.5 Conclusions and Future Directions

A cursory glance at the simulation results reveals that satisfactory gain flatness is obtainable from the proposed devices (Fig. 2.6(b) and Fig. 2.9(b)). This confirms that a linearly chirped fibre Bragg grating with modulated refractive index or a fibre Bragg grating with modulated period and uniform refractive index can be satisfactorily used as a gain-flattening filter in transmission configuration. A gain excursion of less than the standard requirement for WDM operation (i.e. less than 0.2 dB) has been easily achieved. Both designs have been optimised to produce the highest average small-signal gain for a given bandwidth of operation. Also, both GFFs exhibit a reduction in the maximum gain and the average gain, but more importantly the useable operational bandwidth has been significantly increased.

The research should proceed with the fabrication of a prototype for evaluation of the proposed design. The continuous grating writing technique is believed to allow the production of a prototype grating with the pre-designed strength or chirp profile [84]. Nevertheless, the quality of the prototype should be expected to deviate from that of the theoretical design due to surrounding perturbations during the fabrication process, non-uniform cross-sectional refractive index change in the fibre core or inaccurate characterisation from measurement devices with inadequate resolutions [59].

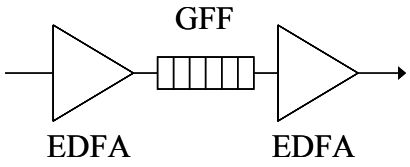

Fig. 2.12. The proposed GFF in two-stage erbium-doped fibre amplifier.

The GFF can also be designed for the use of two-stage EDFA (Fig. 2.12). In this configuration, the lossy GFF resides after the first stage amplifier, which would suppress its influence on the noise figure. The output power loss of the first stage amplifier caused by the GFF is compensated by the second stage amplifier, which also acts as a power amplifier. Overall, this configuration will improve the noise and gain characteristics of a single stage amplifier [5, 12].

WDM networks are also subject to being constantly reconfigured as the nature of the signal traffic in the system changes. The change governs the strength of the input signals to the amplifiers, which determines their level of saturation and of population inversion. Thus, the gain profile of the erbium-doped fibre amplifier will be proportionally altered. Furthermore, the input signal channels are coupled since the amplifier is predominantly a homogeneously broadened amplifier. Hence, the presence and absence of a given wavelength channel will affect the gain of a signal at another wavelength. On the other hand, passive filters are usually designed for a specific operating point of the erbium-doped fibre amplifiers. Thus, they are not necessarily that robust when system parameters vary and the spectral gain of the erbium-doped fibre they are compensating for, changes. This research is essentially a fundamental stage that may finally lead to the proliferation of a commercial cost effective reconfigurable GFF with optimal performance. Feedback loops may probably be accommodated to provide variation in the filter response based on the operating conditions. In this way, equalization can be provided which is robust with respect to changes in operating conditions.

Chapter 3

Reconfigurable Optical Code-Division Multiple Access Phase Encoder

3.1 Introduction

Future communication systems require higher speed and larger capacity transmission. Optical multiplexing techniques have been adopted to cater for these requirements. To date, wavelength-division multiplexing (WDM) and time-division multiplexing (TDM) have been successfully deployed. However, one could argue that WDM generates spectrally inefficient systems through dedication of one wavelength per user, while TDM requires strict temporal synchronization of the networks. Despite the seemingly almost unlimited bandwidth in current fibre systems, the available frequencies in the transmission band of an optical fibre will eventually be depleted if optical networks depend only on these conventional techniques. Therefore, more efficient multiplexing techniques have to be developed.

Recently, optical code division multiple access (OCDMA) has been identified as a possible alternative technique to solve the future wavelength resource problems. OCDMA can be overlaid onto the existing WDM networks to enhance network versatility. Moreover, it allows flexible bandwidth management, asynchronous operation, improved system security and the potential for much higher connectivity [23]. A number of technical approaches for performing the encoding/decoding process have been successfully demonstrated in recent years. These include the use of arrays of discrete optical waveguide-based delay lines

[22], arrays of optical waveguides with phase shifters [23], arrayed waveguide grating (AWG) [24], cascades of fibre gratings [26], and superstructured fibre Bragg gratings (SSFBGs) [28]. The development of the OCDMA systems also takes into account the extension of the code length, which directly determines the maximum number of channels. To date, 255-chip systems have been experimentally demonstrated [85]. Nevertheless, evolution of optical transmission systems to dynamically reconfigurable networks brings about an additional need for this multiplexing system to acquire tuning capabilities. It is appreciated that some of the previous approaches that utilise the planar lightwave circuits (PLC) technology may allow tunability. However, these devices are difficult and expensive to fabricate. Consequently, these requirements inspire further research to produce a reliable, simple and economical reconfigurable code generator for OCDMA systems.

A simple, yet effective reconfigurable device for phase encoding of optical signals is introduced in this chapter. Its characteristics will be thoroughly described through theoretical modelling, as well as laboratory experiments. This chapter ends with demonstrations of the device application in several OCDMA architectures.

3.2 Optical Code Division Multiple Access

In principle, this technique uses codes to define the channels in transmission systems. Each data bit to be transmitted is transformed into a sequence of pulses (or *chip*s) that forms an address code. This can be performed either in time domain (direct-sequence (DS) OCDMA) or frequency domain (frequency-hopping (FH) OCDMA). Fig. 3.1 provides the schematic representations of these procedures. In DS-OCDMA, either the intensity (amplitude-shift-keying (ASK)) or optical phase (phase-shift-keying (PSK)) of the chips can be used for encoding. On the other hand, the individual carrier frequency of each chip is varied accordingly in order to form a code in FH-OCDMA.

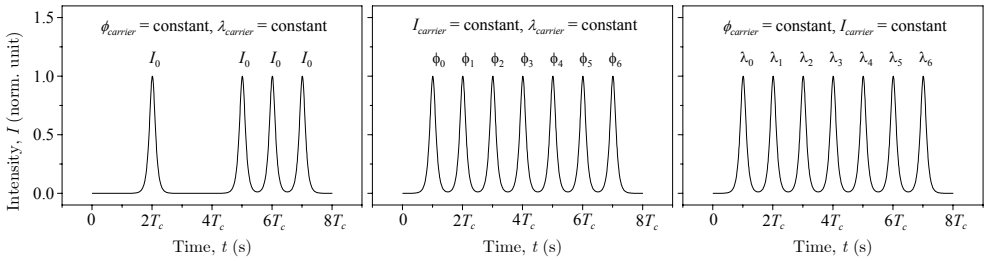

Fig. 3.1. Basic encoding schemes for optical code division multiple access: Amplitude coding (left), phase coding (middle), and frequency coding (right) where I_i is the carrier intensity, ϕ_i is the carrier phase, λ_i is the carrier wavelength, and T_c is the chip period/duration.

The encoded signal $f(t)$, is given by the convolution between data signal $S(t)$, and code $X(t)$, as follows [23]:

$$f(t) = X(t) \otimes S(t) \tag{3.1}$$

where $X(t) = \sum_{i=1}^{N} a_i \cdot \delta\left(t - T_c(i-1)\right)$ and $S(t) = e^{j\omega_0 t} \cdot \sum_{k=1}^{M} p_k \cdot u\left(t - T_b(k-1)\right)$.

In $X(t)$, $\delta(t)$, N and T_c stand for delta function, number of elements and time interval between each elements of the code, respectively. a_1, a_2, …, a_N represent elements of the encoding code, which may be in a form of, for example, frequency, amplitude or phase. In $S(t)$, $u(t)$, p_k and T_b are waveform of pulse, payload data and bit time, respectively.

Only a specifically designed decoder can unambiguously recognise a particular encoded data stream, which is achieved simply by matched filtering. The decoded signal $g(t)$, is given by

$$g(t) = S(t) \otimes C_{XY}(t) \tag{3.2}$$

where $C_{XY}(t) = X(t) \otimes Y(t)$ and $Y(t) = \sum_{i=1}^{N} b_i \cdot \delta\left(t - T_c(i-1)\right)$.

In $Y(t)$, b_1, b_2, …, b_N represent elements of the decoding code. $C_{XY}(t)$ will have the waveform of the auto-correlation function of the code if $Y(t)$ is identical to $X(-t)$. Ordinarily, the corresponding signal $g(t)$, has a large peak at every centre of specified bits of mark (data '1'). On the contrary, $g(t)$ will not have a large peak at any bit when $Y(t)$ is different from $X(-t)$. In this case, $C_{XY}(t)$ has the waveform of cross-correlation function of the two codes. Therefore, a specific signal can be extracted from multiplexed signals through thresholding procedures.

3.3 Reconfigurable Phase Code Generation

3.3.1 Principle of Operation

Grating writing technology has advanced to a stage where precise control of the strength and phase profile of the device is now possible. Ordinarily, a phase-shifted grating is formed by shifting the phase of the rapidly varying refractive index during the grating writing process. Since optical phase is a function of the effective refractive index, a phase shift can also be imposed on the reflected light by introducing a localised variation of this parameter along the propagation path. Apparently, the effective index of a propagating mode is both temperature and strain sensitive. This is dictated by the following equation [43]

$$\Delta n_{eff} = \frac{\partial n_{eff}}{\partial T} \cdot \Delta T + \frac{\partial n_{eff}}{\partial \sigma} \cdot \Delta \sigma \tag{3.3}$$

where $\partial n_{eff} / \partial T$ is the temperature coefficient of refractive index, ΔT is the change in temperature, $\partial n_{eff} / \partial \sigma$ is the longitudinal stress optic coefficient, and $\Delta \sigma$ is the applied longitudinal stress. The stress however needs to be cautiously applied to the fragile grating and is difficult to adjust. On the other hand, heating can easily be controlled and spatially confined. In addition, heating may also produce stress as a result of volume expansion. The thermal expansion coefficient of silica α_T is approximately 0.55×10^{-6} /°C, whereas $\partial n_{eff} / \partial T$ is roughly 5.2×10^{-6} /°C. Therefore, the contribution of the thermo-optic effect should be far greater than the thermo-elastic effect. Moreover, the temperature-

induced index variation is impermanent, as long as the temperature does not exceed the grating erasure temperature (~150 °C). Conclusively, applying adjustable heating would be an effective method to control the phase shift imposed onto the propagating mode.

This procedure can be further exploited for phase encoding in DS-OCDMA systems. A reconfigurable code generator with multiple phase shifts can be formed by deploying several variable heating elements at equal intervals along a uniform fibre Bragg grating. The spatial phase profile of the device can be altered to generate a desired code by simply adjusting the temperature at these chip boundaries. A signal pulse can thus be directly transformed into a coded pulse sequence upon reflection from the device.

3.3.2 Device Modelling

Two approaches can be used to model the proposed reconfigurable code generator. In the first approach, the temporal and phase responses of an encoded optical pulse are used to represent the characteristics of the encoder/decoder. On the other hand, the second approach uses the transfer matrix to exactly describe the device. The phase variation at the chip boundary is assumed to be a slowly varying function of length, based on the kinetic theory of heat. Generally, the theory states that the heat distribution between two points varies linearly. However, in a small scale, a wire has a significant cross-sectional area, thus the heat gradient will be modified by the heat radiation from the whole surface. Simultaneous heat transfer via convection will also add pedestals to the heat distribution profile. Therefore, it is reasonable to assume that a hot wire will produce a heat distribution profile that takes a hyperbolic secant shape in an optical fibre. In the simulation using the transfer matrix method, the effect of a given heat distribution can be also modelled by modulating the local Bragg wavelengths accordingly through its direct relationship with the modified effective refractive index in the phase-matching condition ($\lambda_B = 2n_{eff}\Lambda$). Fig. 3.2 shows the Bragg wavelength profile in the vicinity of a number of localised heating points.

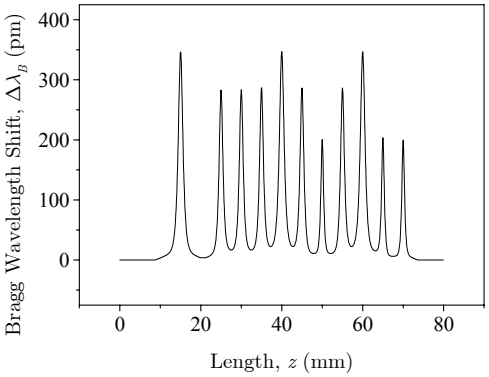

Fig. 3.2. The heat-induced Bragg wavelength modulation.

In accordance with the phase-matching condition, a variation in the local effective refractive index Δn_{eff} , will appear as a shift in the local Bragg wavelength $\Delta\lambda_B$, such that

$$\begin{aligned}\Delta\lambda_B &= 2\cdot\Delta n_{eff}\cdot\Lambda \\ &= \frac{\Delta n_{eff}}{n_{eff}}\cdot\lambda_B\end{aligned} \tag{3.4}$$

where λ_B is the grating's initial Bragg wavelength, $\Lambda = \lambda_B / 2n_{eff}$ is the period of the grating and n_{eff} is the effective refractive index of the core. The variation in the effective refractive index will also cause a phase change $\Delta\phi$ to the propagating light, given by

$$\begin{aligned}\frac{\Delta\phi}{2} &= \Delta\beta\cdot\Delta z \\ &= \frac{2\pi}{\lambda_B}\cdot\Delta n_{eff}\cdot\Delta z\end{aligned} \tag{3.5}$$

where Δz is the length of a very small grating subsection and $\beta = 2\pi n_{eff} / \lambda_B$ is the propagation constant. Therefore, combining Equation (3.4) and Equation (3.5) will give the accumulated phase shift $\Delta\phi$, associated with each Bragg wavelength variation at the chip boundary, as follows

$$\Delta\phi \approx \frac{4\pi n_{eff}}{\lambda_B^{\ 2}} \sum_i \Delta\lambda_{Bi} \cdot \Delta z_i \tag{3.6}$$

where i denotes the associated local parameters. Either the overall Bragg wavelength profile or the multiple gradual phase shifts can be incorporated into the piecewise uniform analysis (transfer matrix method) to efficiently calculate the complex reflection coefficients of the device. Fourier transformation of the product of the complex reflection coefficients with the spectral response of the transmitted pulses will then give the auto-/cross-correlation.

The heating element changes its temperature because of the transformation from the electrical energy to heat energy, in compliance with the principle of energy conservation. This temperature rise causes variation in resistance that leads to a non-linear voltage-current characteristic. The ratio of a specific voltage over the corresponding current will give the resistance of the conductor at that operating temperature. An example of the variation of resistance with current is plotted in Fig. 3.3, which exhibits an excellent resemblance to an exponential function. Therefore, this relationship can be mathematically expressed as,

$$R = R_0 \cdot e^{c_0 I} \tag{3.7}$$

where c_0 is the fitting constant and R_0 is the small-signal resistance, which can also be calculated from

$$R_0 = \frac{\rho_0 \cdot l}{A} \tag{3.8}$$

where ρ_0 is the resistivity at room temperature (tungsten: $5.4 \times 10^{-8}\,\Omega\text{m}$), l is the length and A is the cross sectional area of the conductor.

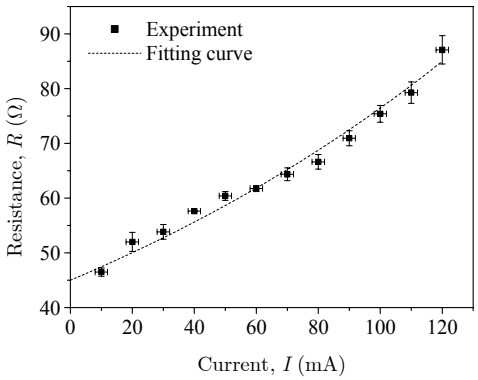

Fig. 3.3. Resistance against current for a tungsten wire with a length of 20 cm and a diameter of 18 μm. The fitting function (Equation (3.7)) uses $R_0 = 45\,\Omega$ *and* $c_0 = 5.3 \times 10^{-3}$ *. The fitted small-signal resistance* R_0 *is close to the calculated value of 42.44 Ω from Equation (3.8).*

On the other hand, the temperature coefficient α, of resistivity is defined as,

$$\alpha = \frac{1}{\rho} \cdot \frac{d\rho}{dT} \tag{3.9}$$

where T is the temperature and ρ is the resistivity. The solution to this equation assumes an exponential form. Since the resistance is proportional to the resistivity, the solution can be rewritten as,

$$R = R_0 \cdot e^{\alpha \cdot \Delta T} \tag{3.10}$$

where ΔT is the temperature change (Tungsten: $\alpha = 4.8 \times 10^{-3}\,\mathrm{K}^{-1}$). By comparing this equation to Equation (3.7), it is evident that the current is directly proportional to the temperature change. Moreover, following the fact that the temperature change shifts the local Bragg wavelength, it is worth recognising that the current is therefore directly proportional to the peak shift in the Bragg wavelength modulation, but not to the phase shift. The latter behaviour can be observed in the variation of the acquired phase shift with the temperature (or current) as illustrated in Fig. 3.4.

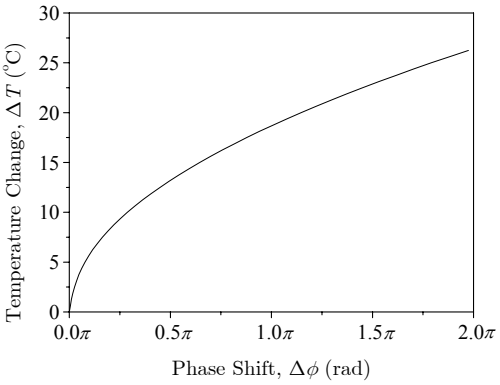

Fig. 3.4. Analytical model of the temperature change as a function of the acquired phase shift.

3.3.3 Description of Device

Gratings with various lengths have been used to investigate the idea of this reconfigurable code generator. The uniform Bragg gratings used for the demonstration are 10 mm, 40 mm and 80 mm long and are written in a standard telecom compatible fibre with an $NA \approx 0.12$. The uniform coupling coefficients in the gratings are ~81 m^{-1}, ~33 m^{-1} and ~12 m^{-1} respectively. The gratings are written using our continuous grating writing technique operated with CW UV light at 244 nm. Thin tungsten wires (18 μm or 25 μm diameter) are wrapped around or laid on top of the grating to ensure a firm contact in a small confined area. A single N-chip code generator with a chip-duration of T_c s is constructed by positioning N-1 parallel tungsten wires L_c m apart along the fibre grating with the first wire being placed L_c m into the grating, where

$$T_c \approx \frac{2n_{eff}L_c}{c} \tag{3.11}$$

where c is the speed of light in free space. In the real device configuration, the amount of temperature rise is controlled independently by varying the current

flow with a variable potentiometer inserted in each parallel circuit. In addition, the fibre grating can be mounted on a stretcher to allow tuning of the grating's central wavelength. The structure of the proposed device is illustrated in Fig. 3.5.

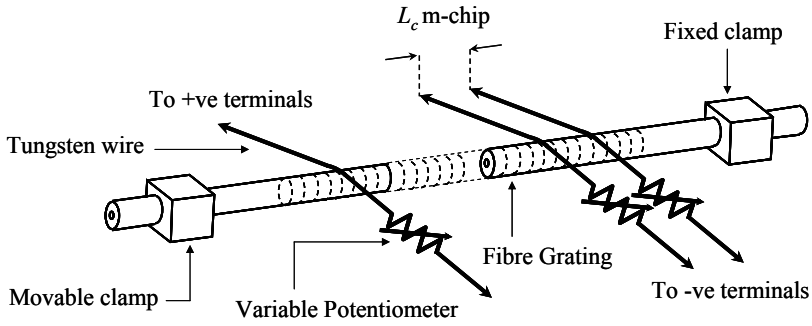

Fig. 3.5. Schematic structure of the reconfigurable encoder/decoder.

3.3.4 Characterization of the Device

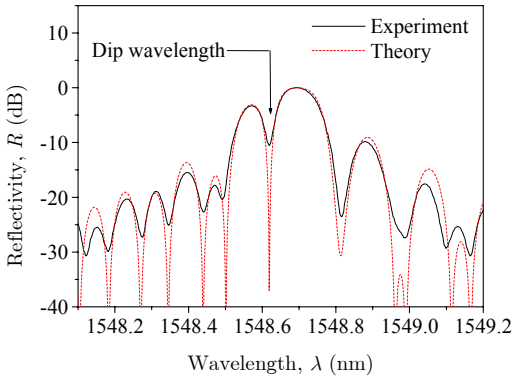

Fig. 3.6. Spectral reflectivity response when a π -phase shift is induced at the centre of a 10 mm uniform grating.

The phase response of the device with current can be determined through experimental observation of the dynamic behaviour of the grating spectrum under heat treatment. One of the traceable varying features is the dip wavelength within the grating bandwidth. This feature corresponds to a very narrow linewidth transmission loss within the grating passband, as illustrated in Fig. 3.6. Fig. 3.7 and Fig. 3.8 show this behaviour for 10 mm and 40 mm gratings respectively with their corresponding simulated phase responses. The acquired phase shift can thus be deduced from the measured excursion, relative to the grating's initial Bragg wavelength, by calibrating with the simulation curves.

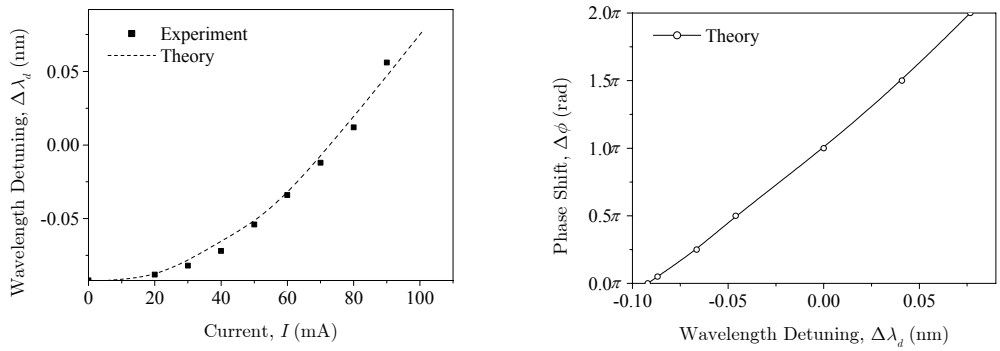

Fig. 3.7. *Phase response with dip wavelength detuning of the 10 mm grating.*

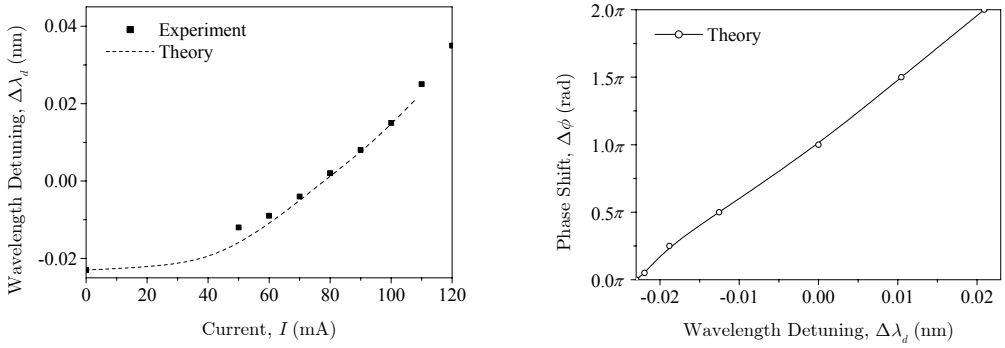

Fig. 3.8. *Phase response with dip wavelength detuning of the 40 mm grating.*

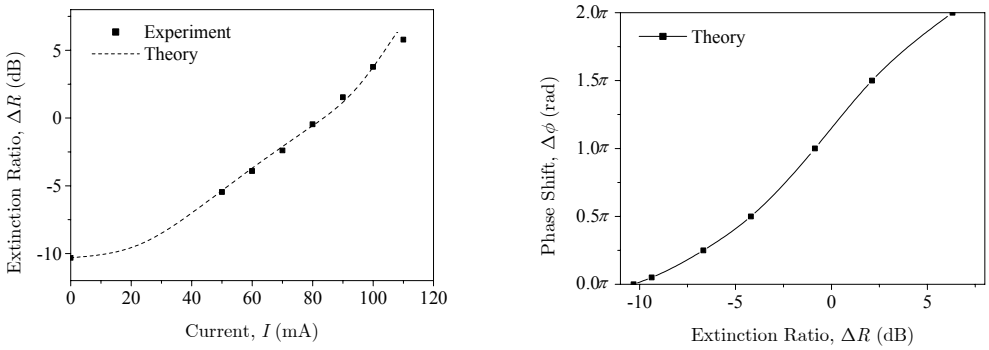

Fig. 3.9. Phase response with extinction ratio between main and left lobes for the 40 mm grating.

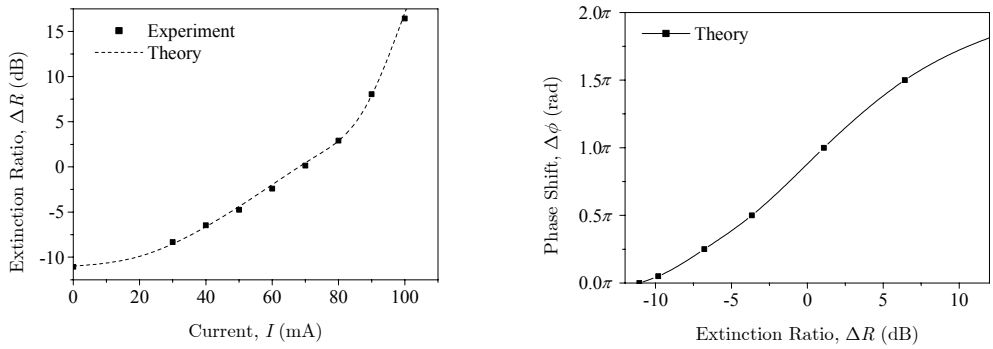

Fig. 3.10. Phase response with extinction ratio between main and left lobes for the 80 mm grating.

However, when the bandwidth of the grating under investigation is narrow, this approach is unlikely to be accurate due to high sensitivity to variation of the surrounding temperature. The study has also discovered that the height difference between two adjacent side-lobes or between the main and the first left side-lobe can be indirectly used to extract the required information. Similarly, comparison with their simulated responses will determine the magnitude of the phase shift for a given current. This approach has been satisfactorily

demonstrated on 40 mm and 80 mm gratings. Their measured and simulated responses are illustrated in Fig. 3.9 and Fig. 3.10 respectively.

3.4 Device Implementation in OCDMA Architectures

The proposed reconfigurable code generator has been included in several systems of various configurations to demonstrate its potential in OCDMA implementations. Initially, a simple encode-decode experiment is demonstrated in which this form of device is used at both the transmitting and receiving sides. In this demonstration, only bipolar phase shift keying (BPSK) is used. Then, the code sequence generation is enhanced in the subsequent experiment by employing a quaternary phase shift keying (QPSK) configuration and extending the number of chips. The reliability of its code generation is also confirmed in this experiment through evaluation of the code recognition by superstructured grating decoders. Finally, this device is applied in a system with a bi-directional add/drop configuration.

3.4.1 All-Reconfigurable Coders Configuration

The tuning characteristic for the devices used in this configuration is deduced from measurements of the dip wavelength detuning. For this particular experiment, only the electrical current to produce a π-phase shift is required for bipolar phase shift keying operations. The measured value has been validated through simulations, as shown in Fig. 3.11.

The gratings used in this system are both 40 mm long with peak reflectivity of about 75% corresponding to a uniform coupling coefficient in the grating of approximately 33 m^{-1}. Seven tungsten wires with 25 μm diameter are wrapped tightly around the grating at equal distance of 5 mm apart. Consequently, an 8-chip encoder/decoder with a chip-duration of 50 ps is obtained.

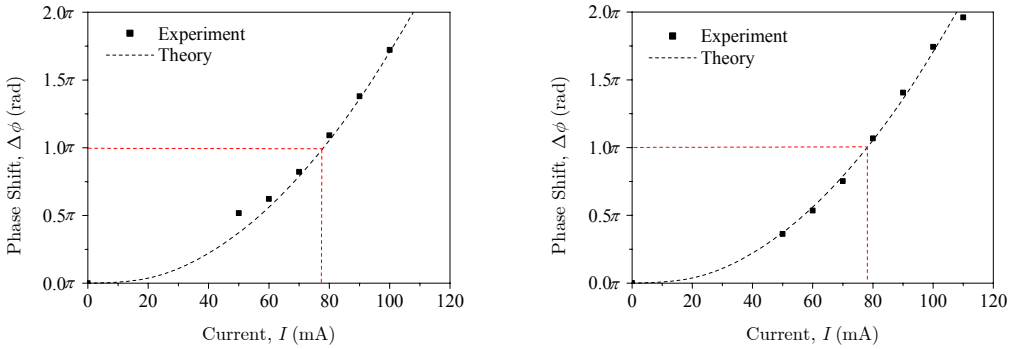

Fig. 3.11. Phase shift as a function of current deduced from the dip wavelength detuning (left) and from the extinction ratio between main and left lobes (right).

When a current flows in each wire, the electrical energy will be eventually converted into heat energy. The heat is transferred to the optical fibre through processes of radiation, conduction and convection. This will result in a heat distribution profile that resembles a hyperbolic secant function within a finite length. Consequently, the local effective refractive index is modified according to the thermo-optic effect. Light that passes through this region will then acquire a phase shift equal to the amount given in Equation (3.6).

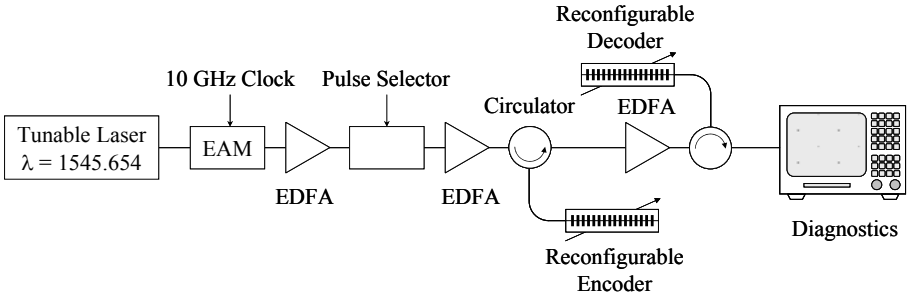

Fig. 3.12. Experimental setup.

The experimental setup for the system is shown in Fig. 3.12. CW signals from a tunable laser source are passed through an electro-absorption modulator (EAM)

to generate a 10 GHz pulse train of 20 ps pulses before being amplified and passed through an electro-optic modulator (EOM), generating 20 ps pulses at a repetition rate of 622 MHz. These pulses then are fed into the reconfigurable encoder. *M*-sequences or also known as *maximal length sequences* are used in this experiment to provide the codes. Codes with lengths of $2^L - 1$ can be generated by a number of L shift registers or delay elements [86]. This scheme is chosen as it is the most basic bipolar coding scheme and it can produce a sufficient auto-correlation contrast between the peak and the sidelobes. It can only provide a pair of perfectly *orthogonal* codes (for example, an orthogonal code to "*0*, π, *0*, *0*, π, π, π" would only be "π, *0*, π, π, *0*, *0*, *0*") . However, it can still produce low cross-correlations between the other *quasi-orthogonal* codes. An *M*-sequence "*0*, π, *0*, *0*, π, π, π, *0*" is tuned into the uniform grating by heating the appropriate wires in accordance with the tuning characteristics shown in Fig. 3.11. Hence, the π-phase shift is obtained at a current value of 78 mA. The time-response of this code is shown in Fig. 3.13(a). At the receiving side, the other 40 mm uniform grating was tuned to the inverse code "*0*, π, π, π, *0*, *0*, π, *0*" to perform the decoding action. The time-response of this code is shown in Fig. 3.13(b).

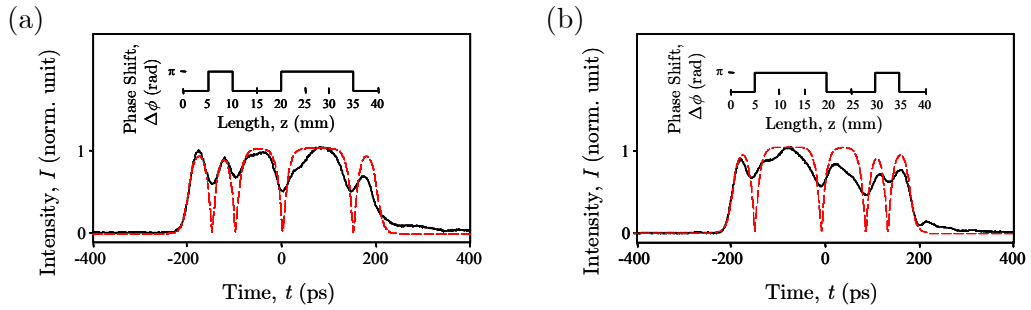

Fig. 3.13. Oscilloscope traces (measured: solid line and calculated: dashed line) after reflection off the grating configured to the bipolar phase code shown in the inset.

The auto-correlation of the measured decoded signal is shown in Fig. 3.14(a) (solid line) showing only a slight broadening from the theoretically expected pulse

(dashed line in Fig. 3.14(a)). By tuning the decoding grating to a quasi-orthogonal code sequence "*0, 0, π , 0, 0, π , π , π* " the quality of the cross-correlation could also be assessed (Fig. 3.14(b)), again confirming only a slight broadening compared to the theoretically predicted time response.

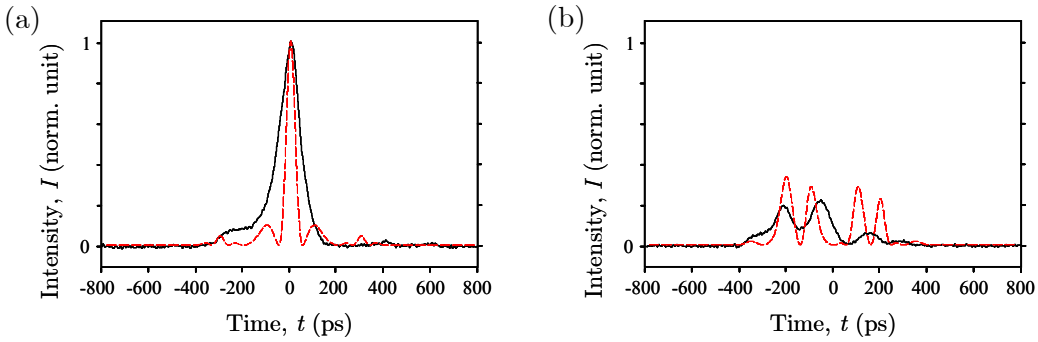

Fig. 3.14. Traces of (a) the intensity auto-correlation, and (b) the intensity cross-correlation of the 20 ps input pulses subjected to "0, π , 0, 0, π , π , π , 0" phase coding (measured: solid line and calculated: dashed line).

3.4.2 Reconfigurable and Fixed Superstructure Bragg Grating Coders Configuration

Quaternary phase shift keying is attempted in this experiment as a means to expand the available codes. Therefore, predetermination of the values of the electrical current for 0.5π , π and 1.5π phase shifts is necessary. However, it was impossible to get the magnitude of phase shift out of the dip wavelength detuning since the measurements deviated considerably from the theoretical curve. At this stage of the research, the theoretical model of the device had not been extensively studied. Consequently, a crude assumption was made regarding the tuning characteristic of the device in order to allow the experiment to proceed with the quaternary phase shift keying operation. The assumption was that a very well confined heating was realised at every chip boundary by using wires with 18 μm diameter. It follows that the increase in the effective refractive index should be

constant along a very small length of fibre which touches the wire. Since the phase shift is proportional to the integral of the Bragg wavelength profile along the fibre as implied by Equation (3.6), it is now directly proportional to the temperature of the wire. It has been verified in Section 3.3.2 that the temperature change varies linearly with current, thus the phase shift can be said to be proportional to the current. Additionally, the π-phase shift was assumed when the height difference between the first and second sidelobes was at a maximum. The remaining magnitudes of phase shifts were obtained through linear extrapolation. As a result, the values of electrical current used to produce 0.5π, π and 1.5π were 30 mA, 60 mA and 90 mA respectively.

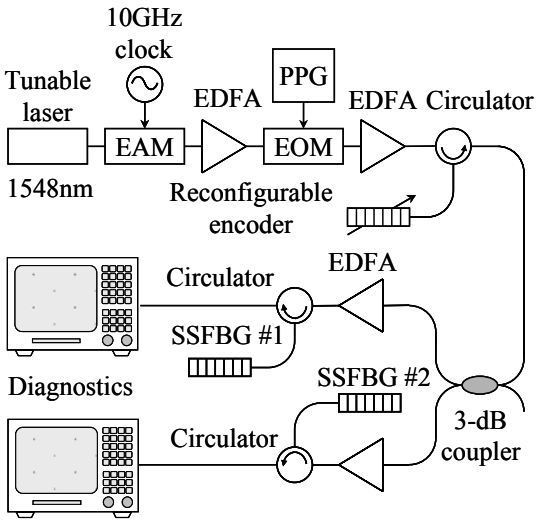

Fig. 3.15. Experimental setup.

The experimental setup is shown in Fig. 3.15. The transmitter consists of a tunable laser operated at 1548 nm, an electro-absorption modulator (EAM), an electro-optic modulator (EOM) and a reconfigurable optical encoder (as described above). The EAM is used to generate a 10 GHz pulse stream with the full width at half maximum (FWHM) of 20 ps. The pulse stream is amplified and passed through the EOM, reducing the repetition rate to 622 MHz. Reflected pulses from the encoder are then split into two arms of a 3-dB coupler, each consisting of a

superstructured fibre Bragg grating (SSFBG) decoder of different phase sequence. The transmitted pulses are pre-amplified by an optical amplifier before being decoded and received by a photo-detector. Output signals are observed on an oscilloscope. Additionally, the bit-error-rate performance of the system is tested by feeding electrical data from a pseudo-random pattern generator (PPG) into the EOM, while an error-detector is connected at the receiver. The reconfigurable encoder is set to the inverse code sequence with respect to either one of the SSFBG decoders so that the time-reversal operation can be performed. This is done by independently adjusting the electrical current flow at the chip boundaries to their associated values. The pulses are then modulated to this phase code, upon reflection from the grating, via a circulator.

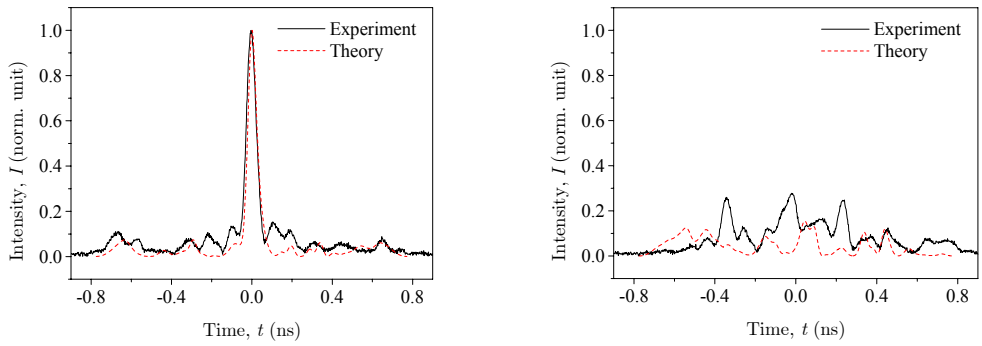

Fig. 3.16. Traces of the intensity auto-correlation (left) and the intensity cross-correlation (right) of the 20 ps input pulses subjected to phase code "0, 0, 0, 1.5π , 1.5π , 0.5π , 1.5π , 0.5π , 0, π , 1.5π , 0.5π , 0, 0.5π , π , π " (measured: solid line and calculated: dashed line).

The 16-chip QPSK coded pulse stream is individually decoded by the SSFBGs at the receiver, both operating at the same central wavelength of 1548 nm. Fig. 3.16 shows the relative intensity distribution of a bit of the decoded signal in the matched and unmatched cases for the SSFBG with address code "*0, 0, 0, 1.5π , 1.5π , 0.5π , 1.5π , 0.5π , 0, π , 1.5π , 0.5π , 0, 0.5π , π , π*". On the other hand, Fig. 3.17 represents that of the SSFBG with address code "*0, 0, 0.5π ,*

π, *0.5*π, *1.5*π, π, *0*, π, *0.5*π, *0*, *0.5*π, *1.5*π, *0*, π, *0*". The overall extinction ratio between auto- and cross-correlation is found to be approximately 71%.

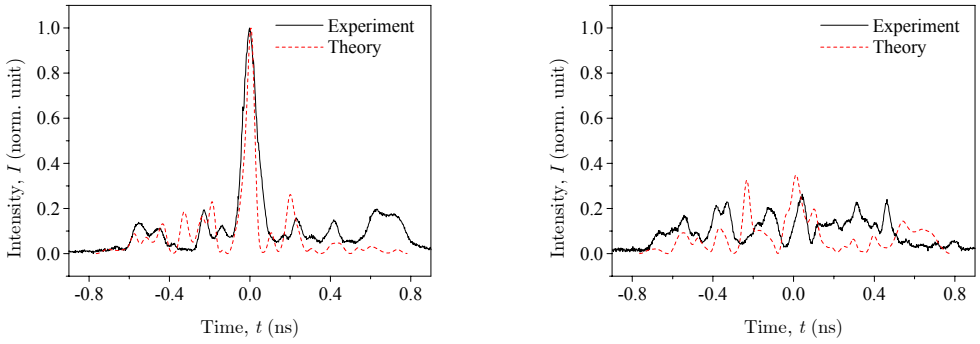

Fig. 3.17. Traces of the intensity auto-correlation (left) and the intensity cross-correlation (right) of the 20 ps input pulses subjected to phase code "0, 0, 0.5π, π, *0.5*π, *1.5*π, π, *0*, π, *0.5*π, *0*, *0.5*π, *1.5*π, *0*, π, *0" (measured: solid line and calculated: dashed line).*

Additional power loss of the recovered signals is anticipated for OCDMA systems employing the proposed reconfigurable encoder. This stems from the fact that each phase shift may not be exactly discrete as it is distributed over a finite length. The power loss will further deteriorate if the concerned phase sequences are not entirely accurate. The tuning characteristic for the 80 mm grating, deduced from the extinction ratio between main and left lobes of its reflectivity spectrum, is shown in Fig. 3.18. It reveals that the acquired phase shifts for the current values used are instead 0.14π, 0.62π and 1.61π respectively. Subsequently, the realised phase sequences differ from the intended phase sequences and are illustrated in Fig. 3.19.

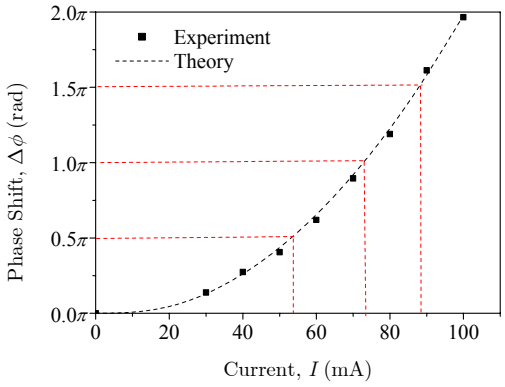

Fig. 3.18. Phase shift as a function of current deduced from the extinction ratio between main and left lobes.

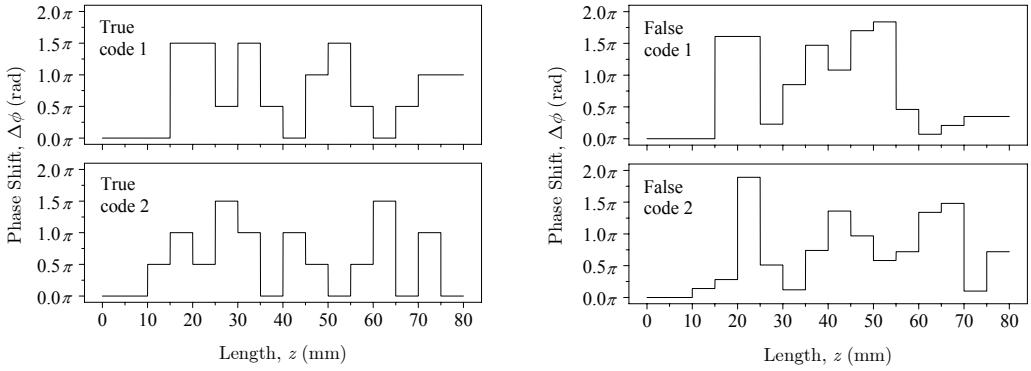

Fig. 3.19. Intended 4-level phase code sequences (left) and their actual phase sequences (right) after analysis.

As a consequence, the intensity of the acquired auto-correlation is far away from the ideal. The relative intensity reduction can be appreciated from Fig. 3.20. This estimation is supported by the bit-error-rate measurements for the two codes, presented in Fig. 3.21. The power penalty of approximately 2.5 dB, with respect to the laser back-to-back response, is observed. In addition, Fig. 3.20 also indicates that the power loss will be accompanied by a slight pulse broadening. The analytical auto-/cross-correlations of the device, reconfigured to the false

phase codes, show a reasonable agreement with their measured responses in Fig. 3.16 and Fig. 3.17.

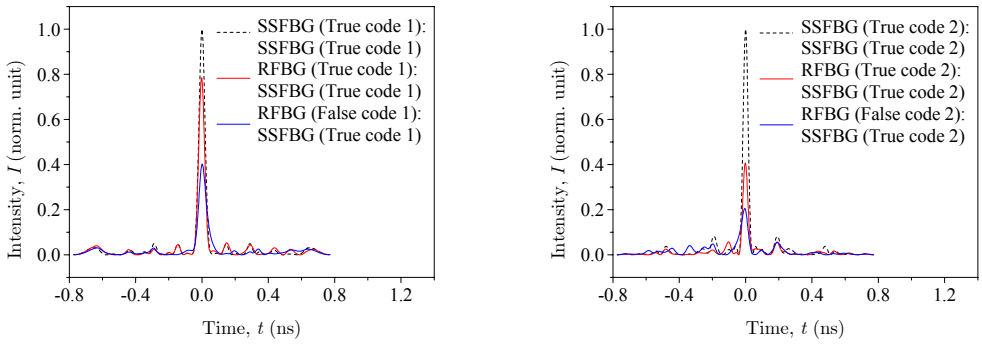

Fig. 3.20. Simulated traces of the intensity auto-correlation due to inclusion of the reconfigurable encoder tuned to the accurate QPSK codes and also to those realised in the experiment (SSFBG and RFBG stand for superstructured and reconfigurable fibre Bragg grating respectively).

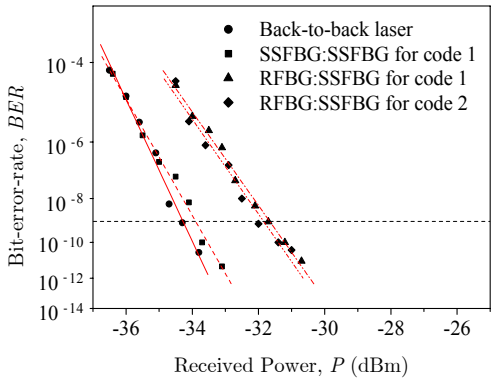

Fig. 3.21. Bit-error-rate measurements under the influence of the reconfigurable encoder in comparison to that using a superstructured grating encoder and also for the back-to-back laser (SSFBG and RFBG stand for superstructured and reconfigurable fibre Bragg grating respectively).

Despite this error, good autocorrelations (Fig. 3.16 and Fig. 3.17) and wide eye diagrams (Fig. 3.22) measured in this demonstration, sufficiently justify its practical implementation. This also indicates high tolerance of the device to offsets in the phase shifts, yet the low cross-correlations confirm its excellent channel selectivity. Most importantly, considerable improvement to the recovered signals is expected as predicted by simulations.

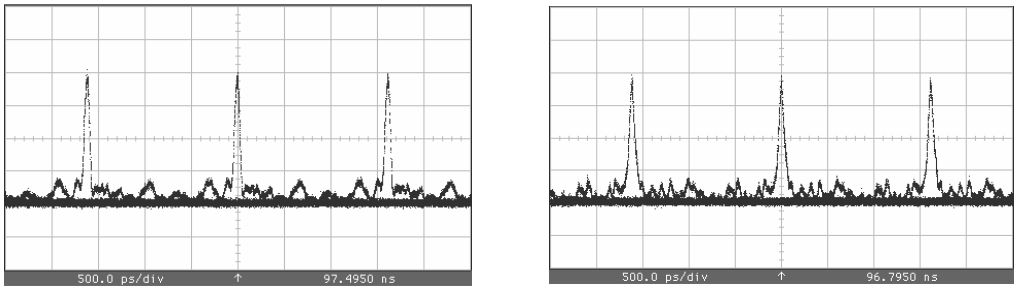

Fig. 3.22. Eye diagrams obtained when the encoder is reconfigured to the attempted phase sequence c1 (left) and c2 (right).

The effect of misallocation of the phase shifts from their correct positions is also theoretically investigated. In this analysis, initially, the phase shifts in a 16-chip encoder with 5 mm chip-length are all displaced by the same amount and direction. This condition is intuitively chosen because it could be the main source of error, derived from the mounting procedure. While constructing the device, the spacing between heating wires can be precisely determined, but the exact location of the grating is a bit uncertain. Nevertheless, the results shown in Fig. 3.23(a) suggest that the effect is negligible for misallocation of up to 60% of the chip length. It could be because only the first and last chips, in effect, have false chip-durations, thus they do not have a significant effect on the relatively large number of the total chips. However, for an encoder with the same chip-length but fewer chips, the influence of the phase shifts' misallocation decreases as the channel selectivity becomes slightly poorer [28]. In addition, the sensitivity to the phase shifts' misallocation increases as the chip-length is reduced while the number of chips is kept the same. The variations of the normalised intensity

auto-correlation as a function of phase shift misallocation distance, due to changes in chip-length and number of chips, are illustrated in Fig. 3.23(b). Another potential effect to study is the erratic misallocations of the phase shifts. This corresponds to an inconsistent amount and direction of displacements of the phase shifts.

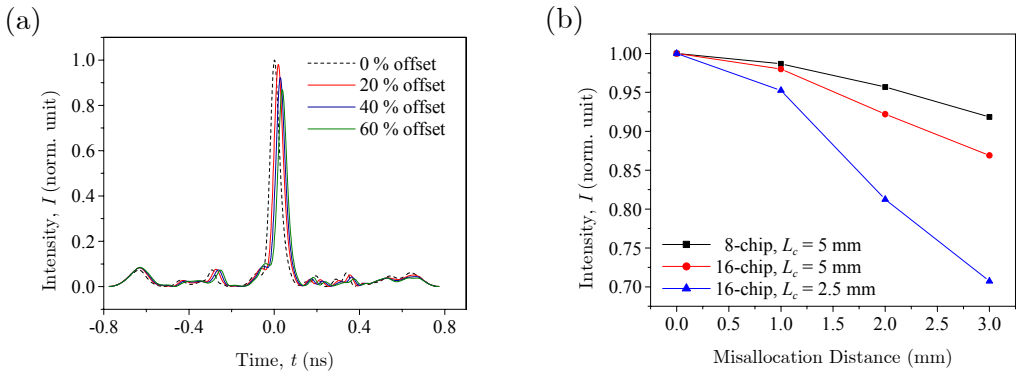

Fig. 3.23. (a) Variation of the traces of the intensity auto-correlation as a result of misallocation of the phase shift, and (b) the intensity auto-correlation against phase shifts misallocation distance for various chip-lengths and numbers of chips.

3.4.3 Bi-directional Clock Distribution Architecture

This experiment demonstrates the application of the reconfigurable encoder/decoder in an enhanced OCDMA system. The system configuration of the previous experiment is expanded to include add/drop and bi-directional operations. The experimental setup of the system is illustrated in Fig. 3.24. Two WDM carriers at 1548.07 nm and 1548.87 nm are simultaneously modulated by an electro-absorption modulator to generate two independent 10 GHz pulse trains of 20 ps width. Only the optical carrier operating at 1548.07 nm is fed with electrical data from a pseudo-random pattern generator (PPG1), by an electro-optic modulator (EOM). Encoding procedure of the data stream is then performed by a reconfigurable encoder tuned to a specific phase code sequence.

Their intensities are also carefully equalised to ensure uniform signal-to-noise ratios. The two carriers are then multiplexed before being broadcast onto a 10 km optical link of dispersion shift fibre (DSF). On the other end of the link, the encoded data stream is unambiguously decoded by a superstructured grating decoder with the inverse phase code sequence (SSFBG #1 or SSFBG #2).

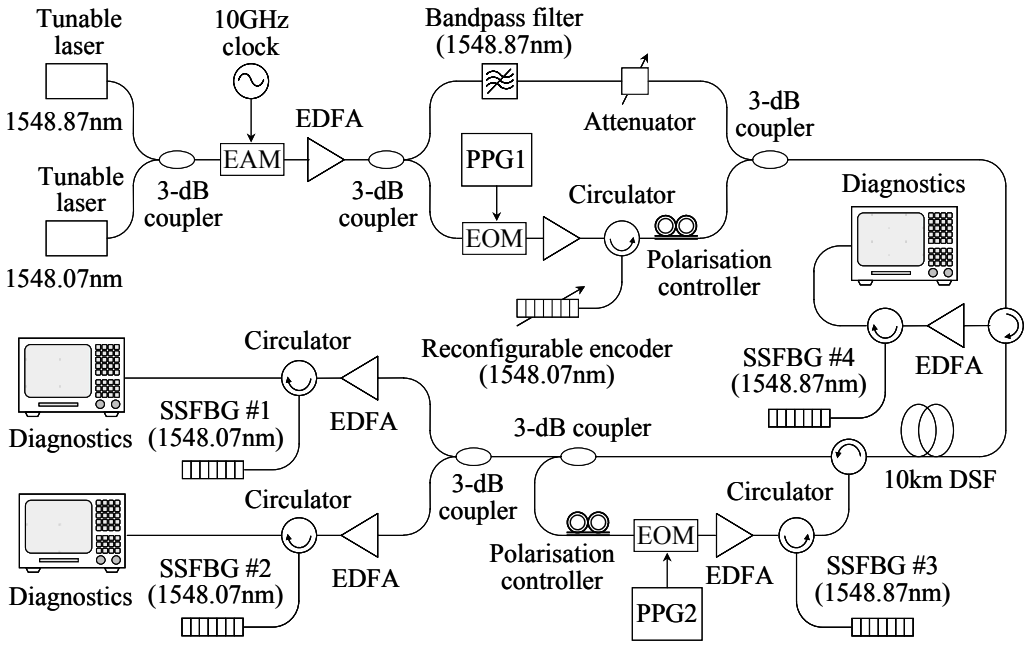

Fig. 3.24. Experimental setup.

Concurrently, the untampered carrier at 1548.87 nm is modulated by another electro-optic modulator in response to the data supplied by a pseudo-random pattern generator (PPG2) and is subsequently encoded by a distinct superstructured grating encoder (SSFBG #3). This wavelength channel is reflected upstream to be recognised only by another superstructured grating decoder operating at the same wavelength (SSFBG #4). The bit-error-rate (BER) performance of the system is monitored at every end terminal. The measured readings are presented in Fig. 3.25.

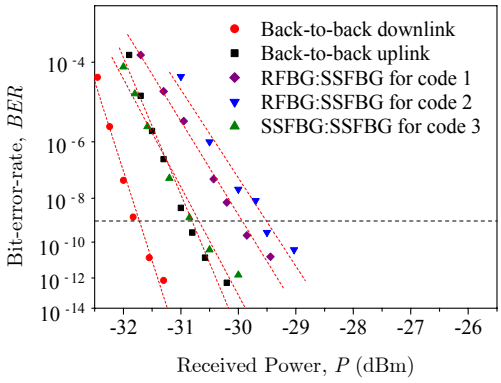

Fig. 3.25. Bit-error-rate measurements at various terminals (SSFBG and RFBG stand for superstructured and reconfigurable fibre Bragg grating respectively).

The results indicate an acceptable quality in terms of data transportations by the proposed device. Only approximately 2.5 dB power penalty is observed for every phase code sequence investigated. This experiment thus confirms the potential of this device to contribute as a main unit of a highly flexible OCDMA system. In another observation, settling time after code switching seems to be an issue. The temperature change induced by the current also changes the surrounding temperature proportionately. This process consumes certain time duration to reach equilibrium since the heat transfer occurs via convection. This is happening in approximately 10 to 30 minutes during the experiment. Nevertheless, the time taken can be substantially reduced by adding a temperature controller element in the configuration.

3.5 Conclusions and Future Directions

We have demonstrated that a uniform fibre Bragg grating can be used in reconfigurable phase-encoding/decoding applications by deploying fine heating elements at equal intervals along the fibre grating. The device has been shown to generate code sequences with bit rates of 20 Gchip/s in bi-polar and quaternary PSK operations. In these experiments, it can satisfactorily reconfigure 4-bit or 16-bit PSK codes in the coherent OCDMA systems. Good auto-/cross-correlation

obtained through match filtering with a phase-encoded superstructured fiber grating indicates very precise dynamic code sequence generation and recognition by the device. BER measurements also show excellent data transportation.

Our results also verify the possibility of channel expansion through exploitation of the continuous phase-shifting capability of our proposed device. Therefore, more phase levels can be experimented. On the other hand, the heating elements are observed to change the surrounding temperature as the code is reconfigured. This problem can be definitely resolved by integrating a thermoelectric module to maintain a constant operating temperature. There is also a possibility to reduce the chip duration and hence increase the chip rate of the code sequences. However, the heating spots may need to be absolutely confined. One possible way to achieved this is by etching the cladding to reduce the fibre diameter so that the wires can be positioned closer to the core, where the grating is actually formed. In conclusion, this device will definitely find important applications in future optical networks as it enables flexible channel management. Possible applications could be header generation/recognition in all-optical packet switched networks as well as coding in advanced OCDMA architectures.

Chapter 4

Bragg Grating Package for Continuous Tuning

4.1 Introduction

Currently, there are numerous applications of fibre Bragg gratings and related devices in both the telecommunications and sensing fields. Their rapid advancements are due to the inherent fibre compatibility and the flexibility they offer for achieving desired spectral characteristics. The latter follows from the discovery of the side writing technique, which permits the realisation of Bragg gratings of any operational wavelength. However, a strong evolution of the optical transmission systems to dynamically reconfigurable networks brings about an additional need for this crucial component to acquire tuning capability.

The Bragg wavelength of a grating can be altered by changing its period or by changing the index of refraction of the waveguide host. These changes typically can be induced either thermally or mechanically. The achievable tuning range is limited by the tolerable extremes of either of these. Change in temperature linearly shifts the Bragg wavelength, with contribution from the thermo-optic effect as well as the thermo-elastic effect. Low temperature sensitivity of the device requires considerably high temperature just to obtain wavelength shifts in a nanometer regime. On the other hand, mechanically induced strain physically extends or compresses the grating period, which leads to a linear shift of the Bragg wavelength in conjunction with the refractive index change in the grating through the strain-optic effect. The excellent tolerance of silica-glass fibres to mechanical strain makes strain tuning preferable for achieving a wide tuning range.

Extensive research into techniques for truly tunable fibre Bragg gratings yielded a variety of strain tuning techniques. Most of them are based on the concept of applying axial strain, either through lateral compression [30,31] or elongation of the grating [32]. The tuning range remarkably has been extended to 45 nm, but these demonstrations typically have required both complicated and bulky components to perform the tuning action. Furthermore, the maximum grating length is usually limited to only a few millimetres so as to avoid bending. Recently, a much simpler tuning technique has been reported by S. Y. Set et. al., based on a beam bending technique [33]. The technique is found to be capable of maintaining all grating parameters over a broad tuning range, as a direct result of the uniform axial strain provided by the bending. Nevertheless, the arc shape of the beam is obtained through a bulky mechanical structure. This research takes the initiative to simplify the structure into a compact package that can also provide the same tuning quality, which will be verified through empirical characterisations.

This chapter explains the mechanics and construction of a novel tuning package. The filtering quality of the package will be fully characterized and analyzed. Eventually, we will demonstrate its applicability in essential optical systems, which include an all-fibre distributed feedback laser (DFB), a high power fibre laser and an optical add/drop multiplexer.

4.2 Bragg Wavelength Tuning through Compression

4.2.1 Elastic Theory of Bending

When bending occurs, the beam is subjected to tensile and compressive stresses simultaneously, where *stress* is defined as force per unit area that the force acts upon. A structural element subjected to tension and compression is elongated and shortened respectively. It follows that there is a line or region of zero stress between the two surfaces, called the neutral axis. The change in length

of a stressed structural element divided by the original length of the unstressed element is defined as *strain.*

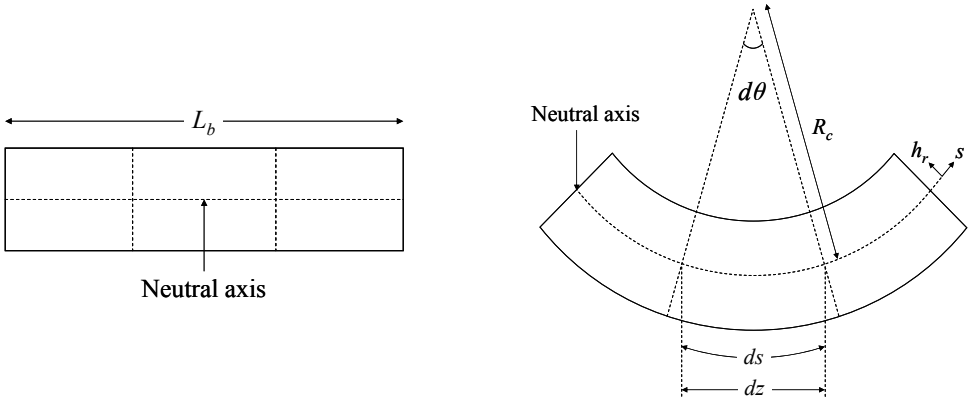

Fig. 4.1. Undeflected beam (left) and beam deformed by pure bending moment (right).

In order to visualise the beam's geometric relationships, the schematic of a bending beam is shown in Fig. 4.1. The dashed lines in the diagram represent two transverse planes of the material and the neutral axis. The planes will remain perpendicular to the neutral axis even after bending. Thus, as the beam bends, developing a curve in the neutral plane that reflects the bending, the tops of these planes become closer together (compression) while the bottom parts experience elongation (tension).

Consideration of a unit segment of a bending neutral plane with length ds, which has a radius of curvature of R_c, and forms a sector angle $d\theta$, indicates that

$$ds = R_c \cdot d\theta \tag{4.1}$$

A segmental plane at some distance h_r, from the neutral plane will then stretch/shorten to

$$ds_h = \left(R_c \pm h_r\right) \cdot d\theta \tag{4.2}$$

Therefore, the longitudinal strain in the plane is

$$\begin{aligned}\varepsilon_z &= \frac{ds_h - ds}{ds} \\ &= \frac{\left(R_c \pm h_r\right)\cdot d\theta - R_c \cdot d\theta}{R_c \cdot d\theta} \\ &= \pm\frac{h_r}{R_c}\end{aligned} \tag{4.3}$$

where positive and negative signs indicate tensile and compressive strain, respectively. A material behaves elastically when it returns to its original shape when an applied load is removed. The stress point where the material stops behaving elastically is called the yield stress σ_{yield}. This point is found by plotting stress versus strain and determining the stress at which the plot becomes non-linear. The slope of the stress-strain curve in the elastic region is defined as the material modulus of elasticity (or *Young's modulus*), denoted by E. The stress-strain relationship that is applicable for linear-elastic bending is given by

$$\varepsilon_z = \frac{\sigma_z}{E} \tag{4.4}$$

where σ_z is the stress, which is given by

$$\sigma_z = \frac{dF_z}{dA} \tag{4.5}$$

where A is the total cross-sectional area and F_z is the longitudinal force acting on the cross section. Combining Equation (4.3) and Equation (4.4) will then give

$$\sigma_z = \pm\frac{E}{R_c}h_r \tag{4.6}$$

Typically, a beam of regular shape that is made up of a homogeneous material has its neutral axis at half the height. On the other hand, the *effective* neutral axis of a composite beam (beam made of two or more different materials) will be at a different location, symbolized by $\overline{H}$ (Fig. 4.2).

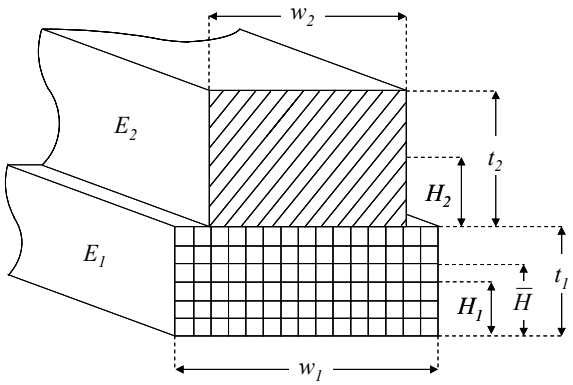

Fig. 4.2. Beam made of two materials with a different modulus of elasticity.

In order to determine this location, the equilibrium condition of the forces imposed on transverse planes of each material is used, which states that

$$\sum F_z = \sum_i \left(\int_{A_i} \sigma_z \, dA_i \right) = 0 \tag{4.7}$$

where F_z is the component of forces acting on the element of area dA_i. Young's modulus for the material is assumed to be the same in tension and compression. Substituting Equation (4.6) in this equation leads to

$$\begin{aligned} \sum_i \left(\int_{A_i} \frac{E_i h_{ri}}{R_c} \, dA_i \right) &= 0 \\ \sum_i \left(h_{ri} E_i A_i \right) &= 0 \end{aligned} \tag{4.8}$$

Moving the reference axis to the bottom of the beam cross section makes $h_{ri} = H_i - \overline{H}$ and allows the above equation to be rewritten as

$$\begin{aligned} &\sum_i \left(\left(H_i - \overline{H} \right) E_i A_i \right) = 0 \\ &\Rightarrow \overline{H} = \frac{\sum_i \left(H_i E_i A_i \right)}{\sum_i E_i A_i} \end{aligned} \tag{4.9}$$

where H_i represents the reference coordinate for the centroid of an individual material. The distance $\overline{H}$, is given with reference to the bottom of the beam cross section.

It follows that the actual location $\overline{H}$, depends on the Young's modulus of the individual materials and also the dimensions of their cross section, as below,

$$\overline{H} = \frac{\frac{t_1^{\,2}}{2} E_1 w_1 + \frac{t_2^{\,2}}{2} E_2 w_2 + t_1 t_2 E_2 w_2}{t_1 E_1 w_1 + t_2 E_2 w_2} \tag{4.10}$$

where t_i and w_i are the heights and widths of the materials, respectively.

Another mechanical behaviour that arises from bending is the *Poisson effect*. The Poisson effect describes the tendency of the material to preserve its volume when changing length. Poisson's ratio ν, is the ratio of the transverse contraction strain to the longitudinal extension strain in the direction of stretching force. Tensile deformation is considered to be positive and compressive deformation is considered to be negative. The definition of Poisson's ratio contains a minus sign so that normal materials have a positive ratio.

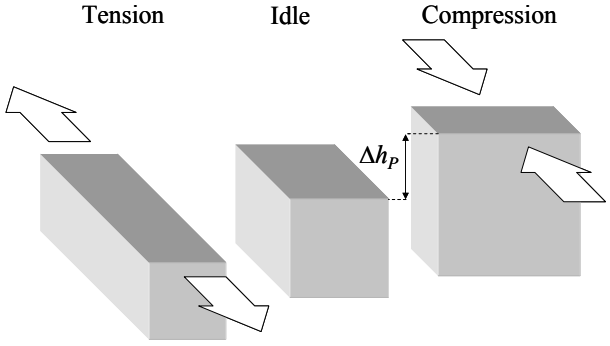

Fig. 4.3. The Poisson effect showing the direction of applied forces and the resulting geometric deformations.

In bending, the Poisson effect is insignificant when only a homogeneous material is considered. This is because the simultaneous shortening and

elongation would have cancelled the effect. On the other hand, since the neutral axis of composite beams is most likely to be in the material of higher Young's modulus, those with lower values will definitely experience this effect. Therefore, in this case, the Poisson effect can be taken into account in order to obtain a slightly more accurate analysis.

4.2.2 Device Descriptions

Silica is found to be better at resisting compression than tension. Therefore, compression can be coarsely imposed onto a fibre grating to alter its characteristics in accordance with Equation (4.12). According to [33, 87], uniform compression of a fibre grating can be achieved by bending the grating in an arc with a constant radius, with the fibre axis slightly displaced at a distance h, from the neutral axis of the bending beam of length L_b, onto which it is firmly adhered. The relative compression/extension of the fibre grating is then given by

$$\varepsilon = -\frac{h\theta}{L_b}, \; L_b \neq 0 \tag{4.11}$$

where θ is the central angle of the sector formed by the arc. It follows that the Bragg wavelength shift obeys the following rule:

$$\Delta\lambda \approx (1 - p_e)\,\varepsilon\lambda_B \tag{4.12}$$

where λ_B is the Bragg wavelength of the fibre grating in an idle state and $p_e \approx 0.22$ is the photo-elastic coefficient.

The schematic structure of our tunable package based on compression is illustrated in Fig. 4.4. The fibre Bragg grating is embedded in a flexible material, which is firmly fixed onto a straight elastic beam of length L_b. The flexible slab also acts to hold the grating firmly so that it will not slip from its axis, thus avoiding premature cracks, which commonly occur for brittle materials under compression. The flexible slab is made of plastic with sufficient hardness to resist indentation caused by a moderate load. The modulus of elasticity E, of the

plastic is roughly 50 times less than that of the elastic steel beam. The two materials are bonded together using strong adhesive solution.

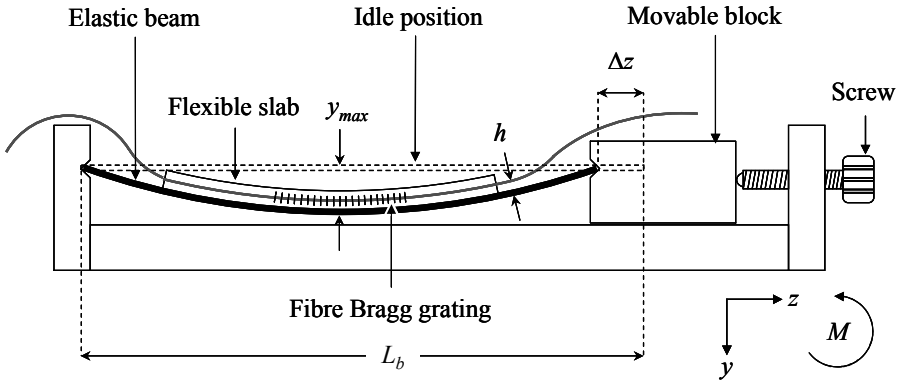

Fig. 4.4. Schematic structure of the tunable package.

When the beam is subjected to a horizontal inwards force, it will be deformed into a curved shape. This shape takes a sinusoidal form and may be deduced by solving the differential equation of the deflection curve [88] as follows,

$$\frac{d^2y}{dz^2} = -\frac{M}{EI} \tag{4.13}$$

where M is the externally applied bending moment, E is the Young's Modulus and I is the second moment of area. The y-axis and z-axis lie on the plane of the paper and their positive directions are as shown in Fig. 4.4. The bending moment M, takes a positive value for anti-clockwise direction. The derivation of the above equation is shown in Chapter 5. Considering the moment equilibrium about the x-axis which is perpendicular to the y and z-axis gives,

$$M = F \times y \tag{4.14}$$

where F is the external force acting horizontally. By inserting this exact bending moment back into Equation (4.13), it will give a general solution in the form of [89]

$$y(z) = C_0 \cos\left(\sqrt{\frac{F}{EI}}z\right) + C_1 \sin\left(\sqrt{\frac{F}{EI}}z\right) \tag{4.15}$$

where C_0 and C_1 are arbitrary constants. The boundary conditions are that $y = 0$ at $z = 0$ and $z = L_b - \Delta z$, where Δz is the horizontal displacement of one end of the beam from its idle state. Therefore, $C_0 = 0$ and

$$\sqrt{\frac{F}{EI}} = \frac{\pi}{L_b - \Delta z} \tag{4.16}$$

If $y = y_{max}$ at $z = \dfrac{L_b - \Delta z}{2}$ from symmetry, then $C_1 = y_{max}$ and the deflection curve is given by

$$y(z) = y_{max} \times \sin\left(\frac{\pi z}{L_b - \Delta z}\right) \tag{4.17}$$

where $y_{\max}$ is the amplitude of the beam deflection. An example of the correlation between these two parameters is illustrated in Fig. 4.5. A unique value of $y_{\max}$ for a given horizontal displacement, can be calculated by satisfying the condition that the length of curvature of the bending beam must always remain exactly equal to L_b.

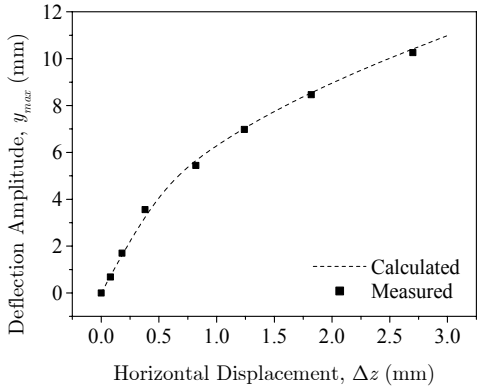

Fig. 4.5. Deflection amplitude of a 100 mm beam as a function of horizontal displacement of the bending force.

The local stress ε, at different locations in the bent fibre can be obtained by dividing it into narrow subsections. Each subsection can be approximated as an arc of a circle since the radius is very large compared to its size and therefore Equation (4.11) applies. The sector angle $d\theta_i$, relating to each arc can be calculated by using the following formula,

$$d\theta_i \approx \arctan\left(\frac{d}{dz}y(z_i)\right) - \arctan\left(\frac{d}{dz}y(z_i + dz_i)\right) \tag{4.18}$$

where dz is the lateral width of the arc (Fig. 4.1). Whereas, the arc length ds_i, is given by

$$ds_i \approx \int_{z_i}^{z_i+dz_i} \sqrt{1+\left(\frac{d}{dz}y(z)\right)^2}\,dz \tag{4.19}$$

Subsequently, the overall Bragg wavelength shift for a given horizontal translation Δz, is obtained by substituting these values into Equation (4.11) and Equation (4.12).

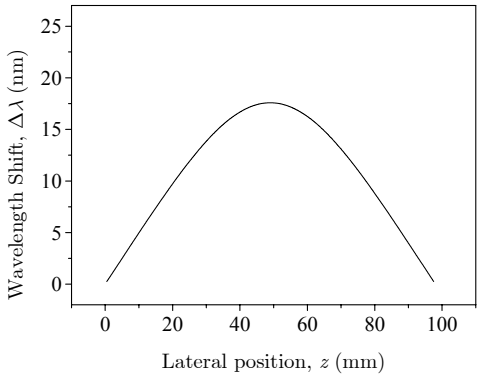

Fig. 4.6. Calculated wavelength shift versus lateral position of gratings on a 100 mm beam with $h \approx 1.6$ mm and $\Delta z = 2$ mm.

Fig. 4.6 shows the calculated Bragg wavelength shift of gratings at various locations on a 100 mm beam due to a 2 mm horizontal translation and an off neutral axis displacement of about 1.6 mm. Using the above analysis, the operational wavelength of a fibre grating mounted in the centre of a bending beam can be accurately determined for a given displacement.

The Poisson effect can also be considered by incorporating the resulting additional thickness Δh_P, (Fig. 4.3) into the total off neutral axis displacement, which is given by

$$\Delta h_P = \nu \cdot t_0 \cdot \frac{\overline{h} \cdot \theta}{ds} \tag{4.20}$$

where ν is the Poisson's ratio, t_0 is the initial thickness and $\overline{h}$ is the mean distance from the neutral axis.

4.3 Device Characteristics

4.3.1 Spectral Quality under Bending Stress

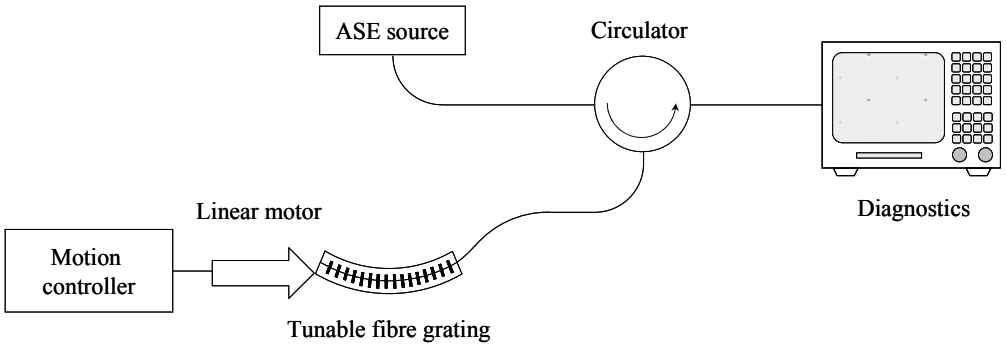

Fig. 4.7. Experimental setup.

The correlation between the horizontal displacement of one end of the beam from its idle position and the Bragg wavelength shift was experimentally

confirmed by varying these parameters in a simple configuration shown in Fig. 4.7. During the tuning procedure, the operating wavelength of a well-packaged fibre Bragg grating (as described above) was swept across the entire conventional band (C-band). A linear motor connected to a motion controller gave quantifiable horizontal displacements. The output power and spectral response of the reflected light that was originated from a broadband ASE source were monitored and recorded on an optical spectrum analyser with a resolution of 0.01 nm.

The demonstration initially took into consideration gratings located approximately 1.72 mm and 2.18 mm away from the neutral axis of a 100 mm beam and also those displaced by approximately 2.17 mm and 2.66 mm on a 150 mm beam. The fibre Bragg gratings used were of various lengths L_g, which were 10 mm and 20 mm. The measured wavelength responses are plotted, with their corresponding theoretical curves, in Fig. 4.8. The results positively verify that these parameters comply with the aforementioned relationships.

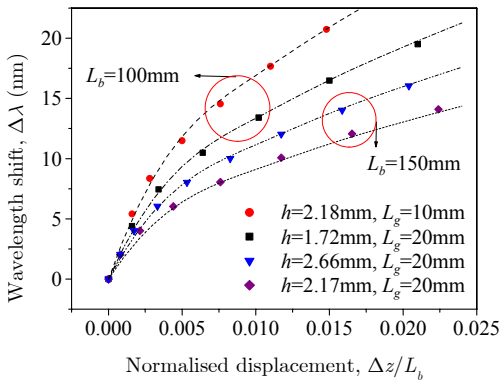

Fig. 4.8. Overlay of the measured wavelength shifts (symbols) and their corresponding theoretical curves for different values of h on 100 mm and 150 mm beams.

The uniformity of the compression was also investigated in this study. Fig. 4.9 shows an excellent match between the spectra of a 5 mm fibre Bragg grating

in its idle and compressed states, indicating that no chirp was induced upon bending. It is therefore confirmed that the compression was uniform.

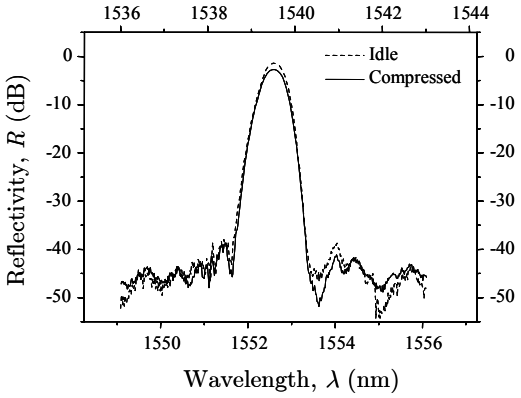

Fig. 4.9. Spectral response of a 5 mm fibre Bragg grating in idle and compressed states (dashed line: bottom axis, solid line: upper axis).

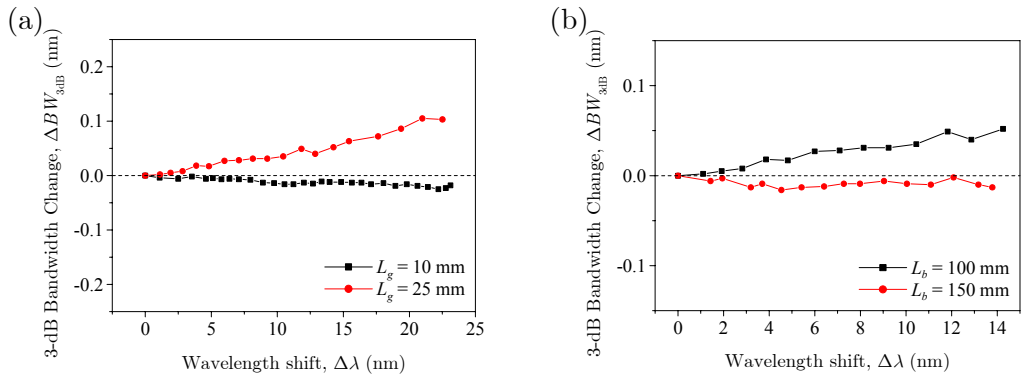

Fig. 4.10. 3-dB bandwidth change at various states of compression for (a) L_b = 100 mm and $h \approx 1.7$ mm, and (b) L_g = 25 mm and $h \approx 1.7$ mm.

Equally uniform compression is also possible for longer fibre gratings as devices with length of up to 25 mm were shown to exhibit excellent consistency in their 3-dB bandwidth. Results from the 25 mm grating are shown in Fig. 4.10(a), measured from its initial value of about 0.17 nm. Any variation in these

values can be reduced by increasing the length of the bending beam as implied by Fig. 4.10(b).

On the other hand, this study has also verified that the bending produced by the tunable package was not of constant radius by characterising gratings positioned at some distances away from the centre of the beam. The results in Fig. 4.11 show that the gratings were substantially chirped as the compressive strain increased at those locations. Therefore, this confirms that the bending followed the sinusoidal shape as presumed in the theoretical analysis.

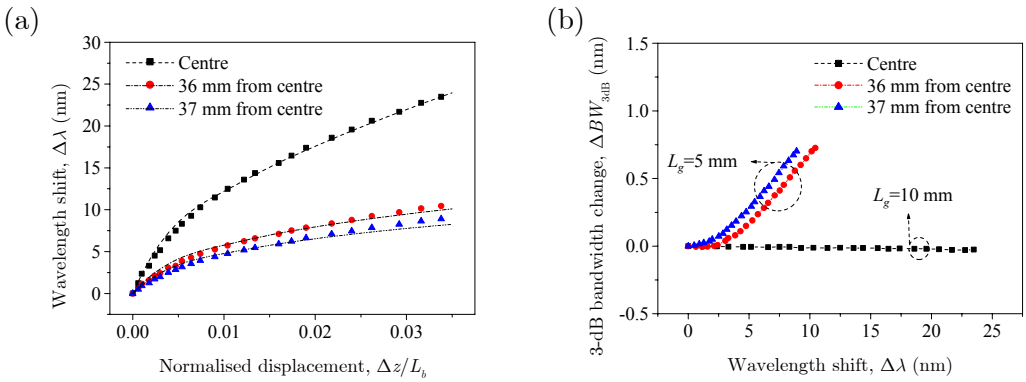

Fig. 4.11. Responses of gratings at different locations on the beam with $h \approx 1.7$ mm. (a) Wavelength shift against the normalised horizontal translation (symbols: measured, lines: calculated), and (b) 3-dB bandwidth change at various states of compression.

The later experiments expanded the tuning window to encompass the long band (L-band). This was in response to the emerging requirement for a wavelength-selective filter with a large tuning range for application in the expanded DWDM systems. These systems utilise all the short band (S-band), conventional band (C-band) and long band (L-band) in order to increase the capacity of optical networks. For this objective, a relatively large off-neutral axis displacement h , is required to achieve large tuning for small horizontal translation, as indicated by the theoretical curves in Fig. 4.12. A bending beam of 100 mm length was chosen to hold a flexible slab that gives the required h

(~5.95 mm). The grating length was 3 mm, which was carefully selected to ensure that it would remain unchirped after a large horizontal translation. The Bragg wavelength of the grating was 1614.3 nm and it was also apodised with a Blackman profile [90].

The excursion of the measured peak wavelength of the tunable device as the compression increased is also shown in Fig. 4.12. It continuously traversed the entire L-band, crossed the dead band, and finally reached halfway across the C-band, which amounted to a wavelength range of 70 nm. This point corresponds to 5.56% of compression imparted on the grating, which is still far below the maximum tolerable strength of the silica fibre in a compression mode (approximately 23%) [30, 91]. Therefore, it should be possible to compress further down in wavelength to cover the whole C-band.

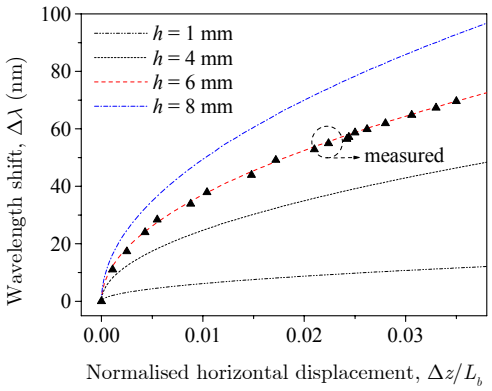

Fig. 4.12. Wavelength shift against the normalised horizontal translation of the tunable device.

The uniformity of the compression was maintained throughout its operation range as confirmed by the 3-dB bandwidth measurements plotted in Fig. 4.13. Also shown are the reflection spectra of the device at various compression states.

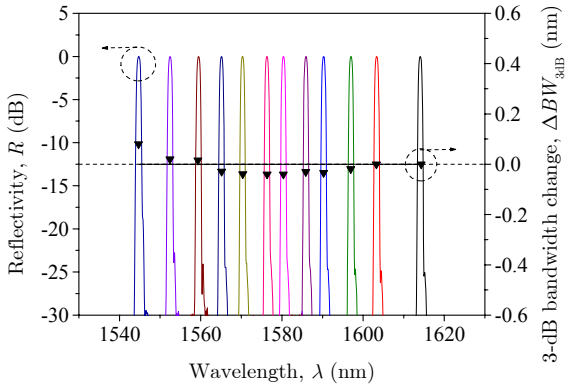

Fig. 4.13. 70 nm tuning range and 3 dB bandwidth change of the tunable device.

Additionally, the device exhibited no noticeable spectral deformation when back in the idle state, even after repeated tuning. This reversible behaviour can only remain as long as the beam is linearly elastic. Therefore, it is necessary to constrain the inward horizontal displacement to be below the proportionality limit of the beam. Consequently, this requirement puts a limit to the achievable tuning range, yet this limit is way beyond the erbium band. Thermal performance of the compressor was also monitored during the experiment. An anticipated increase in the temperature sensitivity was observed, which arose from the fact that the material embedding the fibre grating was firmly adhered to the beam. As a result, the overall thermal expansion coefficient of the arc structure practically took the value of that of the beam (approximately 9×10^{-6} /°C). Therefore, the expected sensitivity for the Bragg wavelength would be approximately equal to 23 pm/°C. Nevertheless, this variation can be minimised through astute choice of the materials for the beam and the mount.

4.3.2 Differential Group Delay and Polarisation Dependent Loss Measurements

Polarisation mode dispersion (PMD) can limit fibre optic transmission performance. Stress may induce additional birefringence in an optical fibre

medium, which in turn causes polarisation components of a signal to travel at different group velocities. The relative delay between two orthogonal polarisation modes is called differential group delay (DGD). As data rates increase, the impact of PMD increases. In this circumstance, polarisation mode delay represents a greater portion of a bit period of a digital optical pulse. High data rate signals may then suffer increased jitter and degraded bit error rate (BER). To maintain data transmission integrity, it is important to keep overall DGD within 10 to 20% of the bit period of a signal. DWDM technology increases the number of optical elements in the signal path. Higher data rates require that PMD must be analysed in these components, and due to the narrowband nature of DWDM, PMD must be measured over small wavelength ranges. Characterising PMD on each channel of the components ensures that the overall system can be designed and manufactured to perform well in fibre optic networks.

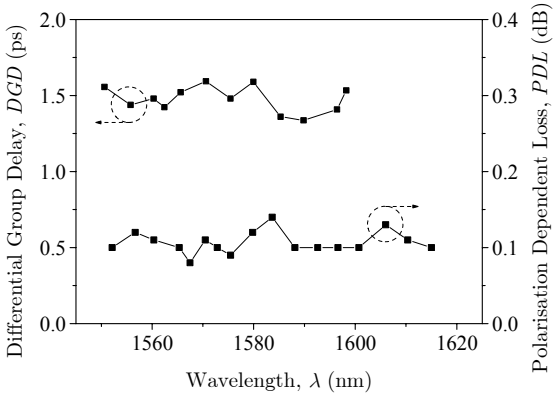

Fig. 4.14. Differential group delay (DGD) and polarisation dependent loss (PDL) of the tunable device at various bend positions.

The PMD test on gratings mounted on the proposed package was done by using a simple setup. A narrowband laser source fed continuously polarised light onto the grating under test through an automated polarisation analyser (HP 8509B). The grating was probed over its entire 3-dB bandwidth. The reflected light returned into the analyser, which then computed the average DGD. Results

obtained for various degrees of bending are shown in Fig. 4.14, which shows that the DGD was always less than 1.6 ps with only small variations. In addition, the polarisation dependent loss (PDL) of the device was also characterised, and no appreciable increment in the parameter was observed. All values were well within 0.11 ± 0.03 dB. Therefore, these measurements verify that the tuning package does not cause any additional significant birefringence.

4.3.3 Insertion Loss under Large Compressive Stress

Since the fibre can withstand high compressive stress, we have attempted to further widen the tuning range. Using $h \approx 6$ mm and a 100 mm beam, we managed to obtain a 110 nm tuning range from a 3 mm fibre Bragg grating which was written on a deuterium-loaded fibre with $NA \approx 0.13$ and $\lambda_c \approx 1200$ nm. The grating was initially centred at 1613.16 nm, with an effective refractive index change $\eta \cdot \Delta n$, of roughly 8×10^{-4} and a 3-dB bandwidth BW_{3dB}, of about 0.82 nm. This result in fact represented the widest tuning range ever achieved with a silica-based fibre Bragg grating.

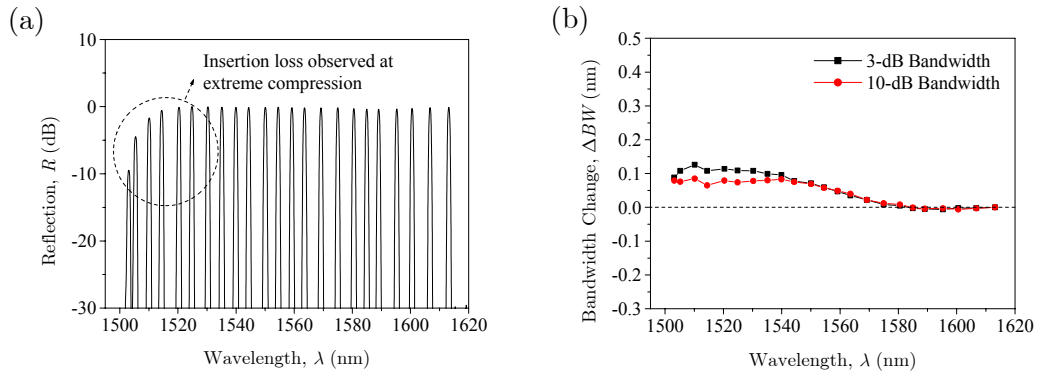

Fig. 4.15. (a) Reflection spectra at various operational wavelengths and (b) the corresponding 3-dB and 10-dB bandwidths.

The spectra of the device recorded at various operational wavelengths are shown in Fig. 4.15(a). The figure revealed a significant insertion-loss at intense negative stress (compression), as marked by the circle. This unexpected observation has subsequently triggered an investigation on the contributing factors, which may later facilitate full exploitation of low-loss compression-tunable devices.

The investigations were carried out by monitoring several different fibres, which were embedded in close proximity to each other inside the composite beam structure to maintain exactly similar ambient conditions for all magnitudes of stress. We started our investigations by comparing the losses induced at the associated Bragg wavelengths, in a standard single-mode-fibre (SMF) with a numerical aperture (NA) of about 0.13 and cut-off wavelength λ_c, of around 1200 nm (fibre A), to that in a photosensitive fibre. The photosensitive fibre was a boron-codoped germano-silicate (B/Ge/Si) fibre with $NA \approx 0.14$ and $\lambda_c = 1194$ nm (fibre B), hence having a nominally identical transverse refractive index profile to fibre A. The results of these fibres are summarised in Fig. 4.16(a) and demonstrate massive differences in the induced losses under extreme values of the stress.

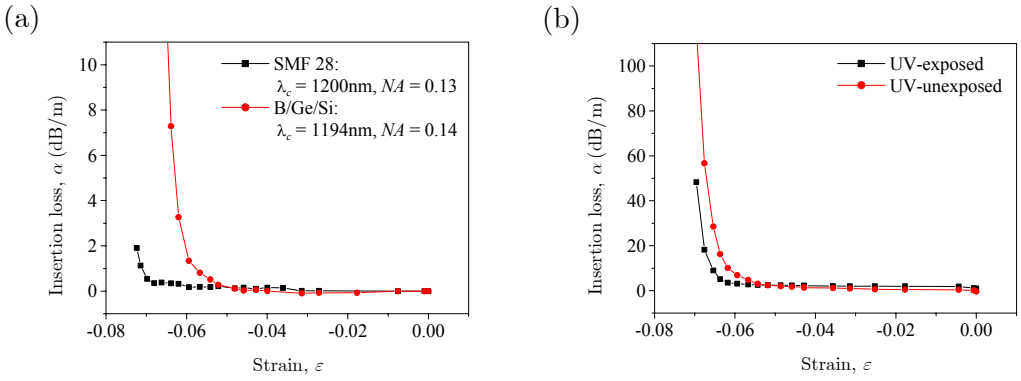

Fig. 4.16. (a) Stress-induced loss at the associated Bragg wavelength against strain for a B/Ge/Si-fibre and a standard single-mode Ge/Si-fibre (SMF-28) of $\lambda_c \approx 1200\,nm$ and $NA \approx 0.13$. (b) Stress-induced insertion loss against strain for an exposed and un-exposed B/Ge/Si fibre.

For strain levels up to about 6%, corresponding to approximately 70 to 75 nm of wavelength tuning, no losses were introduced in either fibre. However, beyond this strain level, the B/Ge/Si fibre was seen to have a sharp increase in loss with a value exceeding 1 dB/m. In contrast, the SMF barely exhibited any loss increase for strain levels up to approximately 7%, suggesting that the inclusion of boron in the fibres had an effect on the induced loss.

In addition, we investigated the effect of UV-exposure on fibre B in relation to the stress-induced losses. In this case we used an estimated fluence of 1 kJ/cm^2 resulting in an index increase of about 4×10^{-4}. The results showed that exposure to UV light reduced the threshold for induced loss of 10 dB/m from around 6.2% to 6.7% (Fig. 4.16(b)). Note that the exposure to UV light and inclusion of boron are in fact closely related to photosensitivity. Therefore, Fig. 4.16(a) and Fig. 4.16(b) directly suggest that photosensitivity plays an important role in the occurrence of the insertion loss.

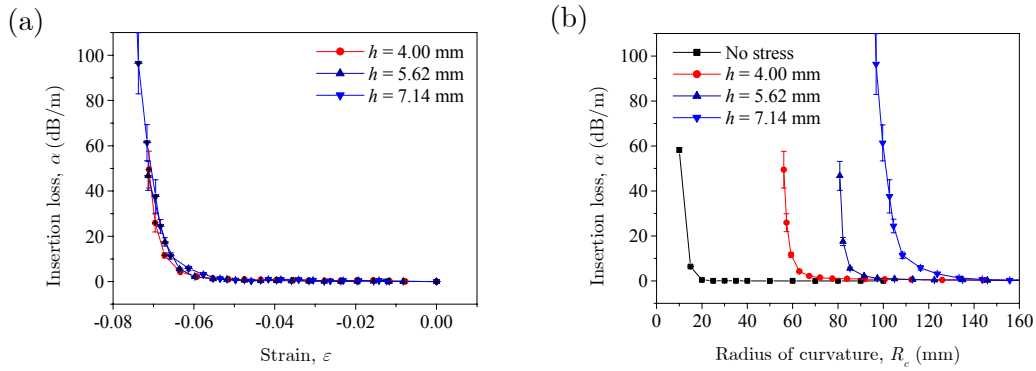

Fig. 4.17. (a) Insertion loss against stress and (b) insertion loss against radius of curvature for various off-neutral axis displacements.

In order to dismiss the notion that *bending loss* may have an influence, we took measurements on the insertion loss in fibre B for various values of the displacement from the neutral axis. The data collected are plotted in Fig. 4.17(a), which shows that massive insertion losses began exactly at the same magnitude of

strain. These points however corresponded to a different radius of curvature for each beam, as depicted by Fig. 4.17(b). Therefore, the occurrence of the massive insertion losses was independent of the radius of curvature. Furthermore, the threshold points occurred at relatively large radii with respect to that observed in the same fibre without the presence of stress. Conclusively, the insertion losses were in fact induced by the large magnitudes of stress, whereas bending losses were merely negligible. In addition, the effect of micro-bending can only be claimed to be responsible if fibres with an identical field overlap factor have the same strain points where the effect starts, irrespective of any difference in the composition of the fibres. However, Fig. 4.16(a) shows contrary experimental results, wherein the two types of fibres exhibit different reactions to large stress levels.

The plot of the corresponding 3-dB and 10-dB bandwidths of the compressed fibre Bragg grating is shown in Fig. 4.15(b). It shows that these parameters gradually increased with increasing stress level, yet this was not because the grating was chirped. This fact can be appreciated by examining the transmission spectra of a fibre Bragg grating under various levels of stress. Measurements were obtained from a 3 mm grating, inscribed on a Boron-codoped germanosilicate fibre with a cut-off wavelength of 925 nm and an *NA* of 0.15. The recorded spectra are illustrated in Fig. 4.18(a), while the associated transmission losses are plotted against the applied strains in Fig. 4.18(b).

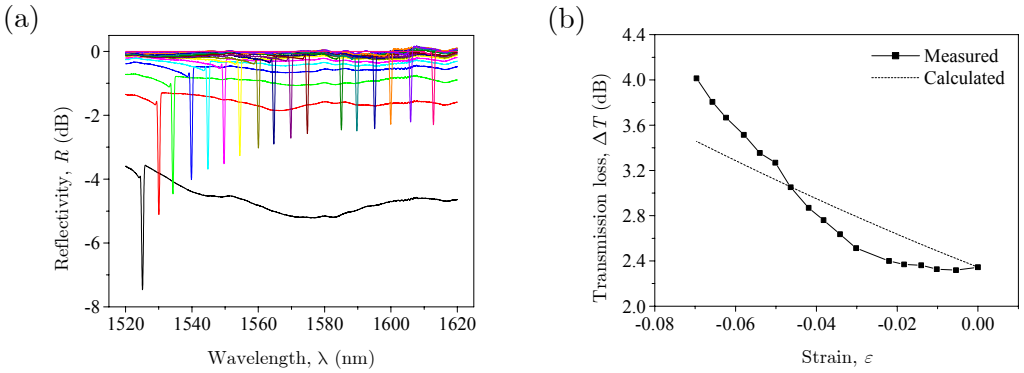

Fig. 4.18. (a) Transmission spectra at various operational wavelengths and (b) the corresponding transmission loss with its theoretical curve.

Fig. 4.18(b) indicates that the Bragg grating was getting stronger (increasing transmission loss or reflectivity at the Bragg wavelength) as it was compressed. This was expected since the normalized frequency V, was increased and thus also the value of the field overlap factor η. The increment was a consequence of the shift of the operating wavelength λ, towards the cut-off wavelength λ_c, as well as the fact that the core size was increasing radially due to the *Poisson* effect. Moreover, in the presence of stress, the resultant value of the refractive index n', is proportional to its initial value n [43], which is mathematically expressed as,

$$n' = (1 - p_e\varepsilon) \cdot n \tag{4.21}$$

where p_e is the photo-elastic coefficient. On this account, the elasto-optic effect will cause different amount of changes in the refractive index of the core and cladding for the same magnitude of strain ε, thus increasing the NA. Taking all of these effects implicitly into account, the value of V should change according to the following rule,

$$V = \frac{2\pi}{\lambda} \cdot (1 - \nu_f\varepsilon) a_0 \cdot (1 - p_e\varepsilon) NA \tag{4.22}$$

where a_0 is the initial radius of the fibre core, p_e is the photo-elastic coefficient and ν_f is the Poisson's ratio of silica. In addition, Equation (4.21) suggests that the refractive index modulation should also change, as the grating planes with a lower refractive index vary more slowly compared to the planes with a higher refractive index. Therefore, the anticipated transmission loss ΔT, is given by,

$$\Delta T = -10 \cdot \log\left(1 - \tanh^2\left(\frac{\pi}{\lambda_B} \cdot \eta(V) \cdot (1 - p_e\varepsilon) \Delta n \cdot L_g\right)\right) \tag{4.23}$$

where $\eta(V)$ is the modified field overlap factor due to a change in the V-number in accordance with Equation (4.22), Δn is the initial refractive index change, λ_B is the centre wavelength, and L_g is the grating's length. The evolution of the calculated transmission loss was then plotted on the same graph. We can however see that it did not match well with the measurement values, which suggests that

the increase in the grating strength may also have a contribution from some unexplained factors. It can be concluded that regions with different refractive indices react differently with large stress and these reactions are unpredictable. This observation also suggests that the properties of the fibre, which in this case, the quantity of defects associated with photosensitivity, may as well influence the magnitude of the insertion loss to large stress.

4.4 Demonstrations of Device Application

4.4.1 All-fibre Distributed Feedback Laser

The proposed package has been shown to be capable of imposing constant stress on an embedded fibre Bragg grating. Therefore, it may also be possible to tune a distributed feedback (DFB) fibre laser. Since the beam portion with constant stress is rather limited (see section 4.3.1), a longer beam is necessary to accommodate a typical length of DFB fibre laser. We demonstrated a tunable DFB fibre laser with a tuning range of nearly 25 nm [92]. The experiment was carried out in collaboration with Dr. Li Bin Fu (research fellow). It was constructed using an asymmetrical $\pi/2$-phase shifted fibre grating [93] with a length of 25 mm, embedded on a 290 mm composite beam. The DFB assembly was displaced vertically from the neutral axis of the beam by roughly 7 mm. The DFB fibre laser was constantly pumped at 63 mW. A laser diode at 977 nm wavelength was used as the pump source, which was coupled via a 980/1550 nm-WDM coupler. An optical isolator was spliced at both ends of the grating in order to eliminate the back reflections.

Its spectral responses were recorded during the tuning operation by an optical spectrum analyzer having a resolution of 0.2 nm. The results are presented in Fig. 4.19(a), which displays a successful tuning operation from 1553.3 nm to 1528.85 nm. Only approximately 1.3 dB power fluctuation was observed for wavelengths down to 1534 nm. Below this point, where it was still far below the stress-induced loss event, the DFB exhibited a rapid power drop. Therefore, the power drop was purely in accordance with the gain roll-off of the erbium-doped medium.

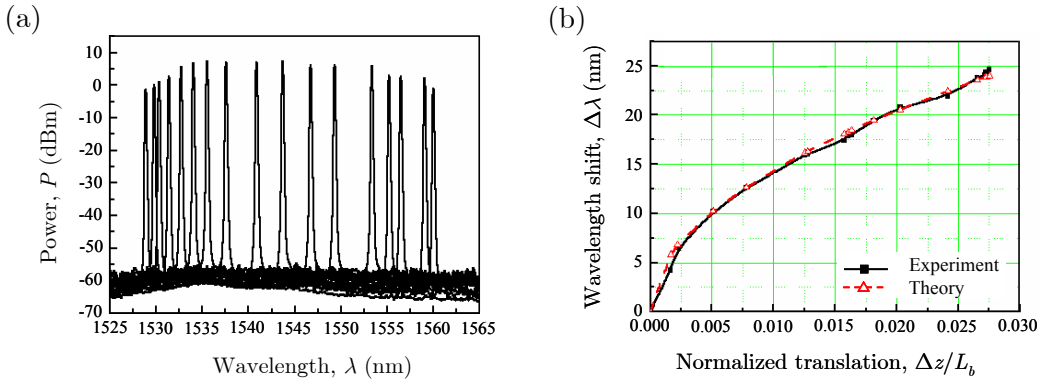

Fig. 4.19. (a) Laser output spectra at various operational wavelengths and (b) the central wavelength shift as a function of normalized horizontal translation.

The laser line-width was also measured utilising the delayed self-heterodyne detection technique. The laser signal was first split by a fibre coupler. Light in one arm was modulated by an acousto-optic modulator (AOM) at roughly 35 MHz, while light in the other arm was delayed using SMF of approximately 58 km. Subsequently, the outputs from both arms were mixed and detected by a photo-detector and an RF spectrum analyzer. The line-width remained at around 92 kHz for the full tuning range. Single mode operation was also maintained with a side mode extinction ratio larger than 55 dB. Additionally, the central wavelength was able to be shifted upward to about 1560 nm by operating the package in tension mode. The measured central wavelength excursion with the horizontal translation of the bending beam in compression mode is shown in Fig. 4.19(b). Excellent agreement with the calculated values confirms that the operational wavelength of the laser can be set with high precision.

4.4.2 Resonator Mirror for High Power Fibre Laser

Fibre lasers have been developing rapidly in recent years, especially those operating at wavelengths between 1.5 and 2 μm which are motivated by many emerging interests for free-space and satellite applications. Some demonstrations

have also utilized external lens-coupled diffraction grating into the fibre laser systems in order to achieve tunability. However, this configuration led to a bulky device.

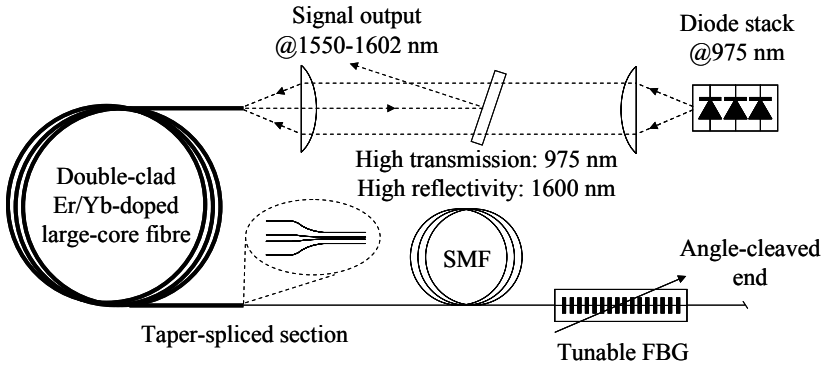

Fig. 4.20. Cladding-pumped tunable Er-Yb doped fibre laser arrangement.

Working in collaboration with Dr. J. K. Sahu (research fellow) and Dr. Y. Jeong (research fellow), we constructed an efficient tunable narrow linewidth high power erbium (Er): ytterbium (Yb) co-doped fibre laser (EYDFL) [94]. The EYDFL comprised a double-clad fibre with a 25 μm diameter phosphosilicate core, embedded in a 400 μm diameter pure silica inner cladding that provided a core *NA* of 0.22. The inner cladding had a 'D' shape and was coated with a low refractive index polymer, thus having a nominal *NA* of 0.49. Pump light from a diode stack, operating at 975 nm, was coupled into the inner cladding through a simple lens arrangement. The laser cavity was formed between a perpendicularly cleaved fibre facet at the pump launch end and a high reflectivity fibre Bragg grating at the other end. The Bragg grating was written in a standard single-mode fibre (SMF). Fusion splicing of the gain medium with the FBG was made possible after tapering one of its ends to match the outer diameter of the SMF. The laser output was collected at the pump launch end using a dichroic mirror with a high reflectivity around 1.6 μm . The complete arrangement of the fibre laser system can be seen in Fig. 4.20.

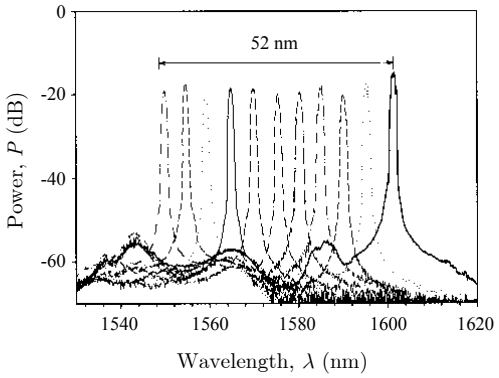

Fig. 4.21. Laser output spectra at different operational wavelengths.

The tunable FBG device enabled tuning of the fibre laser system from 1602 down to 1550 nm. The spectra of the laser output at various wavelengths are shown in Fig. 4.21. The linewidth stayed constant at roughly 0.2 nm for the full tuning range. The maximum output power of 70 W at 1560 nm was obtained from 240 W of launched pump power. The pump absorption in the Er-Yb doped fibre (EYDF) was sufficiently high (∼2.5 dB/m) to minimize the risk of damaging the SMF. Moreover, the SMF had a higher refractive index coating than that of the pure-silica inner cladding of the EYDF, in which the pump laser was guided. Consequently, any residual pump power that reached the SMF will leak into the coating of the SMF and be absorbed. The unabsorbed pump power was measured to be only a few watts.

4.4.3 Add/Drop filter for All Optical TDM to WDM System

Conversion of optical time-division multiplexed (TDM) signals into wavelength-division multiplexed (WDM) signals has become an attractive solution for effective signal processing. This is attributed to the availability of filters with definite phase and amplitude responses in the wavelength domain,

such as fibre Bragg grating filters. Recently, we successfully demonstrated the use of the fibre Bragg grating technology as a wavelength filter in an all-optical time-division multiplexer [95] for a 40 GHz optical TDM system. This demonstration was carried out in collaboration with Mr. Paolo J. Almeida (research student).

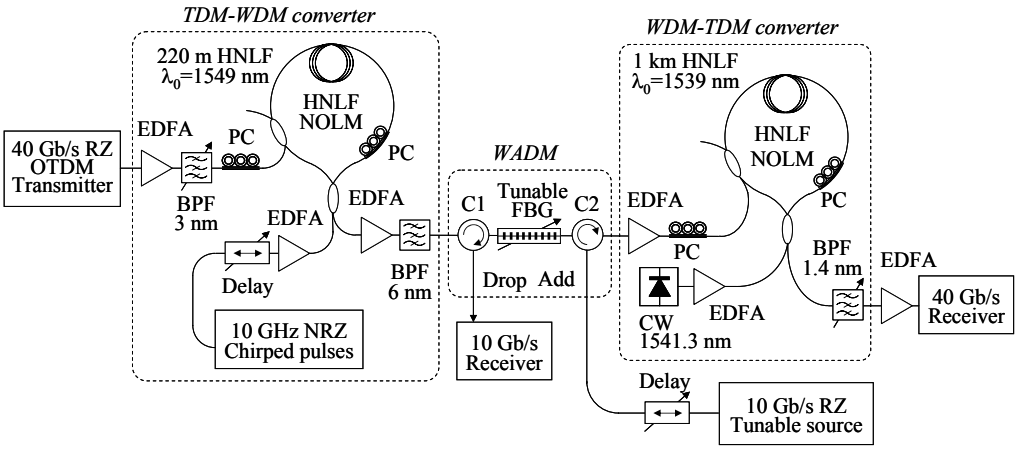

Fig. 4.22. Experimental setup for OTDM add/drop multiplexing of a 40 Gb/s signal. (HNLF: highly nonlinear fibre, PC: polarization controller, BPF: band-pass filter, EDFA: erbium-doped fibre amplifier).

The experimental setup for the optical TDM add/drop multiplexing of a 40 Gb/s signal is shown in Fig. 4.22. The optical TDM signal was initially mapped onto lower bit rate WDM signals through a highly non-linear optical loop mirror (NOLM). After amplification, the original TDM signal with a central wavelength of 1547 nm, acted as the control signal that switched the 10 GHz linearly chirped square pulses. These particular pulses were chirped by means of self-phase modulation in a highly nonlinear fibre and temporally expanded by a length of negatively dispersive dispersion compensating fibre (DCF) [96]. The control signal carved WDM-replica pulses through cross-phase modulation with the chirped square pulses in the NOLM. The output of the NOLM thus consisted of 4 WDM channels, each having a repetition rate of 10 Gb/s. After filtering out the control signal at the output of the NOLM, one of the WDM channels was selected

through reflection from a tunable fibre Bragg grating filter [97]. The eye diagram of the dropped channel is presented in Fig. 4.23(a). The fibre Bragg grating provided a narrow stop-band of 1.2 nm and a transmission loss of 15 dB. Fig. 4.23(b) shows the spectra after the channel drop.

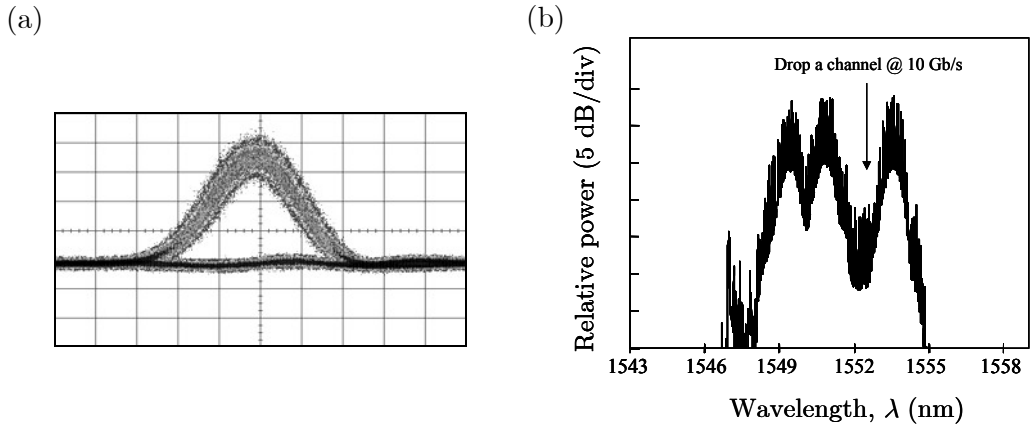

Fig. 4.23. (a) Eye diagram of the dropped channel and (b) the transmission spectra after the channel drop.

A new WDM signal was then added via a circulator. Once amplified, the final WDM signals were then used as control signals for another NOLM. Interaction with a continuous wave from a laser diode operating at 1541.3 nm subsequently transformed them back into 40 Gb/s TDM signals for onward transmission. The bit-error-rate measurements of the whole system showed that error free operation could be achieved with a power penalty between 2 and 4 dB.

4.5 Conclusions and Future Directions

This chapter has demonstrated a simple package for accurate broad-range tuning of the operational wavelength of a fibre Bragg grating, adapted from the beam bending technique. The device can produce uniform and repeatable compression for wavelength shifts up to 110 nm, in precise agreement with the theoretical analysis. Its performance is maintained over the operational regime

with no significant degradation due to PMD and PDL. This package conveniently consumes no power once set to a desired wavelength.

Gratings with a large tuning range will certainly find useful applications in future broadband optical systems, which may have dynamic traffic. Most of these systems would have tight channel separation, thus putting critical requirements on the consistency of their components' performance. The proposed device has been verified to possess this quality under proper design. Nevertheless, the length of the beam should be extended proportionally with the grating length to ensure a uniform stress distribution along the entire grating. In addition, any applied force should not cause the stress in the structure to be greater than the yield stress σ_{yield}, so that the tuning function remains repeatable. By abiding to these guidelines, gratings for any applications such as dispersion compensation, gain equalisation, or a distributed feedback laser, can be effectively tuned using this package.

The prototype device can be improved in many aspects. Use of materials with appropriate thermal expansion coefficients for the beam and the mount could lead to a temperature-stabilised fibre Bragg grating. Its shape can also be redesigned to further reduce its size, resulting in a more compact device. More importantly, the region with uniform stress can be considerably extended by wisely tapering the cross-sectional area of the beam or/and the flexible slab [98]. On the other hand, study of other bend structures may help to find new ways to dynamically reconfigure the grating profile to suit specific applications. This possibly includes investigating the shapes that are provided by commercial stripe actuators. The use of the actuators may result in high precision tuning and also allow tuning with higher frequency oscillations.

Chapter 5

Bragg Grating Package for Variable Dispersion

5.1 Introduction

One of the inherent flaws of optical fibre is the attenuation, which places a requirement for frequent regeneration of the transmitted optical signals. Conventionally, this involves the conversion of the optical signals to electrical signals for amplification. These electronic repeaters are typically placed at every 40 km fibre span, thus contributing significantly to the network system cost and introducing an upper limit to the allowable data bit rate. Nevertheless, the regeneration has the advantage of limiting the accumulation of signal impairments such as optical noise and nonlinearity. On the other hand, amplification in the optical regime can remove the need for these expensive electronic repeaters. Erbium doped fibre amplifiers (EDFAs) can provide gain for signals with wavelengths between 1525 nm and 1560 nm. This range falls within the region at which the loss of the transmission fibre is at its minimum, thus allowing an extended transmission span. However, some of the deployed transmission fibre links were designed for operation in the 1300 nm telecommunications window. This means that these conventional fibres have a zero chromatic dispersion value at this wavelength region. As the fibres also exhibit a nonlinear group delay characteristic, it gives a dispersion value of 17 ps/nm/km near 1550 nm. However, the EDFA exhibits desirable properties such as high gain, high saturation power, a low noise figure and physical compatibility with existing components. Consequently, these overwhelming advantages have forced operation near 1550 nm.

Propagation through a long span of conventional fibre by optical signals within the EDFA band results in large accumulated dispersion. The signal bits disperse linearly with transmission distance, such that after a certain length (referred to as the dispersion limit) it will begin to expand to the adjacent bit slots. In the case of direct detection by a photodiode, this may then generate false bit recognition. This situation becomes more severe as the bit rate goes higher. It is possible to produce fibres with low or even zero dispersion for the 1550 nm wavelength, but the conventional fibres comprise a majority portion of the current global optical transmission architectures. On these accounts, the chromatic dispersion issue has received major attention from researchers, looking for ways to prolong the operation of this enormous investment. Furthermore, the problem has now become more challenging since there is already an increasing demand for telecommunication systems with higher capacity and speed.

This chapter is dedicated to introducing a package for continuously varying the dispersion property of a fibre Bragg grating. Initially, the fundamental concept of dispersion will be briefly discussed, along with the current technological approaches for compensation. Then, the principle exploited in constructing the dispersion-variable device will be explained. Experimental results that illustrate the properties of the device will be presented later. Finally, the applications of the device will be demonstrated through a straightforward compensation test on various lengths of non-zero dispersion shifted fibres and an experimental study on receiver filtering effects in a spectrum-sliced WDM system with semiconductor optical amplifier (SOA)-based noise reduction.

5.2 Chromatic Dispersion Compensation Technologies

Generally, possibilities to confront dispersion exist in the transmitter, in the fibre as well as in the receiver. The transmitter techniques often produce a pulse stream where each leading edge is composed of longer wavelength components than that of the trailing edge. This process can be accomplished by utilising an auxiliary phase modulator [99] or exploiting fibre nonlinearity, namely self phase

modulation (SPM) [100]. As the chirped pulses propagate in a positively dispersive medium, the leading and trailing components in each pulse have to first pass through their own pulse slot completely before reaching their neighbours. The commencement of dispersion impairment is therefore delayed. Additionally, in order to further extend the dispersion length, it was proposed that the pulses should be expanded beyond the clock periods prior to the pre-chirping process [99]. There is also another scheme that makes use of frequency modulation (FM) of the transmitted signals to overcome the dispersion effect, known as dispersion-supported transmission [101]. In this scheme, the FM modulated signals are converted into amplitude modulation at the receiver. These signals are seen as three-level signals as the bits represented by higher frequency light pulses will lag behind and totally occupy the following bit slot at the receiving ends. Consequently, appropriate decoders have to be employed. It is also possible to reduce the effect of dispersion by decreasing the bandwidth of the optical data signals. This can be done using a lithium niobate Mach-Zehnder modulator driven by a three level drive current [102]. Overall, the transmitter techniques often involve additional pieces of equipment with complicated driving circuitry, yet in principle, they can only perform a limited compensation.

Contrary to the previous techniques, receiver based techniques try to recover the data from the pulse streams that have already been distorted by dispersion. Through the coherent detection approach, the optical signals are shifted down to electronic frequency along with the phase information. Consequently, this allows compensation to be performed on the electronic carrier [103]. On the other hand, if direct detection arrangement is used, only the amplitude variations are retained. Fortunately, the distortion to original pulse streams caused by dispersion is predictable. This can be used to deduce the correct data by analyzing a number of preceding bits, or perhaps including the trailing bits [40]. This technique is capable of extending the dispersion length farther than the transmitter technique because dispersion is permitted to have an effect for longer bit periods. However, the complexity from the electronic circuit, as well as the logic and increasing signal-to-noise (SNR) requirement place a constraint on the maximum dispersion length.

Besides dealing with dispersion in the electronic regime, it is more appealing to neutralize the dispersion impairment before the signals reach the detector. Some of the reasons are that the system will be inherently more transparent to any type of data modulation scheme and no speed limitation is imposed by electronic processors, whilst the phase of the signals is securely preserved for the compensation process. Basically, a compensating unit, placed along the transmission fibre link yields an equal amount of negative dispersion. The required negative dispersion can be obtained either from a special fibre, known as dispersion compensating fibre (DCF), or from various types of interferometers. The DCF has a specially designed cross sectional refractive index profile that will cause different wavelength components to have a different mode size [34]. Consequently, the accompanied difference in the effective refractive index will make the shorter wavelength light travel slower than the longer wavelength light. The mode is weakly guided in order to magnify the changes in mode size with wavelength. This leads to an increase in the fibre attenuation (~0.35 dB/km) and bending loss. Since the typical length required for compensating a span of standard single mode fibre is around one sixth of the span length, the accumulated loss will therefore be substantial.

Another interesting approach is to invert the spectrum of the dispersed pulse near the middle of the fibre span so that it may then correct itself while travelling through the remaining span length [39]. The spectral inversion can be accomplished by means of the optical phase conjugation, aided by a nonlinear effect (four-wave mixing). The operating principle of this technique allows dispersion compensation to be performed for any length of fibre. In this process, the carrier wavelength is also shifted and therefore the optimal position of the phase conjugator for exact compensation is slightly away from the middle of the transmission span. Therefore, in the case of WDM systems, channels at other than an exclusively optimized wavelength will either be under or over compensated. Moreover, it requires much more expensive equipment to setup a proper phase conjugator.

Each spectral component of a signal may traverse through a different length when it propagates in an interferometric device. One device possessing such a

property is a Mach-Zehnder interferometer. The relative phase delay of lights propagating in the two arms of a Mach-Zehnder interferometer determines the distribution of the wavelength components in the output ports. Therefore, a cascade of several Mach-Zehnder interferometers with asymmetric arms can provide the required negative dispersion by connecting the output port with shorter wavelength components to the longer arm of the next identical unit [37]. However, this assembly is polarization sensitive, has a limited negative dispersion value and narrow bandwidth. Nevertheless, tunability is possible and the periodic nature of the group delay response may be adapted for compensation of WDM channels. A reflective etalon filter can equally perform dispersion compensation, yet with a simpler construction and polarisation insensitivity. It produces group delay with a negative slope at wavelengths slightly above the resonance, although this is over a narrow bandwidth [36]. The most attractive of all fibre filters is the fibre Bragg grating. This device operates by reflecting only light with a wavelength of twice the grating period. Therefore, by for example linearly decreasing the grating period along the device structure, the shorter wavelength components will be delayed relative to the longer wavelength components [41]. Due to the maturity of the fibre grating fabrication, the bandwidth of operation is extendable and the group delay characteristics may be designed to compensate for higher order dispersion [104]. Additionally, it is polarization insensitive and compact. These advantages cause this technique to advance more rapidly than its counterparts.

Tunability features in the dispersion compensator are becoming more necessary with current development trends of optical networks. One of the reasons is that fibre links are occasionally being replaced or upgraded as a result of aging. These newly installed fibres may have different dispersion properties. Additionally, a ring configuration, that is commonly adopted for network failure recovery, may have a reserve link with a different transmission length than that of the original route. Moreover, reconfigurable networks that allow adding and dropping of multiplexed channels lead to an uncertain amount of cumulative dispersion for a given channel. As system speed is enhanced, the sensitivity to variations in accumulated dispersion becomes more critical, such that dispersion influence increases quadratically with data rates. The variations may stem from

environmental changes or cable movement. In conclusion, it is imperative that the dispersion characteristic of the compensator can be continuously reconfigured to allow networks to cope with changes as they adapt to variable path characteristics, environmental fluctuations and regularly changing configurations.

5.3 DISPERSION

The term dispersion actually refers to the phenomenon of a wavelength dependent refractive index. Therefore in a systems context, different components of a signal pulse travel through a transmission medium at different speeds. This effect causes temporal distortion to the pulse and may eventually cause inter-symbol interference (ISI). However, in optical communication systems, often the dispersion components can be different spectral components (chromatic dispersion) or different transmission modes (intermodal dispersion). Another form of dispersion is polarization mode dispersion, which results from differences in transmission speed for light components with different polarizations. Intermodal dispersion may occur only in multimode fibres as different modes travel at different speeds.

Chromatic dispersion may be caused by the dispersive properties of the waveguide material (material dispersion) and also guidance effects within the fibre structure (waveguide dispersion). Material dispersion results from the variation in the refractive index experienced by the various spectral components of the optical signal. The time delay due to material dispersion after travelling a fibre of length L_f, is given by [105]

$$\tau_m(\lambda) = L_f \frac{d\beta}{d\omega} = \frac{L_f}{c}\left(n_{eff} - \lambda \frac{dn_{eff}}{d\lambda}\right) \tag{5.1}$$

where n_{eff} is the effective refractive index of the mode. The material dispersion parameter D_m, is then defined as

$$D_m(\lambda) = \frac{1}{L_f}\frac{d\tau_m(\lambda)}{d\lambda} = -\frac{\lambda}{c}\frac{d^2 n_{eff}}{d\lambda^2} \tag{5.2}$$

where c is the speed of light in vacuum. Another cause of dispersion is that the cross-sectional distribution of light within the fibre also changes for different wavelengths. This effect is termed as waveguide dispersion. Shorter wavelengths are more confined to the fibre core, while a larger portion of the optical power at longer wavelengths propagates in the cladding. Since the index of the core is greater than the index of the cladding, this difference in spatial distribution causes a change in propagation velocity. The expression for the waveguide dispersion can be derived by considering that the relative refractive index difference Δ, is very small, such that

$$\Delta = \frac{{n_1}^2 - {n_2}^2}{2{n_1}^2} \approx \frac{n_1 - n_2}{n_1} \tag{5.3}$$

where n_1 and n_2 are the refractive index of the core and cladding, respectively, and the fact that $n_1 \approx n_2$ has been exploited. The normalized propagation constant b, is defined as,

$$b = \frac{\left(\beta / k\right)^2 - {n_2}^2}{{n_1}^2 - {n_2}^2} \tag{5.4}$$

where β is the propagation constant of the guided mode and $k = 2\pi / \lambda$ is the propagation constant for light in a vacuum. Taking regard of the fact that $\beta / k \approx n_1$, then the above equation becomes

$$b = \frac{\left(\beta / k\right) - n_2}{n_1 - n_2} \tag{5.5}$$

Since k is also equal to ω / c, where $\omega = 2\pi f$ and f is the frequency, Equation (5.5) can be rearranged as follows,

$$\beta = \frac{\omega}{c}\left[n_2 + \left(n_1 - n_2\right)b\right] \tag{5.6}$$

where c is the speed of light in a vacuum and ω is the angular frequency.

Differentiating this with respect to the angular frequency ω, with an assumption that n_1 and n_2 are both independent of wavelength gives the time

delay explicitly caused by the waveguide dispersion [105]. The time taken to traverse length L_f, of the fibre is thus given by

$$\begin{aligned}\tau_w &= L_f \frac{d\beta}{d\omega} \\ &= \frac{L_f}{c}\left[n_2 + (n_1 - n_2)b\right] + \frac{L_f \omega}{c}(n_1 - n_2)\left(\frac{db}{dV}\cdot\frac{dV}{d\omega}\right)\end{aligned} \tag{5.7}$$

where V is the normalized frequency, given by

$$V = \frac{2\pi}{\lambda} a\sqrt{n_1^{\,2} - n_2^{\,2}} = \frac{\omega}{c} a\sqrt{n_1^{\,2} - n_2^{\,2}} \tag{5.8}$$

where a is the radius of the fibre core.

It can be shown that $dV/d\omega = V/\omega$. Additionally, Equation (5.3) can be substituted in Equation (5.7), giving

$$\begin{aligned}\tau_w &= \frac{L_f}{c}\left[n_2 + (n_1 - n_2)\left(b + V\frac{db}{dV}\right)\right] \\ &= \frac{L_f n_2}{c}\left[1 + \Delta\frac{d(bV)}{dV}\right]\end{aligned} \tag{5.9}$$

Subsequently, the waveguide dispersion parameter D_w, is obtained as

$$\begin{aligned}D_w &= \frac{1}{L_f}\frac{d\tau_w}{d\lambda} = \frac{n_2\Delta}{c}\left(\frac{d^2(bV)}{dV^2}\cdot\frac{dV}{d\lambda}\right) \\ &= -\frac{n_2\Delta}{c\lambda}\left(V\frac{d^2(bV)}{dV^2}\right)\end{aligned} \tag{5.10}$$

where the fact that $dV/d\lambda = -V/\lambda$ has been used. The total chromatic dispersion is simply the addition of these two dispersion contributions, thus giving

$$D(\lambda) = D_m(\lambda) + D_w(\lambda) \tag{5.11}$$

It should be appreciated that Equation (5.11) is only an approximation, as a result of many assumptions have been made throughout the derivation process.

In a real fibre, bends, strain, inhomogenities and imperfections produce low levels of birefringence (a different refractive index for different polarizations). Consequently, one polarization path is delayed relative to the other and results in pulse broadening. This becomes another source of dispersion, which is named polarization mode dispersion (PMD). Degree and orientation of birefringence varies randomly along the length of the fibre. Therefore, birefringence effects may partly average out. PMD does not accumulate linearly with fibre length but instead with the square root of the length. Typically, the magnitude of PMD is 0.05 to 1 ps/km$^{1/2}$. Effective compensation of chromatic dispersion will leave PMD as the largest type of residual dispersion.

Generally, the group delay per unit length of an optical fibre, as a function of wavelength λ, can be expressed in a form of a Taylor series [106] as follows

$$\tau(\lambda) = \tau(\lambda_Z) + (\lambda - \lambda_Z)\frac{d\tau(\lambda)}{d\lambda}\bigg|_{\lambda=\lambda_Z} + \frac{(\lambda-\lambda_Z)^2}{2!}\frac{d^2\tau(\lambda)}{d\lambda^2}\bigg|_{\lambda=\lambda_Z} + \frac{(\lambda-\lambda_Z)^3}{3!}\frac{d^3\tau(\lambda)}{d\lambda^3}\bigg|_{\lambda=\lambda_Z} + \ldots + \frac{(\lambda-\lambda_Z)^n}{n!}\frac{d^n\tau(\lambda)}{d\lambda^n}\bigg|_{\lambda=\lambda_Z} + \ldots \tag{5.12}$$

where λ_Z is the zero dispersion wavelength for the fibre. The measure of chromatic dispersion is then given by

$$\begin{aligned} D(\lambda) &= \frac{d\tau(\lambda)}{d\lambda} \\ &= \frac{d\tau(\lambda)}{d\lambda}\bigg|_{\lambda=\lambda_Z} + (\lambda-\lambda_Z)\frac{d^2\tau(\lambda)}{d\lambda^2}\bigg|_{\lambda=\lambda_Z} + \frac{(\lambda-\lambda_Z)^2}{2!}\frac{d^3\tau(\lambda)}{d\lambda^3}\bigg|_{\lambda=\lambda_Z} \\ &\quad + \ldots + \frac{(\lambda-\lambda_Z)^{n-1}}{(n-1)!}\frac{d^n\tau(\lambda)}{d\lambda^n}\bigg|_{\lambda=\lambda_Z} + \ldots \end{aligned} \tag{5.13}$$

where $d\tau(\lambda)/d\lambda\,|_{\lambda=\lambda_Z}$ becomes zero in both equations since the dispersion takes zero value at this particular wavelength. In standard single mode fibres, it is sufficient to consider only up to the third order dispersion. This means that the time delay function can be simplified to only one quadratic term and the dispersion parameter will then contain only a single linear term. A standard single mode fibre has a step index waveguide with a zero in the dispersion near

1310 nm. The slope $d^2\tau(\lambda)/d\lambda^2\,|_{\lambda=\lambda_Z}$ of D is 0.06 to 0.07 ps/nm^2/km and thus gives the D value of about 17 ps/nm/km in the 1550 nm transmission window.

5.4 Fibre Bragg Grating for Dispersion Compensation

The temporal broadening due to both second and third order chromatic dispersion of a signal pulse at a wavelength λ_0, after travelling a distance L_f, can be derived from the simplified form of Equation (5.13) [107], which gives

$$\begin{aligned}\Delta\tau &= L_f\int_{\lambda_S}^{\lambda_L} D(\lambda_0)\,d\lambda + L_f\int_{\lambda_S}^{\lambda_L}\int_{\lambda_S}^{\lambda_L} D'(\lambda_0)\,d\lambda d\lambda \\ &= L_f D(\lambda_0)\cdot BW + \frac{1}{2}L_f D'(\lambda_0)\cdot BW^2 \end{aligned} \tag{5.14}$$

where $D' = dD/d\lambda$ is the dispersion slope, λ_S and λ_L are the shortest and longest wavelength in the spectrum of the pulse, respectively and $BW = \lambda_L - \lambda_S$.

No dispersion compensation is required if the fibre length is below the dispersion limit or dispersion length. This parameter can be estimated by determining the transmission distance at which a pulse has broadened by one bit interval. It is deduced from Equation (5.14) that only second order dispersion must be compensated if

$$\frac{T_b}{D\cdot BW} < L_f < \frac{2T_b}{D'\cdot BW^2} \tag{5.15}$$

where T_b is the bit period. Therefore, the dispersion slope need not be a concern for single channel compensation as the signal spectrum is very small. However, the third order dispersion obviously becomes significant in WDM systems, in which the dispersion slope must be compensated either channel by channel using compensators with different second order dispersion values or using a single wideband compensator with a nonlinear group delay characteristic.

In order to successfully compensate the dispersion in an optical fibre of length L_f, a fibre Bragg grating has to satisfy the following equation,

$$D_g(\lambda) = -D(\lambda) L_f \tag{5.16}$$

The general expression for the group delay as a function of wavelength for a fibre Bragg grating can be obtained by substituting Equation (5.13) in Equation (5.16) and then integrating it with respect to wavelength, thus giving

$$\begin{aligned}\Delta\tau_g(\lambda) &= -L_f \int_{\lambda_L}^{\lambda} (\lambda - \lambda_Z) \frac{d^2\tau(\lambda)}{d\lambda^2}\bigg|_{\lambda=\lambda_Z} d\lambda \\ &= \frac{L_f}{2}\left[(\lambda_L - \lambda_Z)^2 - (\lambda - \lambda_Z)^2\right] \frac{d^2\tau(\lambda)}{d\lambda^2}\bigg|_{\lambda=\lambda_Z}\end{aligned} \tag{5.17}$$

The above equation can be rewritten to describe the position in the grating structure z, where light with a specific wavelength λ, is being reflected, by using the time to space conversion formula, which is given by

$$\Delta\tau_g(z) = \frac{2n_{eff}(L_g - z)}{c} \tag{5.18}$$

where L_g is the physical length of the grating and $z = 0$ at the beginning of the grating. Additionally, the variation of the grating pitch $\Lambda(z)$, can be obtained by incorporating the phase matching condition, which states that

$$\lambda_B(z) = 2n_{eff}\Lambda(z) \tag{5.19}$$

where $\lambda_B(z)$ is the local Bragg wavelength. The equation for the grating period profile is then given by

$$\Lambda(z) = \frac{1}{2n_{eff}}\left[\lambda_Z + \sqrt{(\lambda_L - \lambda_Z)^2 - \frac{4n_{eff}}{c\tau''(\lambda_Z) L_f}(L_g - z)}\right] \tag{5.20}$$

As validated by Equation (5.15), dispersion compensation of a single channel can disregard the third order dispersion within the bandwidth of that channel. Subsequently, since $BW << \lambda_S, \lambda_L$, it is reasonable to assume that

$$L_f D(\lambda_L) \cdot BW \approx \frac{2n_{eff} L_g}{c} \tag{5.21}$$

which results in a linearly chirped grating profile, given by

$$\Lambda(z) = \frac{1}{2n_{eff}}\left[\lambda_L - BW \cdot \left(1 - \frac{z}{L_g}\right)\right] \tag{5.22}$$

As the proposed tunable dispersion compensator is also used for compensating a single channel, it will thus assume this profile. The tunability incorporated in our device relaxes the precision required for all parameters in the chirp function. Therefore, rough estimations for signal bandwidth, operational wavelength and cumulative dispersion are adequate for design purposes.

5.5 Altering the Local Bragg Wavelength Profile

5.5.1 Origin of Design

As discussed in the earlier Chapter, the local response of the grating can be altered by modifying the grating pitch or the effective refractive index in accordance to the following relationship,

$$\Delta\lambda_B(z) = \lambda_B(z) \cdot (1 - p_e) \cdot \varepsilon(z) \tag{5.23}$$

where p_e is the photo-elastic coefficient of silica, $\Delta\lambda_B(z)$ is the shift in the Bragg wavelength, $\lambda_B(z)$ and $\varepsilon(z)$ are the Bragg wavelength and strain, respectively at particular positions along the grating structure.

The proposed device is designed to compensate a single channel. It is justifiable to consider only the second-order dispersion, thus the grating should have a linearly varying period. The grating is also said to have a constant chirp rate, which is defined as the variation of the Bragg wavelength per unit length of the grating structure. The local Bragg wavelengths at both sides of the grating centre are expected to be shifted oppositely with linearly increasing magnitude along the length of the fibre. This means reconfiguring the strain profile along the grating with the sign changes at the middle of the grating, such that

$$\varepsilon(z) = m_1 \cdot \left(\frac{L_g}{2} - z \right) \tag{5.24}$$

where L_g is the length of the grating structure and m_1 is a constant of proportionality. As a consequence, the bandwidth of the device changes in conjunction with the group delay characteristics. This is because the various spectral components of a signal are no longer being reflected at their former positions in the grating and therefore experience different delays associated with the change in the propagation path distances.

A bending technique is found to be the most efficient way to impart stresses on a piece of fibre [33]. This technique involves transferring the stress in the material completely to the embedded fibre. In a bending beam, a point above the neutral plane will suffer strain with a magnitude obeying the following rule [88],

$$\varepsilon(z) = \frac{h_r}{R(z)} \tag{5.25}$$

where strain $\varepsilon(z)$, is defined as the change in length of a structural element normalized to its original length, h_r is the distance from the neutral plane and $R(z)$ is the local radius of curvature. By assessing the corresponding curvature locally, it is therefore possible to decide the proper bending shape that will be likely to produce the desired stress distribution along the grating structure. But first, the relationship between the deflection and the associated radius of curvature has to be secured.

The derivation begins by recognizing that the length of a circular arc S, is related to the associated radius of curvature R, and sector angle θ, through the following formulae [88],

$$S = R \cdot \theta \tag{5.26}$$

In the case where a curve does not follow the shape of a circular arc, the instantaneous radius of curvature $R(s)$, can be obtained by considering a very small length ds, of the curve which make a very small sector angle $d\theta$. In the

limit where $ds \rightarrow 0$ and $d\theta \rightarrow 0$, the above equation can be rewritten in a form of differential equation, as follows

$$R(s) = \frac{ds}{d\theta} \tag{5.27}$$

where s is a measure of the length of the curve. Fig. 5.1 shows all the variables and axes used in the equations.

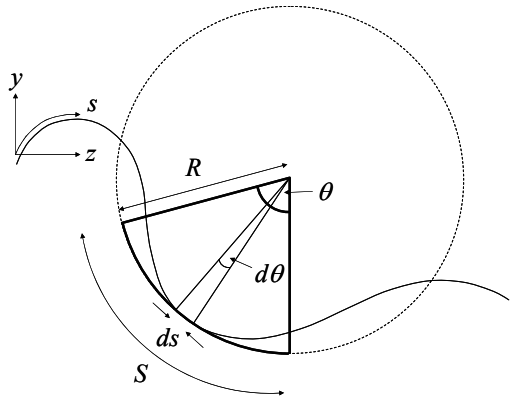

Fig. 5.1. Instantaneous radius of curvature and axes.

Additionally, it is useful to know that the tangent to the curve at a particular coordinate gives the angle between the tangent and the z-axis, that is

$$\tan\theta = \frac{dy}{dz} \tag{5.28}$$

For a small angle, no error is introduced in assuming that $ds \approx dz$ and $\tan\theta \approx \theta$. Consequently, Equation (5.27) can be rewritten as,

$$\frac{1}{R(z)} = \frac{d\theta}{dz} = \frac{d}{dz}\left(\frac{dy}{dz}\right) = \frac{d^2y}{dz^2} \tag{5.29}$$

Finally, it follows from Equation (5.25) and Equation (5.29) that the strain is related to the shape of the curvature as follows,

$$\varepsilon(z) = \frac{h_r}{R(z)} \approx h_r \frac{d^2 y(z)}{dz^2} \tag{5.30}$$

where $y(z)$ is the vertical deflection of various points along the longitudinal axis of the bending material. Therefore, it can be deduced from this equation that in order to obtain the desired linear stress distribution, the curvature should be cubic. Study of structural engineering reveals that two bending conditions may be imposed on a flexible beam to produce the cubic deformation. One condition requires a beam with fixed and free ends, with a load at the free end. The other involves displacing two fixed ends vertically. These bending types are illustrated in Fig. 5.2. The latter produces exactly the required stress distribution as it produces contra-flexure at the centre of the beam. This means that the stress on each side of the beam surface will change sign at this point.

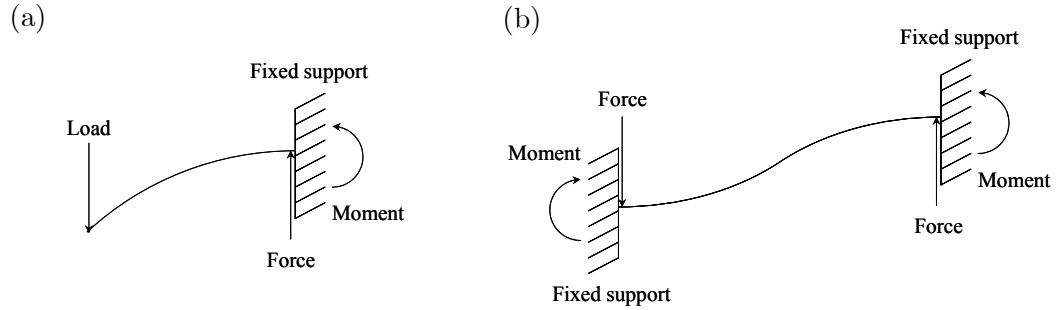

Fig. 5.2. Free-body diagrams of a) a beam with one end fixed and one end free with a load, and b) a beam with both ends fixed and displaced.

5.5.2 Mechanics of Device

The equation that governs the deflection curve can be deduced by first considering the moment of the axial force F_z, about the neutral plane [88]. Consider an element of area dA, at a distance h_r, from some arbitrary location of the neutral surface, Fig. 5.3.

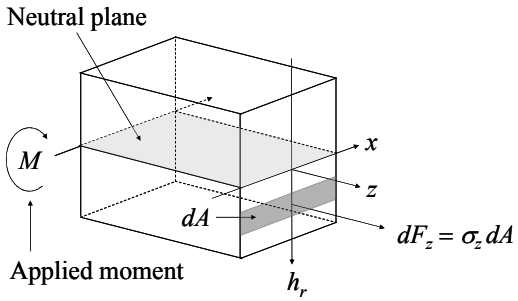

Fig. 5.3. Internal resisting moment.

The total internal resisting moment is

$$\int_A h_r \, dF_z = \int_A h_r \sigma_z \, dA \tag{5.31}$$

where σ_z is the internal stress which is defined as the force acting on a unit area and A is the cross-sectional area. This must balance the external applied moment M, so that for equilibrium

$$\int_A h_r \sigma_z \, dA = M \tag{5.32}$$

For linear-elastic bending, the stress is related to strain as $\sigma_z = E\varepsilon_z$, where E is known as *Young's modulus of elasticity*. Expressing the strain as in Equation (5.25) and then substituting the stress term in the above equation will give

$$M = \int_A h_r \left(E \cdot \frac{h_r}{R} \right) dA = \frac{E}{R} \int_A h_r^{\,2} \, dA \tag{5.33}$$

where $\int_A h_r^{\,2} \, dA$ is called the *second moment of area* of the cross-section about the neutral axis and is denoted by I. Moreover, using the approximation in Equation (5.29) leads to

$$\frac{d^2 y}{dz^2} = \frac{M}{EI} \tag{5.34}$$

This is the general formula that can work out the shape of a beam under the influence of certain bending moments.

This formula will now be used to confirm the shape of a beam with both ends fixed to a rigid body and slightly displaced. Moment equilibrium for this case gives

$$\sum M_x = M - F \cdot \left(\frac{L_z}{2} - z \right) = 0 \tag{5.35}$$

where M_x are moments about the horizontal x-axis that is perpendicular to the z-axis, F is the external force acting vertically and L_z is the horizontal distance between the two beam ends. The moment about one supported end of the beam M, is thus obtained and inserting this in Equation (5.34) yields a second order differential equation as a function of z. It should be readily recognized that the slope of the beam curvature at the supported end must be zero and this point is taken as reference for the vertical displacement of the other end. Applying these boundary conditions, which mathematically are $dy/dz = 0$ and $y = 0$ at $z = 0$, will yield

$$\begin{aligned} y(z) &= \frac{F}{EI} \int_0^z \int_0^z \left(\frac{L_z}{2} - z \right) dz dz \\ &= \frac{F}{EI} \left(\frac{L_z}{4} z^2 - \frac{1}{6} z^3 \right) \end{aligned} \tag{5.36}$$

The displacement between two ends of the beam y_{max}, can be obtained by applying $z = L_z$ in the above equation, which gives

$$y_{max} = \frac{F}{EI} \cdot \frac{{L_z}^3}{12} \tag{5.37}$$

Subsequently, the deflection equation can be expressed in terms of the maximum deflection as the following

$$y(z) = \frac{y_{max}}{{L_z}^3} \cdot (3L_z z^2 - 2z^3) \tag{5.38}$$

Differentiating the above equation twice with respect to z will give the corresponding stress. It clearly shows that the stress is linear along the beam with the gradient directly proportional to the magnitude of the maximum deflection.

5.5.3 Description of Device

The gradient of the stress will in fact influence the dispersion property of a fibre Bragg grating, which is embedded at some positive or negative distance h, from the neutral axis of the bending beam. It should be noted that it is possible to vary this parameter continuously, as well as to change its sign for a specified value of h. Ideally, the beam length L_b , must always remain constant at any deflection amplitude in order to ensure that the point of zero stress is always at the middle of the span of the grating. However, the design of the device will be more relaxed if the beam length is allowed to vary slightly and instead, the horizontal distance of the beam ends L_z , is kept constant. In order to ensure minimal error, a sizeable value of h should be used so that only a very small deflection is required for a desired tuning range of dispersion. The assumption of $L_z = L_b$ will thus result in an unnoticeable shift in the measured centre wavelength.

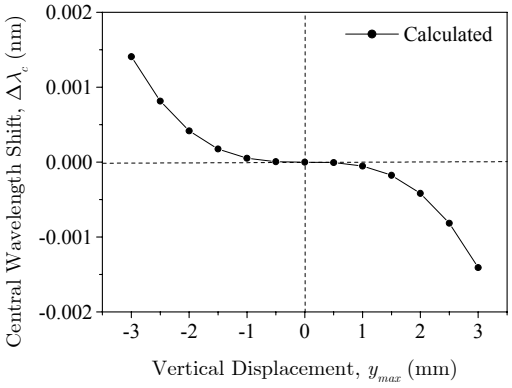

Fig. 5.4. Calculated central wavelength shift against vertical displacement for the worst case scenario with L_z = 100 mm, h = 1.2 mm and λ_{C0} = 1550 nm.

Moreover, if the point of zero stress remains at the centre of the grating, such that the *guided* beam ends have slid the same distances, the centre wavelength of the grating bandwidth will also remain stationary. The worst case occurs if one of the beam ends does not move at all and only the other end slides to conform to the bending conditions. This is depicted in Fig. 5.4, which shows the shift of the centre wavelength of a chirped Bragg grating, embedded at $h = 1.2$ mm from the beam neutral plane. The calculation assumes a distance of 100 mm for L_z. This fibre Bragg grating originally has a centre wavelength at 1550 nm. It can be seen that the central wavelength excursion is indeed very small, which is always less than 2 pm, and thus is acceptable for most applications.

The graph is obtained by evaluating the Bragg wavelength at the middle span of the grating structure in response to the stress distribution for a particular value of the maximum vertical deflection. Combining Equation (5.23), Equation (5.30) and Equation (5.38) will result in

$$\Delta\lambda_C\left(y_{max}\right) = -\frac{12\cdot y_{max}\cdot h\cdot\left(1-p_e\right)\cdot\lambda_{C0}}{{L_z}^3}\cdot\left(\frac{L_z}{2}-z_C\left(y_{max}\right)\right) \tag{5.39}$$

where $\Delta\lambda_C$ is the central wavelength shift due to the applied strain, z_C is the z-coordinate of the grating centre point and λ_{C0} is the initial central wavelength of the fibre Bragg grating. The z-coordinate of the grating middle point can be obtained from the inverse function of the following equation,

$$s\left(z\right) = \int_0^z \sqrt{1+\left(\frac{dy}{dz}\right)^2}\,dz \tag{5.40}$$

where s is the axial position along the neutral axis of the beam (i.e. arc length) which corresponds to a specified value of z. In order to produce the graph in Fig. 5.4, the above formula is solved numerically, with a calculation tolerance of 10^{-15} and by substituting $z = L_z/2$.

The desired arrangement as previously discussed is constructed simply from a composite beam, a pair of clamps and a translation stage. The composite beam is made from two types of materials with a massive difference in their *Young's*

modulus E, value (∼50:1). These materials are bonded together using strong adhesive solution, such that the material with the bigger E essentially defines the neutral axis, whilst the lower E material embeds the fibre Bragg grating and roughly specifies h. We use a combination of hardened steel and plastic to form the composite beam. The plastic should be flexible but it needs to show sufficient hardness to resist indentation caused by a moderate load. The beam is firmly supported by a pair of clamps in a perfectly straight position and at equal level. Both of the clamps must be frictionless to ensure that no unwanted axial forces will act on the beam. One of the clamps is mounted on a linear translation stage that is oriented in a perpendicular direction. The stage is driven mechanically by a high resolution screw and can be moved in either a forward or backward direction. Fig. 5.5 illustrates the proposed device.

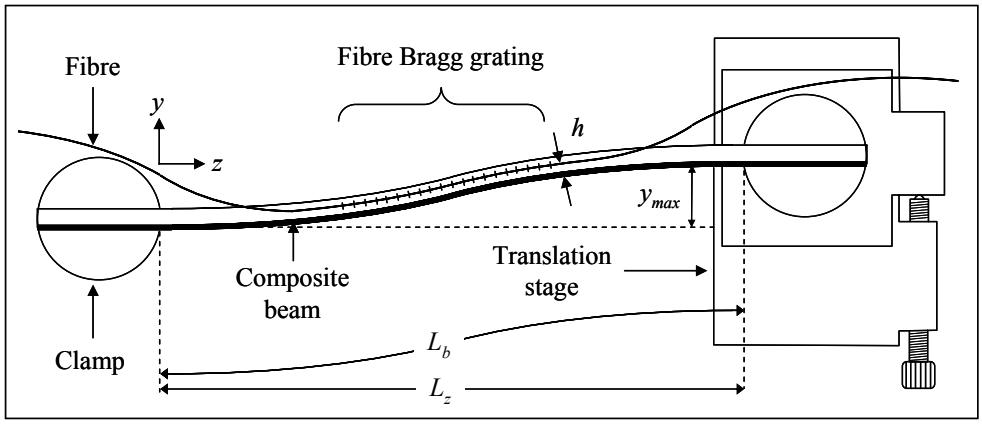

Fig. 5.5. Schematic structure of the variable dispersion device.

5.5.4 Characterization of Device

The magnitude of dispersion of the device can be predicted by first calculating the difference of the Bragg wavelengths of two specific points along the embedded chirped fibre Bragg grating. For a particular maximum deflection

y_{max} , the difference between the longer and shorter Bragg wavelengths can be expressed as,

$$\Delta\lambda_{\Delta L}\left(y_{max}\right) = \lambda_B\left(s_L, y_{max}\right) - \lambda_B\left(s_S, y_{max}\right) \tag{5.41}$$

where λ_B denotes the Bragg wavelength, while s_L and s_S are the positions along the grating's longitudinal axis for the assessed points of reflection. Assuming that the centre of the fibre Bragg grating always remains at $z = L_z / 2$ at all bending positions, these points are given by,

$$s_S\left(y_{max}\right) = \frac{1}{2}\left[L_b\left(y_{max}\right) - \Delta L\right] \tag{5.42a}$$

$$s_L\left(y_{max}\right) = \frac{1}{2}\left[L_b\left(y_{max}\right) + \Delta L\right] \tag{5.42b}$$

where L_b can be readily obtained from Equation (5.40) with substitution of $z = L_z$ and $\Delta L = s_L - s_S$, that is the separation distance. By using Equation (5.23), Equation (5.30) and Equation (5.38), Equation (5.41) can be rewritten as,

$$\begin{aligned}\Delta\lambda_{\Delta L}\left(y_{max}\right) = &\left[\lambda_B\left(s_L, 0\right) - \lambda_B\left(s_S, 0\right)\right] + \\ &\lambda_{C0}\cdot\left(1 - p_e\right)\cdot\varepsilon'\left(y_{max}\right)\cdot\left[z_L\left(y_{max}\right) - z_S\left(y_{max}\right)\right]\end{aligned} \tag{5.43}$$

where $\varepsilon' = d\varepsilon / dz$, while the z-coordinate of s_L and s_S are denoted by z_L and z_S, respectively and can be obtained by using the inverse function of Equation (5.40). The first term is merely the initial Bragg wavelength difference between the points. Subsequently, the corresponding dispersion values are obtained by using the following approximation,

$$D\left(y_{max}\right) = \frac{2n_{eff}\cdot\Delta L}{c\cdot\Delta\lambda_{\Delta L}\left(y_{max}\right)} \tag{5.44}$$

The spectral and group delay responses of the device under various magnitudes of maximum vertical deflection are measured using the characterization rig described in Chapter 1. Fig. 5.6 shows the spectra of a chirped fibre Bragg grating with $L_g = 50\,\text{mm}$ and $D_0 \approx 173\,\text{ps/nm}$. The effective refractive index modulation $\eta\cdot\Delta n$ of the grating was roughly 2.3×10^{-4} and

30% of the total length was apodised at each end. This grating was embedded at $h \approx 1.15\,\text{mm}$ away from the neutral axis of a beam, which was fixed by clamps with separation distance $L_z = 100\,\text{mm}$. The measured spectra exhibit a negligible excursion of the central operating wavelength from its initial value of $\lambda_{C0} \approx 1549.8\,\text{nm}$, as expected. In addition, the corresponding time delay responses are shown in Fig. 5.7. It shows that the measured temporal ripple is approximately ±5 ps in all operating conditions. This graph only displays the responses within the 3-dB bandwidth.

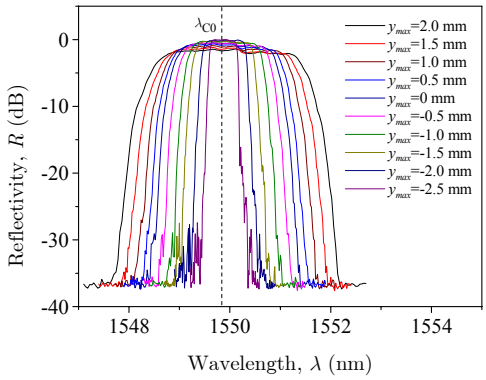

Fig. 5.6. Measured spectral responses of the variable dispersion grating.

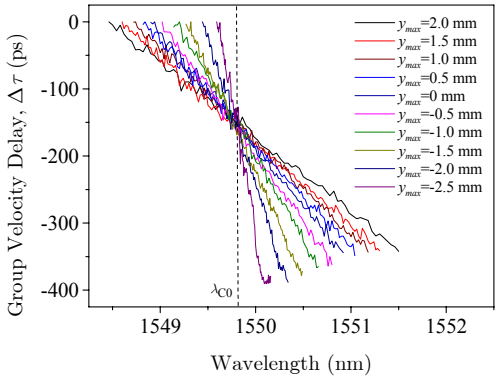

Fig. 5.7. Measured group velocity delay responses of the variable dispersion grating.

The measurements of the dispersion magnitudes of the device against the maximum vertical deflections are presented in Fig. 5.8, overlaid with the theoretical curve generated from Equation (5.44). The measured values are obtained by evaluating the grating delay characteristics within the 3-dB bandwidth using the *least-squares fitting* method. On the other hand, the theoretical dispersion curve results from analyzing the Bragg wavelength differences between the two edges of the grating structure, such that $\Delta L = L_g$ for several bending positions. The plot for the corresponding 3-dB bandwidth measurements is also shown in Fig. 5.8, together with the theoretical values obtained via the transfer matrix method.

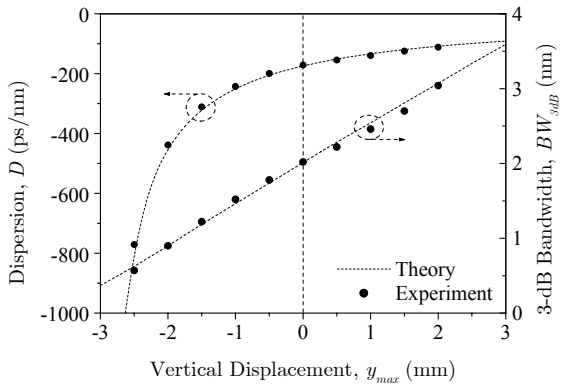

Fig. 5.8. Dispersions and 3-dB bandwidths against deflection amplitudes.

5.6 Demonstrations of Device Application

5.6.1 Chromatic Dispersion Compensation

The device was successfully used to compensate the chromatic dispersion in a non-zero dispersion shifted fibre of length approximately 40 km. This fibre had zero dispersion at a wavelength near 1460 nm and dispersion slope of roughly 0.05

ps/nm^2/km. In order to compensate this length of fibre, the device was adjusted to provide a dispersion value of -173.2 ps/nm, at which its 3-dB bandwidth was around 2 nm. The time delay responses of the optical fibre and the proposed device adjusted exactly to the negative dispersion value of the fibre is shown in Fig. 5.9, superimposed with the time delay response measured after the fibre and the device.

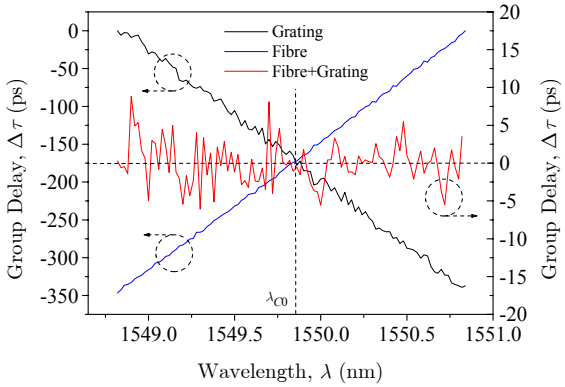

Fig. 5.9. Individual group delay responses for the fibre Bragg grating and transmission fibre and the magnified response after compensation.

An experiment on optical data transmission was done in collaboration with the "optical communications system group", in particular Mr. Michael Roelens (research student) and Dr. Benn Thomsen (research fellow). Optical pulses were generated by carving the continuous wave (CW) light from a semiconductor DFB laser operating at 1550 nm [108]. The pulse carving process was accomplished using a dual-drive Mach-Zehnder interferometer in a form of Lithium Niobate ($LiNbO_3$) modulator. The modulator was dc biased at a peak of its switching characteristic and driven sinusoidally between two adjacent minima at a frequency of 5 GHz. In order to yield a return-to-zero (RZ) pulse source with 10% duty-cycle, the chirped-pulse-compression technique was utilized. The resulting pulse train with a repetition rate of 10 GHz was chirped using a phase modulator driven at the same frequency. The phase modulator was also a $LiNbO_3$ modulator.

The magnitude of the driving voltage was set such that compression by 5 km of standard single-mode fibre (SMF) produced pulses with approximately 10 ps width. These output pulses were then modulated with 10 Gb/s PRBS data and transmitted through 40 km and 80 km non-zero dispersion shifted fibres, once amplified by an erbium-doped fibre amplifier (EDFA). Finally, the dispersion compensation of the transmitted optical data was performed by our proposed device at the end of the fibre span, where it is adjusted to the appropriate negative dispersion values. The whole system setup is illustrated in Fig. 5.10.

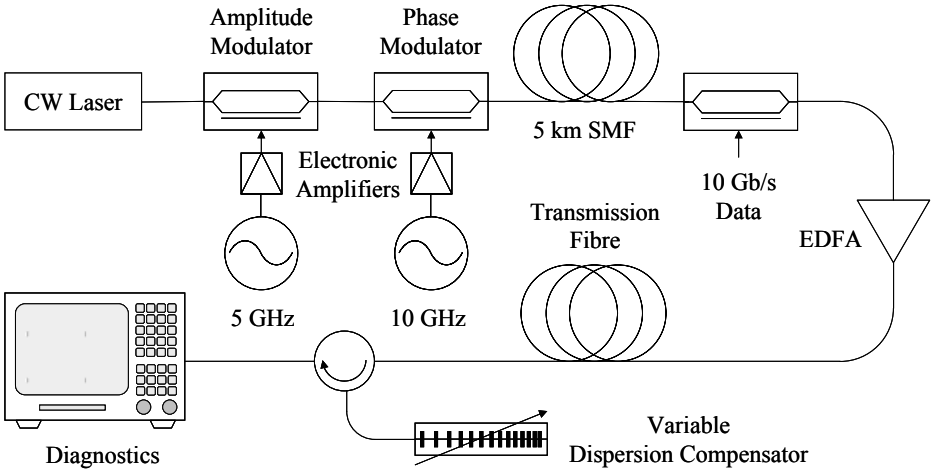

Fig. 5.10. Experimental setup.

The performance of the system was diagnosed through the Q measurements [109], in which dispersion compensations after transmissions over 40 km and 80 km fibre produced Q-value of 19.5 dB and 17.5 dB, respectively. Therefore, the penalties were small in relation to the Q-value obtained from the back-to-back operation, which was 21 dB. The eye diagrams for the dispersion compensated transmissions over 40 km and 80 km fibres are shown in Fig. 5.11. The eye was hardly open without the dispersion compensation.

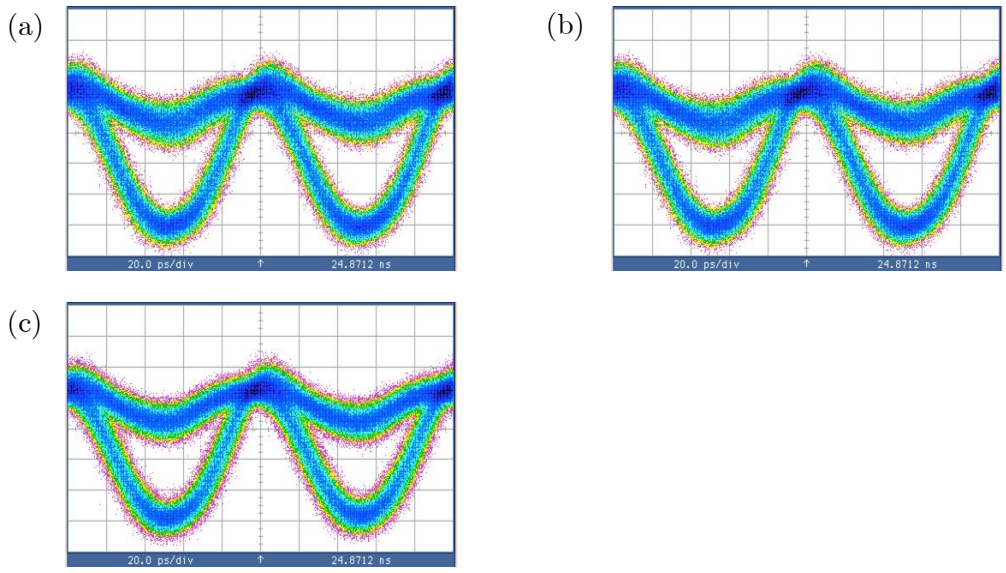

Fig. 5.11. Eye diagrams for a) back-to-back operation and dispersion-compensated transmissions over b) 40 km and c) 80 km fibres.

5.6.2 Bandwidth-Variable Filter for Spectrum-Sliced WDM System Experiment

Our proposed device has aided an experimental study on receiver filtering effects in a spectrum-sliced WDM system using semiconductor optical amplifier (SOA)-based noise reduction [110]. This experiment was exclusively carried out by Mrs. Anoma D. McCoy, a member of the "optical communication system group". In the experiment, incoherent light originated from an EDFA was subsequently polarized and equally coupled into three optical paths. Three channels were generated by individually slicing a band of spectrum with a fibre Bragg grating with a 3-dB bandwidth of approximately 0.24 nm in each path. Each output was then intensely amplified by an EDFA and fed into an SOA. The SOA was compelled to operate in the non-linear regime and thus enabled the intensity noise suppression procedure. The processed light was then modulated with 2.5 Gb/s PBRS data through an $LiNbO_3$ modulator. All channel signals

were then wavelength-division multiplexed using a passive coupler. Finally, our device which in this demonstration, comprised a 30 mm fibre Bragg grating, was placed just before detection, wherein the ability to continuously vary the bandwidth of the device was exploited to define the bandwidth of the received signal. The schematic of the system is illustrated in Fig. 5.12.

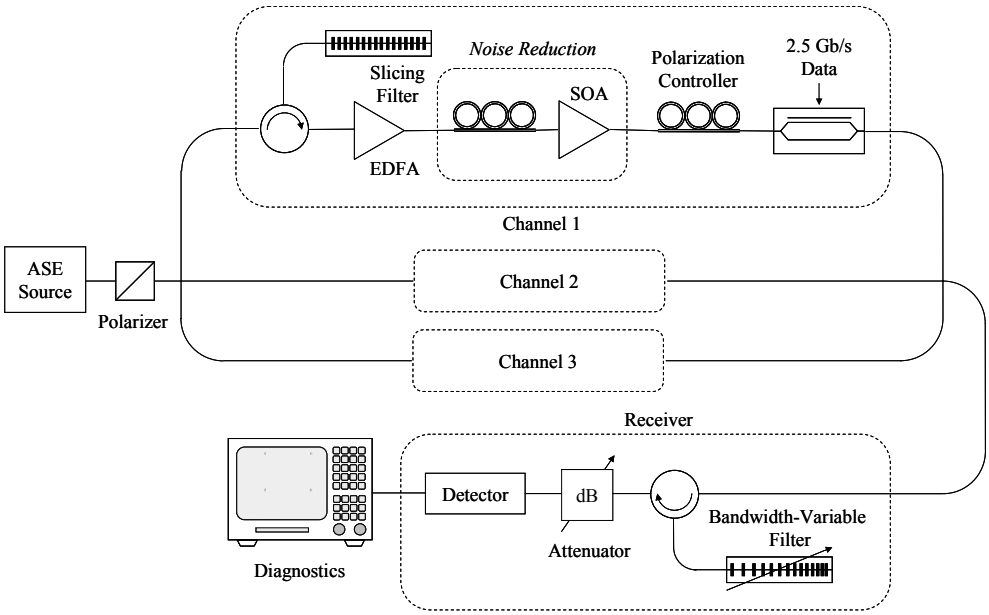

Fig. 5.12. Experimental setup.

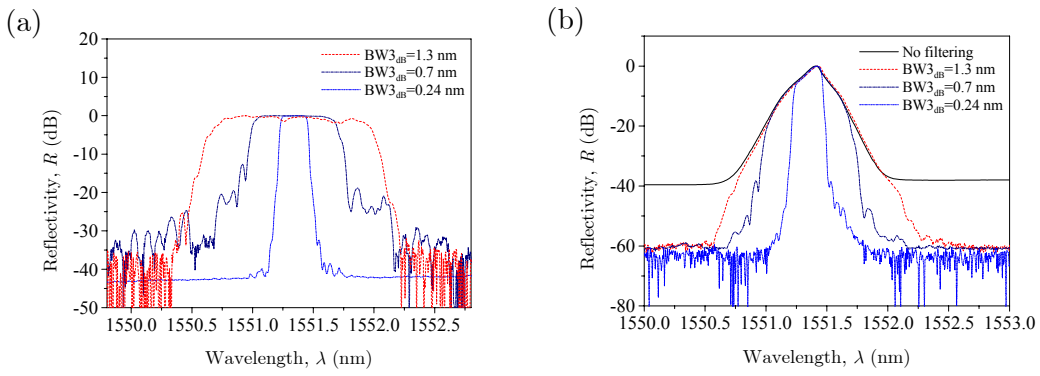

Fig. 5.13. Spectra of the a) bandwidth-variable filter and b) filtered detector input.

The filtered spectra of the transmitted signal are shown in Fig. 5.13, along with the spectral responses of the bandwidth-variable filter. The dispersive behaviour of our device has no implication to a low bit rate system, such as this case. Instead, the system performance is influenced by the degree of depletion of the intensity noise suppression effect caused by the wavelength-division demultiplexing process, as well as the inter-channel crosstalk. The measurements of Q-factor as a function of receiver filter bandwidth are shown in Fig. 5.14 for spacings of 0.6, 0.8 and 1.0 nm. Conclusively, through analysis of the Q-measurements of the system in response to the varying demultiplexer bandwidths, our device allows the determination of the optimum bandwidth of demultiplexers for such systems.

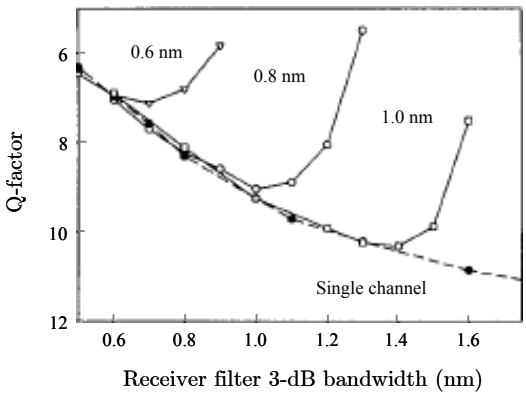

Fig. 5.14. Three channel system Q measurements at 0 dBm for varying filter width and channel spacing. Single channel measurements are also shown.

5.7 Conclusions and Future Directions

Chirped fibre Bragg grating can be effectively utilized as a dispersion compensation unit. This is attributable to the maturity of the fabrication technology which allows production of high quality grating structures that show

nearly smooth group delay characteristics. In order to continue being the top technology, this device has to adapt to the next generation of optical fibre networks wherein flexible traffic management becomes mandatory. Its characteristics should therefore able to be conveniently reconfigured or tuned.

Mechanical stress provides the most efficient method to dynamically modify the characteristics of a fibre Bragg grating. We therefore adopt this technique to craft a dispersion-variable device. The mechanics of the device have been presented in detail and its characteristics have been evaluated experimentally. Various dispersion measurements agreed well with those obtained theoretically, and such predictable behaviour is beneficial for tuning procedure. This observation encourages the demonstration of the device application in a 10 Gb/s optical data transmission system. Error free transmissions for distances of up to 80 km have been successfully undertaken. This length coincides with a typical optical amplifier span, thus this device may be readily integrated in a repeater module. The package does not continuously drain electrical power, such that it no longer requires electrical power once set to a desired operating condition. In a separate experiment, the bandwidth-variable property of the device has been utilized in a study on receiver filtering effects in a spectrum-sliced WDM system using semiconductor optical amplifier (SOA)-based noise reduction. In this experiment, it served as a convenient tool to determine the optimum demultiplexer bandwidth for the system with specific channel spacing.

The proposed device is capable of fully compensating the chromatic dispersion in an optical amplifier span and therefore should allow the actual long-haul optical transmission. This could be experimentally tested by using the "circulating loop transmission experiment" [111]. It however places a stringent requirement on the quality of the grating since noise sources due to intensity or phase ripples are cumulative for such an arrangement. Unlike the actual system, the usage of multiple fibre Bragg gratings averages the effect of the ripples. Nevertheless, it may also be possible to yield the averaging effect in the circulating loop transmission system by lightly vibrating the package at high frequency.

The adjustable bandwidth property of the device may find further applications in the optical networks, for instance as a multi-channel band-pass filter for selecting a varying number of channels. Such multi-wavelength as well as high bit rate systems prefer that all network components are dispersionless. Our proposed device can be transformed into a dispersionless bandwidth-variable filter through addition of an identical fibre Bragg grating with equal dispersion magnitude but opposite sign. Total cancellation of the intrinsic dispersion is accomplished by feeding the output of the first fibre Bragg grating into the second one through the shorter wavelength end. The second fibre Bragg grating should be embedded at exactly the same distance from the neutral axis as the first one.

In conclusion, our simple package can conveniently convert a fibre Bragg grating into a variable dispersion compensator or bandwidth-variable bandpass filter. The device characteristics are predicted and described mathematically, thus facilitating the design process. It has the benefits of minimal electrical power consumption, inherently polarization insensitivity and transparency to any data modulation scheme or speed. Moreover, the package offers great design flexibility, such that fibre Bragg gratings of any length can be accommodated through appropriate adjustments of the distance between clamps and the grating's distance from the neutral axis. In view of all the abovementioned advantages, we are therefore confident that this device could secure applications in the future optical communication networks.

Chapter 6

Conclusions

There are now practically no limits on the design of fibre Bragg gratings as the fabrication systems have reached maturity. They have infiltrated into virtually all applications in optical systems and exhibited exceptional performances. It now needs to evolve into a fully reconfigurable or tunable device as the optical communication systems are progressing towards truly flexible networks. This thesis emphasizes on the design of fibre Bragg grating filters for applications in optical communication systems, where the majority would incorporate tunability. We have designed gain flattening filters from a targeted spectrum without utilising the layer-peeling inverse scattering method. We have also proposed a novel reconfigurable optical phase code generator. A simple package for continuous wideband tuning of fibre Bragg gratings has also been proposed. Finally, we have demonstrated a package for variable dispersion of fibre Bragg gratings.

All-optical long haul optical transmission systems are made possible by employing erbium-doped fibre amplifiers (EDFA). However, the variation in the gain spectrum causes detrimental effects on multi-channel systems. Fibre Bragg gratings can be used to even out the excessive powers from channels that have experienced higher amplifications. Empirical observations suggest that the magnitude of the transmission loss caused by fibre Bragg gratings indeed depends on the chirp rate as well as the refractive index change. The fitting formula can be used to design a grating from a desired spectral profile. We utilised this approach to design fibre Bragg grating filters to be used in a transmission configuration. Chapter 2 provides a full description of these filters, which comprises fibre Bragg gratings with either modulated refractive index change or

chirp rate. It is shown that the design procedure could produce gain flattening filters of acceptable quality through simulations using the transfer matrix method. This alternative approach is conceptually simpler than the inverse scattering method. Moreover, it offers precise control over all parameters of the grating structure.

Owing to the available advanced fabrication systems, fibre Bragg gratings can be freely moulded into complex signal filters. This opens up an opportunity for exploitation in optical code-division multiple access (OCDMA) operation. Its successful operation is no longer of doubt, yet true advantage should emerge only if it becomes reconfigurable. In light of this, we proposed a simple approach for generating phase codes, utilising a uniform fibre Bragg grating. Full description of the device can be found in Chapter 3. Phase modulation of a reflected signal was achieved through the thermo-optic effect, induced by several fine heating elements. We were able to demonstrate up to 16 bit code sequence with error free signal recognition. This included applications in a simple coding-decoding configuration and later extended to a bidirectional clock-distributed architecture. This device has been comprehensively analysed in theory, as well as experiments.

Fibre Bragg gratings demonstrated excellent performance in spectral and phase responses in many sorts of applications. However, the necessity to evolve into a tunable device exists in order to become one of the enabling components of truly flexible optical communication systems in the foreseeable future. The small dimension of the FBG apparently permits structural modification for active adjustment of its characteristics. This primarily involves changes in the grating period. However, the material in which the grating is formed is brittle and fragile. Therefore, any application of mechanical forces would be a delicate procedure. Many approaches in applying stress on a FBG have failed to achieve large tunability, as the fibre can easily break prematurely. We were able to delay this occurrence by embedding the grating in a flexible plastic slab, which helps holding the fibre firmly and thus preventing it from slipping from the fibre longitudinal axis. The stress is obtained through bending, the magnitude of which is enhanced through utilisation of composite beam. The beam is shaped by a simple package, which directs necessary forces for appropriate bending moments.

A continuously tunable fibre Bragg grating is demonstrated in Chapter 4, which was able to achieve over 110 nm tuning range. The concept and construction of this device are clearly presented. The accompanying mathematical description provides accurate prediction of the operational wavelength. The performance limitation of this device has been studied in terms of insertion loss, spectral deformation, differential group delay (DGD) and polarisation dependent loss (PDL). This study revealed that spectral response remains consistent throughout the tuning process, implying uniform stress distribution along the grating. On the other hand, an unexpected insertion loss was observed at intense magnitude of stress. Through observation of the effect of intense stress on fibres with various compositions, it was concluded that photosensitivity may promote the effect. This is verified by a reduction of the stress point of massive insertion loss in case of boron-codoped germanosilicate fibre with respect to a standard fibre. Moreover, this point shifted up upon UV-exposure. DGD and PDL measurements showed no change from their intrinsic value, at least within the operational limit of the measurement equipment, which was coincidentally below the stress point of massive insertion loss. Conclusively, this device can perform very well when operating below the discussed point. This fact is supported by the demonstrations of the device application in some crucial optical systems. Namely, it has been used as a resonator mirror for high power fibre lasers and an add/drop filter for an all-optical time-division multiplexed (TDM) to wavelength-division multiplexed (WDM) system. Additionally, the package has successfully accommodated an all-fibre distributed feedback laser (DFB).

The same approach has also been exploited for constructing a fibre Bragg grating filter with variable dispersion. The description of this particular device is documented in Chapter 5. The package is designed to produce linear stress along an off-axis plane of a bending beam. This is achieved by vertically displacing the two ends of an elastic beam. The generated shape has a point of zero stress at the middle of the beam. Consequently, the time delay characteristic of an embedded uniform or chirped fibre Bragg grating will be linearly varied with the centre operating wavelength remaining constant. This device is capable of executing an error free point-to-point data transmission of a single channel at 10 Gb/s data rate. Additionally, another useful property is that the spectrum bandwidth

increases with the stress gradient. It immediately found an application in a spectrum-sliced WDM test system as a bandwidth-variable filter. These two behaviours were shown to be mathematically predictable.

We have therefore added a few more novel forms of fibre Bragg grating devices. Conclusively, these devices could become apart of the future optical communication systems as supported by the convincing results from several laboratory experiments presented in this thesis. Combining with further improvement in the fibre Bragg grating fabrication, the simplicity of techniques in modifying its characteristics as illustrated in the previous chapters would be an extra advantage that will put this technology ahead of its rivals.

BIBLIOGRAPHY

[1] K. O. Hill, Y. Fujii, D. C. Johnson and B. S. Kawasaki, "Photo-sensitivity in optical fiber waveguide: Application to reflection filter fabrication", *Appl. Phys. Lett.*, vol. 32, no. 32, pp. 647-649, 1978.

[2] M. Cole, W. H. Loh, R. I. Laming, M. N. Zervas and S. Barcelos, "Moving fiber/phase-mask scanning beam technique for enhance flexibility in producing fiber gratings with a uniform phase-mask", *Electron. Lett.*, vol. 31, no. 17, pp. 1488-1489, 1995.

[3] C. R. Giles, "Lightwave applications of fiber Bragg gratings", *J. Lightwave Technol.*, vol. 15, no, 8, pp. 1391-1404, 1997

[4] T. Otani, T. Kawazawa, K. Goto, N. Takeda and S. Akiba, "16 channel 2.5 Gbit/s WDM transmission experiment over 9000 km by using gain equalised amplifier repeaters", *Electron. Lett.*, vol. 33, no. 4, pp. 309-310, 1997.

[5] P. C. Becker, N. A. Olsson and J. R. Simpson, "Erbium-Doped Fiber Amplifiers: Fundamentals and Technology", Academic Press, 1999.

[6] A. R. Chraplyvy, J. A. Nagel and R. W. Tkach, "Equalization in amplified WDM lightwave transmission systems", *IEEE Photon. Technol. Lett.*, vol. 4, no. 8, pp. 920-922, 1992.

[7] J. Li, F. Khaleghi and M. Kavehrad, "Gain equalization by mitigating self-filtering effect in a chain of cascaded EDFA's for WDM transmissions", *J. Lightwave Technol.*, vol. 13, no. 11, pp. 2191-2196, 1995.

[8] H. Ono, M. Yamada, T. Kanamori and Y. Ohishi, "Low-noise and high-gain 1.58 μm band Er^{3+}-doped fibre amplifiers with cascade configurations", *Electron. Lett.*, vol. 33, no. 17, pp. 1477-1479, 1997.

[9] H. Masuda, K. I. Suzuki, S. Kawai and K. Aida, "Ultra-wideband optical amplification with 3 dB bandwidth of 65 nm using a gain-equalised two-stage erbium-doped fibre amplifier and Raman amplification", *Electron. Lett.*, vol. 33, no. 9, pp. 753-754, 1997.

[10] S. Yoshida, S. Kuwano and K. Iwashita, "Gain-flattened EDFA with high Al concentration for multistage repeatered WDM transmission systems", *Electron. Lett.*, vol. 31, no. 20, pp. 1765-1767, 1995.

[11] M. Yamada, T. Kanamori, Y. Terunuma, K. Oikawa, M. Shimizu, S. Sudo and K. Sagawa, "Fluoride-based Erbium-doped Fiber Amplifier with Inherently Flat Gain Spectrum", *IEEE Photon. Technol. Lett.*, vol. 8, no. 7, pp. 882-884, 1996.

[12] M. Tachibana, R. I. Laming, P. R. Morkel and D. N. Payne, "Erbium-Doped Fiber Amplifier with Flattened Gain Spectrum", *IEEE Photonics Technol. Lett.*, vol. 3, no. 2, pp. 118-120, 1991.

[13] M. Wilkinson, A. Bebbington, S. A. Cassidy and P. McKee, "D-fibre filter for erbium gain spectrum flattening", *Electron. Lett.*, vol. 28, no. 2, pp. 131-132, 1992.

[14] R. A. Betts, S. J. Frisken and D. Wong, "Split-beam Fourier filter and its application in a gain-flattened EDFA", *Proc. Conference on Optical Fiber Communication (OFC)*, vol. 8, paper TuP4, pp. 80-81, 1995.

[15] S. F. Su, R. Olshansky, D. A. Smith and J. E. Baran, "Flattening of erbium-doped fibre amplifier gain spectrum using an acousto-optic tunable filter", *Electron. Lett.*, vol. 29, no. 5, pp. 477-478, 1993.

[16] J. Pan, M. A. Ali, A. F. Elrefaie and R. E. Wagner, "Multiwavelength Fiber-Amplifier Cascades with Equalization Employing Mach-Zehnder Optical Filter", *IEEE Photon. Technol. Lett.*, vol. 7, no. 12, pp. 1501-1503, 1995.

[17] H. Taga, N. Takeda, K. Imai, S. Yamamoto and S. Akiba, "110 Gbit/s (22 x 5 Gbit/s), 9500 km transmission experiment using 980 nm pump EDFA 1R repeater without forward error correction", *Proc. Optical Amplifiers and Their Applications (OAA)*, paper PDP5, pp. 28-31, 1996.

[18] J. C. Dung, S. Chi and S. Wen, "Gain flattening of erbium-doped fibre amplifier using fibre Bragg gratings", *Electron. Lett.*, vol. 34, no. 6, pp. 555-556, 1998.

[19] R. Kashyap, R. Wyatt and P. F. McKee, "Wavelength Flattened Saturated Erbium Amplifier using Multiple Side-tap Bragg Gratings", *Electron. Lett.*, vol. 29, no. 11, pp. 1025-1026, 1993.

[20] A. M. Vengsarkar, P. J. Lemaire, J. B. Judkins, V. Bhatia, T. Erdogan and J. E. Sipe, "Long-period Fiber Gratings as Band-rejection Filters", *J. Lightwave Technol.*, vol. 14, no. 1, pp. 58-65, 1996.

[21] M. Ibsen, M. K. Durkin, M. N. Zervas, A. B. Grudinin and R. I. Laming, "Custom Design of Long Chirped Bragg Gratings: Application to Gain-Flattening Filter with Incorporated Dispersion Compensation", *IEEE Photon. Technol. Lett.*, vol. 12, no. 5, pp. 498-500, 2000.

[22] P. R. Prucnal, M. A. Santoro and T. R. Fan, "Spread spectrum fiber-optic local area network using optical processing", *J. Lightwave Technol.*, vol. 4, no. 5, pp. 547-554, 1986.

[23] N. Wada and K. Kitayama, "A 10Gb/s optical code division multiplexing using 8-chip optical bipolar code and coherent detection", *J. Lightwave Technol.*, vol. 17, no. 10, pp. 1758-1765, 1999.

[24] H. Tsuda, H. Takenouchi, T. Ishii, K. Okamoto, T. Goh, K. Sato, A. Hirano, T. Kurokawa and C. Amano, "Spectral encoding and decoding of 10Gb/s femtosecond pulses using high resolution arrayed-waveguide grating", *Electron. Lett.*, vol. 35, no. 14, pp. 1186-1188, 1999.

[25] H. Fathallah, L. A. Rusch and S. LaRochelle, "Passive Optical Fast Frequency-Hop CDMA Communications System", *J. Lightwave Technol.*, vol. 17, no. 3, pp. 397-405, 1999.

[26] P. Boffi, D. Piccinin, P. Parolari, R. Aldeghi and M. Martinelli, "Programmable fiber Bragg gratings for spectral CDMA", *Proc. Conference on Lasers and Electro-Optics (CLEO)*, pp. 578-579, 2000.

[27] L. R. Chen, "Flexible fiber Bragg grating encoder/decoder for hybrid wavelength-time optical CDMA", *IEEE Photon. Technol. Lett.*, vol. 13, no. 11, pp. 1233-1235, 2001.

[28] P. C. Teh, Petropoulos, M. Ibsen and D. J. Richardson, "A comparative study of the performance of seven- and 63-chip optical code-division multiple-access encoders and decoders based on superstructured fiber Bragg gratings", *J. Lightwave Technol.*, vol. 19, no. 9, pp. 1352-1365, 2001.

[29] D. M. Spirit and M. J. O'Mahony, "High capacity optical transmission explained – BT series", *John Wiley & Sons Ltd.*, 1996.

[30] G. A. Ball and W. W. Morey, "Compression-tuned single-frequency Bragg grating fibre laser", *Opt. Lett.*, vol. 19, no. 23, pp. 1979-1981, 1994.

[31] A. Iocco, H. G. Limberger, R. P. Salathe, L. A. Everall, K. E. Chisholm, J. A. R. Williams and I. Bennion, "Bragg grating fast tunable filter for wavelength division multiplexing", *IEEE J. Lightwave Technol.*, vol. 17, no. 7, pp. 1217-1221, 1999.

[32] T. Inui, T. Komukai and M. Nakazawa, "Highly efficient tunable fibre Bragg grating filters using multilayer piezoelectric transducer", *Opt. Comm.*, vol. 190, no. 1-6, pp. 1-4, 2001.

[33] S. Y. Set, B. Dabarsyah, C. S. Goh, K. Katoh, Y. Takushima, K. Kikuchi, Y. Okabe and N. Takeda, "A widely tunable fiber Bragg grating with a wavelength tunability over 40nm", *Proc. Conference on Optical Fiber Communication (OFC)*, vol. 1, paper MC4-1, 2001.

[34] R. J. Nuyt, Y. K. Park and P. Gallion, "Dispersion equalization of a 10 Gb/s repeatered transmission system using dispersion compensating fiber", *J. Lightwave Technol.*, vol. 15, no. 1, pp. 31-42, 1997.

[35] D. Garthe, R. E. Epworth, W. S. Lee, A. Hadjifotiou, C. P. Chew, T. Bricheno, A. Fielding, H. N. Rourke, S. R. Baker, K. C. Byron, R. S. Baulcomb, S. M. Ohja and S. Clements, "Adjustable dispersion equaliser for 10 and 20 Gbit/s distances up to 160 km", *Electron. Lett.*, vol. 30, no. 25, pp. 2159-2160, 1994.

[36] D. Garthe, J. Ip, P. Colbourne, R. E. Epworth, W. S. Lee and A. Hadjifotiou, "Low-loss dispersion equaliser operable over the entire erbium window", *Electron. Lett.*, vol. 32, no. 4, pp. 371-373, 1996.

[37] K. Takiguchi, K. Okamoto and K. Moriwaki, "Planar Lighwave Circuit Dispersion Equalizer", *IEEE J. Lightwave Technol.*, vol. 14, no. 9, pp. 2003-2011, 1996.

[38] M. Shiraki, "Chromatic-dispersion compensator using virtually imaged phase array", *IEEE Photon. Technol. Lett.*, vol. 9, no. 12, pp. 1598-1600, 1997.

[39] A. H. Gnauck, R. M. Jopson, P. P. Iannone and R. M. Derosier, "Transmission of two wavelength-multiplexed 10 Gb/s channels over 560 km of dispersive fibre", *Electron. Lett.*, vol. 30, no. 9, pp. 727-728, 1994.

[40] J. H. Winters and R. D. Gitlin, "Electrical Signal Processing Techniques in Long-Haul Fiber-Optic Systems", *IEEE Trans. Commun.*, vol. 38, no. 9, pp. 1439-1453, 1990.

[41] F. Ouellette, "Dispersion cancellation using linearly chirped Bragg grating filters in optical waveguides", *Opt. Lett.*, vol. 12, no. 10, pp. 847-849, 1987.

[42] A. H. Gnauck, L. D. Garrett, F. Forghieri, V. Gusmeroli and D. Scarano, "8x20 Gbit/s 315-km, 8x10 Gbit/s 480km WDM transmission over conventional fiber using multiple broad-band fiber gratings", *IEEE Photon. Technol. Lett.*, vol. 10, no. 10, pp. 1495-1497, 1998.

[43] A. Othonos and K. Kalli, "Fiber Bragg Gratings: Fundamentals and Applications in Telecommunications and Sensing", *Artech House Inc.*, 1999.

[44] R. Kashyap, "Fiber Bragg Gratings", *Academic Press*, 1999.

[45] M. Douay, W. X. Xie, T. Taunay, P. Bernage, P. Niay, P. Cordier, B. Poumellec, L. Dong, J. F. Bayon, H. Poignant and E. Delevaque, "Densification involved in the UV based photosensitivity of silica glasses and optical fibers", *J. Lightwave Technol.*, vol. 15, no. 8, 1329-1342, 1997.

[46] J. K. Sahu, M. R. Mokhtar, N. Y. Voo, D. N. Payne and M. Ibsen, "Photosensitivity in germanium-free antimony doped alumino-silicate optical fibre prepared by MCVD", *Tech. Dig. European Conference on Optical Communication (ECOC)*, paper Th3.3.5, 2004.

[47] P. J. Lemaire, R. M. Atkins, V. Mizrahi and W. A. Reed, "High-pressure H_2 loading as a technique for achieving ultrahigh UV photosensitivity and thermal sensitivity in GeO_2 doped optical fibres", *Electron. Lett.*, vol. 29, no. 13, pp. 1191-1193, 1993.

[48] J. Stone, "Interaction of hydrogen and deuterium with silica optical fibers: a review", *J. Lightwave Technol.*, vol. 5, no. 5, 712-733, 1987.

[49] F. Bilodeau, S. Malo, J. Albert, D. C. Johnson and K. O. Hill, "Photosensitization of optical fiber and silica-on silicon/silica waveguides", *Opt. Lett.*, vol. 18, no. 12, pp. 953-955, 1993.

[50] A. Yariv, "Coupled-mode theory for gided-wave optics", *IEEE J. Quantum Electron.*, vol. QE-9, pp. 919-933, 1973.

[51] T. Erdogan, "Fiber Grating Spectra", *J. Lightwave Technol.*, vol. 15, no. 8, pp. 1277-1294, 1997.

[52] J. Skaar, L. Wang and T. Erdogan, "On the Synthesis of Fiber Bragg Gratings by Layer Peeling", *IEEE J. Quantum Electron.*, vol. 37, no. 2, pp. 165-173, 2001.

[53] http://mathworld.wolfram.com/DiscreteFourierTransform.html

[54] G. Meltz, W. W. Morey and W. H. Glen, "Formation of Bragg gratings in optical fibers by a transverse holographic method", *Opt. Lett.*, vol. 14, no. 15, pp. 823-825, 1989.

[55] K. O. Hill, B. Malo, F. Bilodeau, D. C. Johnson and J. Albert, "Bragg gratings fabricated in monomode photosensitive optical fibre by UV exposure through a phase mask", *App. Phys. Lett.*, vol. 62, no. 25, pp. 1035-1037, 1993.

[56] D. Z. Anderson, V. Mizrahi, T. Erdogan and A. E. White, "Production on in-fibre gratings using a diffraction optical element", *Electron. Lett.*, vol. 29, no. 6, pp. 566-568, 1993.

[57] C. Palmer, "Diffraction Gratings Handbook", *Thermo RGL*, 2002.

[58] http://www.ibsen.dk/ibsen/phasemas.nsf

[59] M. Ibsen, M. K. Durkin, M. J. Cole, M. N. Zervas and R. I. Laming, "Recent advances in long dispersion compensating fiber Bragg gratings", *IEE Colloquium on Optical Fibre Gratings (ref. no. 1999/023)*, pp. 6/1-6/7, 1999.

[60] R. Feced and M. Zervas, "Effects of Random Phase and Amplitude Errors in Optical Fiber Bragg Gratings", *J. Lightwave Technol.*, vol. 18, no. 1, pp. 90-101, Jan 2000.

[61] M. L. Rocha and R. Kashyap, "Characterisation of fibre Bragg gratings: a study of accuracy and repeatability", *Proc. Optical Fiber Measurement Conference (OFMC)*, pp. 14-17, 1997.

[62] S. Barcelos, M. N. Zervas, R. I. Laming and D. N. Payne, "Interferometric fibre grating characterization", *IEE Colloquium on Optical Fibre Gratings and their Applications*, pp. 5/1-5/7, 1995.

[63] B. F. Ventrudo, G. A. Rogers, G. S. Lick, D. Hargreaves and T. N. Demayo, "Wavelength and intensity stabilization of 980 nm diode lasers coupled to fiber Bragg gratings", *Electron. Lett.*, vol. 30, no. 25, pp. 2147-2149, 1994.

[64] J. L. Zyskind, J. W. Sulhoff, P. D. Magill, K. C. Reichmann, V. Mizrahi and D. J. DiGiovanni, "Transmission at 2.5 Gbits/s over 654 km using an erbium-doped fiber grating laser source", *Electron. Lett.*, vol. 29, no. 12, pp. 1105-1106, 1993.

[65] J. Chow, G. Town, B. Eggleton, M. Ibsen, K. Sugden and I. Bennion, "Multi-wavelength generation in an erbium-doped fiber laser using in-fiber comb filters", *IEEE Photon. Technol. Lett.*, vol. 8, no. 1, pp. 60-62, 1996.

[66] W. H. Loh and R. I. Laming, "1.55 μm phase-shifted distributed feedback fiber laser", *Electron. Lett.*, vol. 31, pp. 1440-1442, 1995.

[67] S. G. Grubb, T. Strasser, W. Y. Cheung, W. A. Reed, V. Mizrahi, T. Erdogan, P. J. Lemaire, A. M. Vengsarkar and D. J. DiGiovanni, "High power 1.48 μm cascaded Raman laser in germanosilicate fibers", *Proc. Optical Amplifiers and Their Applications (OAA)*, paper SaA4, pp. 197-199, 1995.

[68] C. R. Giles, J. Stone, L. W. Stulz, K. Walker and C. A. Burrus, "Gain enhancement in reflected-pump erbium-doped fiber amplifiers", *Proc. Optical Amplifiers and Their Applications (OAA)*, vol. 13, paper ThD2, pp. 148-151, 1991.

[69] C. R. Giles and V. Mizrahi, "Low-loss add/drop multiplexers for WDM lightwave networks", *Proc. Conference on Integrated Optics and Optical Fiber Communication (IOOC)*, paper ThC2-1, 1995.

[70] F. Bilodeau, D. C. Johnson, S. Theriault, B. Malo, J. Albert and K. O. Hill, "An all-fiber dense wavelength division multiplexer/demultiplexer using photo-imprinted Bragg gratings", *IEEE Photon. Technol. Lett.*, vol. 7, no. 4, pp. 388-390, 1995.

[71] V. Mizrahi, T. Erdogan, D. J. DiGiovanni, P. J. Lemaire, W. M. MacDonald, S. G. Kosinski, S. Cabot and J. E. Sipe, "Four channel fiber grating demultiplexer", *Electron. Lett.*, vol. 30, no. 10, pp. 780-781, 1994.

[72] B. J. Eggleton, T. Stephens, P. A. Krug, G. Dhosi, Z. Brodzeli and F. Ouellette, "Dispersion compensation using a fiber grating in transmission", *Electron. Lett.*, vol. 32, no. 17, pp. 1610-1611, 1996.

[73] C. R. Giles, V. Mizrahi and T. Erdogan, "Polarization-independent phase conjugation in a reflective optical mixer", *IEEE Photon. Technol. Lett.*, vol. 7, no. 1, pp. 126-128, 1995.

[74] R. Giles and S. Jiang, "Fiber-grating sensor for wavelength tracking in single-fiber WDM access PON's", *IEEE Photon. Technol. Lett.*, vol. 9, no. 4, pp. 523-525, 1997.

[75] R. Giles, M. Zirngibl, T. Strasser, C. Joyner and L. Stulz, "Wavelength Conversion in a 1550 nm multifrequency laser", *IEEE Photon. Technol. Lett.*, vol. 9, no. 1, pp. 43-45, 1997.

[76] F. A. Flood, "L-band erbium-doped fiber amplifiers", *Proc. Conference on Optical Fiber Communication (OFC)*, vol. 2, pp. 10.2-104, 2000.

[77] L. Poladian, "Graphical and WKB analysis of nonuniform Bragg gratings", *Phys. Rev. E*, vol. 48, no. 6, pp. 4758-4767, 1993.

[78] R. K. Staubli and P. Gysel, "Crosstalk Penalties due to Coherent Rayleigh Noise in Bidirectional Optical Communication Systems", *J. Lightwave Technol.*, vol. 9, no. 3, pp. 375-380, 1991.

[79] M. Begin, J. Lauzon, Y. Rouleau and Y. Mimeault, "Gain-locked dual-stage EDFA for WDM systems", *Proc. Optical Amplifiers and Their Applications (OAA)*, pp. 148-151, 2000.

[80] M. Zirngibl, "Gain control in Erbium-doped fiber amplifiers by an all-optical feedback loop", *Electron. Lett.*, vol. 27, no. 7, pp. 560-561, 1991.

[81] R. I. Laming, J. D. Minelly, L. Dong and M. N. Zervas, "Twincore erbium-doped fibre amplifier with passive spectral gain equalisation", *Electron. Lett.*, vol. 29, no. 6, pp. 509-510, 1993.

[82] L. Eskildsen, E. L. Goldstein, G. K. Chang, M. Z. Iqbal and C. Lin, "Self-regulating WDM amplifier module for scalable lightwave networks", *IEEE Photon. Technol. Lett.*, vol. 6, no. 11, pp. 1321-1323, 1994.

[83] E. L. Goldstein, L. Eskildsen, V. da Silva, M. Andrejco and Y. Silberberg, "Inhomogeneously broadened fiber-amplifier cascades for transparent multiwavelength lightwave networks", *J. Lightwave Technol.*, vol. 13, no. 5, pp. 782-790, 1995.

[84] http://www.spioptics.com/gain_spectfbgs.htm

[85] P. C. Teh, M. Ibsen, J. H. Lee, P. Petropoulos and D. J. Richardson, "A 4-channel WDM/OCDMA system incorporating 255-chip 320 Gchip/s quaternary phase coding and decoding gratings", *Proc. Conference on Optical Fiber Communication (OFC)*, vol. 4, paper PD37-1, 2001.

[86] E. H. Dinan and B. Jabbari, "Spreading codes for Direct Sequence CDMA and Wideband CDMA Cellular Networks", *IEEE Communications Magazine*, vol. 36, pp. 48-54, 1998.

[87] M. Ibsen, S. Y. Set, G. S. Goh and K. Kikuchi, "Broad-band continuously tunable all-fiber DFB lasers", *IEEE Photon. Technol. Lett.*, vol. 14, no. 1, pp. 21-23, 2002.

[88] P. P. Benham, R. J. Crawford and C. G. Armstrong, "Mechanics of Engineering Materials", *Addison Wesley Longman Ltd.*, 1998.

[89] http://www.sosmath.com/diffeq/second/constantcof/constantcof.html

[90] W. H. Loh, M. J. Cole, M. N. Zervas, S. Barcelos and R. I. Laming, "Complex grating structures with uniform phase masks based on the moving fiber-scanning beam technique", *Opt. Lett.*, vol. 20, no. 20, pp. 2051-2053, 1995.

[91] http://www.heraeus-amersil.com/HQS1/ENG/HQT/hqt_home.nsf/$frameset/Quarzglas1st

[92] L. B. Fu, M. Ibsen, M. R. Mokhtar, M. Gunning, D. J. Richardson and D. N. Payne, "Wideband compression-tuned all-fibre DFB laser: analysis and characterisation", *Proc. Conference on Optical Fiber Communication (OFC)*, vol. 1, pp. 235-237, 2003.

[93] M. Ibsen, E. Ronnekleiv, G. J. Cowle, M. O. Berendt, O. Hadeler, M. N. Zervas and R. I. Laming, "Robust high power (>20 mW) all-fibre DFB lasers with unidirectional and truly single polarisation outputs", *Proc. Conference on Lasers and Electro-Optics (CLEO)*, pp. 245-246, 1999.

[94] J. K. Sahu, Y. Jeong, C. Codemard, J. Nilsson, M. R. Mokhtar, M. Ibsen, D. J. Richardson and D. N. Payne, "Tunable narrow linewidth high power erbium:ytterbium co-doped fiber laser", *Proc. Conference on Lasers and Electro-Optics (CLEO)*, paper CMK, 2004.

[95] P. J. Almeida, P. Petropoulos, M. Ibsen, M. R. Mokhtar, B. C. Thomsen and D. J. Richardson, "All-optical TDM add-drop multiplexer based on

Time to Wavelength conversion", *Tech. Dig. European Conference on Optical Communication (ECOC)*, paper We3.5.5, 2004.

[96] P. J. Almeida, P. Petropoulos, J. H. Lee, B. C. Thomsen, M. Ibsen and D. J. Richardson, "Optical Packet Compression in fibres based on time lens and solitonic effects", *IEEE Photon. Technol. Lett.*, vol. 16, no. 7, pp. 1688-1690, 2004.

[97] M. R. Mokhtar, C. S. Goh, S. A. Butler, S. Y. Set, K. Kikuchi, D. J. Richardson and M. Ibsen, "Fibre Bragg grating compression-tuned over 110 nm", *Electron. Lett.*, vol. 39, no. 6, pp. 509-511, 2003.

[98] A. S. Stephen, C. B. Paul, D. B. Dwight, L. B. Collin and K. A. Dave, "An elastic, low-background vertical focusing element for a doubly focusing neutron monochromator", *Nucl. Instr. and Meth. A*, vol. 466, pp. 513-526, 2001.

[99] M. Schiess, "Extension of the dispersion limit by pulse shaping and profiting of fibre nonlinearities", *Tech. Dig. European Conference on Optical Communication (ECOC)*, pp. 423-426, 1994.

[100] B. F. Jorgensen, "Unrepeated transmission at 10 Gbit/s over 204 km standard fiber", *Tech. Dig. European Conference on Optical Communication (ECOC)*, pp. 685-688, 1994.

[101] B. Wedding, B. Franz and B. Junginger, "10 Gb/s optical transmission up to 253 km via standard single-mode fiber using the method of dispersion-supported transmission", *J. Lightwave Technol.*, vol. 12, no. 10, pp. 1720-1727, 1994.

[102] A. J. Price and N. Le Mercier, "Reduced bandwidth optical digital intensity modulation with improved chromatic dispersion tolerance", *Electron. Lett.*, vol. 31, no. 1, pp. 58-59, 1995.

[103] N. Takachio, S. Norimatsu and K. Iwashita, "Optical PSK Synchronous Heterodyne Detection Transmission Experiment Using Fiber Chromatic Dispersion Equalization", *IEEE Photon. Technol. Lett.*, vol. 4, no.3, pp. 278-280, 1992.

[104] M. Durkin, M. Ibsen, M. J. Cole and R. I. Laming, "1 m long continuously-written fibre Bragg gratings for combined second- and third-order dispersion compensation", *Electron. Lett.*, vol. 33, no. 22, pp. 1891-1893, 1997.

[105] A. Ghatak and K. Thyagarajan, "Introduction to Fiber Optics", *Cambridge University Press*, 2000.

[106] T. Komukai, T. Inui and M. Nakazawa, "The Design of Dispersion Equalizers Using Chirped Fiber Bragg Gratings", *J. Lightwave Technol.*, vol. 36, no. 4, pp. 409-417, 2000.

[107] K. Hinton, "Dispersion Compensation Using Apodized Bragg Fiber Gratings in Transmission", *J. Lightwave Technol.*, vol. 16, no. 12, pp. 2336-2346, 1998.

[108] J. J. Veselka and S. K. Korotky, "Pulse Generation for Soliton Systems Using Lithium Niobate Modulators", *IEEE J. Sel. Top. Quantum Electron.*, vol. 2, no. 2, pp. 300-310, 1996.

[109] N. S. Bergano, F. W. Kerfoot and C. R. Davidson, "Margin Measurements in Optical Amplifier Systems", *IEEE Photon. Technol. Lett.*, vol. 5, no. 3, pp. 304-306, 1993.

[110] A. D. McCoy, B. C. Thomsen, M. Ibsen and D. J. Richardson, "Filtering Effects in a Spectrum-Sliced WDM System Using SOA-Based Noise Reduction", *IEEE Photon. Technol. Lett.*, vol. 16, no. 2, pp. 680-682, 2003.

[111] N. S. Bergano and C. R. Davidson, "Circulating Loop Transmission Experiments for the Study of Long-Haul Transmission Systems Using Erbium-Doped Fiber Ampflifiers", *J. Lightwave Technol.*, vol. 13, no. 5, pp. 879-888, 1995.

List of Publications

Journals

[1] M. R. Mokhtar, M. Ibsen, P. C. Teh and D. J. Richardson, "Reconfigurable Multi-level Phase Shift Keying Encoder/Decoder for All-optical Networks", *IEEE Photon. Technol. Lett.*, vol. 15, no. 3, pp. 431-433, 2003.

[2] C. S. Goh, M. R. Mokhtar, S. A. Butler, Sze Y. Set, Kazuro Kikuchi and Morten Ibsen, "Accurate Tuning of Fiber Bragg Gratings over 90 nm Using a Simple Set-and-Forget Package Configuration", *IEEE Photon. Technol. Lett.*, vol. 15, no. 4, pp. 557-559, 2003

[3] M. R. Mokhtar, C. S. Goh, S. A. Butler, S. Y. Set, K. Kikuchi, D. J. Richardson and M. Ibsen, "Fibre Bragg grating compression-tuned over 110 nm", *IEE Electron. Lett.*, vol. 39, no. 6, pp. 509-511, 2003.

[4] Y. Jeong, C. Alegria, J. K. Sahu, L. Fu, M. Ibsen, C. Codemard, M. R. Mokhtar, and J. Nilsson, "A 43 W C-band tunable narrow-linewidth erbium-ytterbium co-doped large-core fiber laser", *IEEE Photon. Technol. Lett.*, vol. 16, no. 3, pp. 756-758, 2004.

[5] A. D. McCoy, P. Horak, B. C. Thomsen, M. Ibsen, M. R. Mokhtar and D. J. Richardson, "Improving Signal Quality in a Spectrum-Sliced WDM System Using SOA-Based Noise Reduction", *IEEE Photon. Technol. Lett.*, vol. 17, no. 1, pp. 241-243, 2005.

Conferences

[1] M. R. Mokhtar, M. Ibsen, P. C. Teh and D. J. Richardson, "Simple dynamically reconfigurable OCDMA encoder/decoder based on a uniform

fiber Bragg grating", *Proc. Conference on Optical Fiber Communication (OFC)*, paper ThGG54, pp. 688-690, 2002.

[2] M. R. Mokhtar, M. Ibsen, S. A. Butler, S. Y. Set, D. J. Richardson and D. N. Payne, "Bragg Grating Package for Simple Broad-range Tuning", *Tech. Dig. European Conference on Optical Communication (ECOC)*, paper 7.2.3, 2002.

[3] M. R. Mokhtar, M. Ibsen, P. C. Teh and D. J. Richardson, "16-bit multilevel reconfigurable phase encoder for all optical header generation/recognition based on a Uniform Fibre Bragg Grating", *Proc. Optoelectronics and Communications Conference (OECC)*, paper PD-2-2 (Postdeadline), 2002.

[4] C. S. Goh, M. R. Mokhtar, S. A. Butler, S. Y. Set, K. Kikuchi and M. Ibsen, "Over 70 nm Wideband Tuning of Fiber Bragg Gratings Using a Compressive Bending Technique", *Proc. Optoelectronics and Communications Conference (OECC)*, paper PD-2-1 (Postdeadline), 2002.

[5] M. Ibsen, R. Feced, P. C. Teh, J. H. Lee, M. R. Mokhtar, P. Petropoulos, M. N. Zervas, D. J. Richardson and D. N. Payne, "Advanced fibre Bragg gratings and where they are going", *AIP-ACOFT*, (Invited), 2002.

[6] C. S. Goh, M. R. Mokhtar, S. A. Butler, S. Y. Set, K. Kikuchi and M. Ibsen, "Greater Than 90nm Continuously Wavelength-tunable Fibre Bragg Gratings", *Proc. Conference on Optical Fiber Communication (OFC)*, 2003.

[7] L. B. Fu, M. Ibsen, M. R. Mokhtar, M. Gunning, D. J. Richardson and D. N. Payne, "Wideband compression-tuned all-fibre DFB laser: analysis and characterisation", *Proc. Conference on Optical Fiber Communication (OFC)*, vol. 1, pp. 235-237, 2003.

[8] P. C. Teh, M. R. Mokhtar, M. Ibsen and D. J. Richardson, "A novel distributed OCDMA architecture based on simultaneous transmission of 16-chip OCDMA signals and clock pulses", *Proc. Conference on Optical Fiber Communication (OFC)*, 2003.

[9] C. S. Goh, M. R. Mokhtar, S. A. Butler, S. Y. Set, K. Kikuchi, M. Ibsen, "Widely tunable fibre Bragg grating filters", *Proc. Rank Prize Funds minisymposium: Passive Optical Components*, 2003.

[10] M. R. Mokhtar, S. A. Butler, D. J. Richardson and M. Ibsen, "Effects of large compressive-stresses on photosensitive optical fibres and Bragg gratings", *Proc. Bragg Gratings, Photosensitivity and Poling Glass Waveguides (BGPP)*, paper WA3, 2003.

[11] M. Ibsen, J. Nilsson, L. Fu, Y. Jeong, J. K. Sahu, M. R. Mokhtar, C. Alegria and D. N. Payne, "All-fibre Bragg grating filters and lasers for future optical networks", *Proc. ICICS-PCM 2003*, (Invited), 2003.

[12] J. K. Sahu, Y. Jeong, C. Codemard, J. Nilsson, M. R. Mokhtar, M. Ibsen, D. J. Richardson, and D. N. Payne, "Tunable narrow linewidth high power erbium:ytterbium co-doped fiber laser", *Proc. Conference on Lasers and Electro-Optics (CLEO)*, paper CMK, 2004.

[13] C. Alegria, Y. Jeong, C. Codemard, J. K. Sahu, L. Fu, M. R. Mokhtar, M. Ibsen, S. Baek, D. B. S. Soh, V. Philippov and J. Nilsson, "Wideband tunable high power narrow linewidth erbium-ytterbium doped fiber laser using compression-tunable fiber Bragg grating", *SPIE Proc. 5335-43 Photonics West*, pp. 229, 2004.

[14] P. J. Almeida, P. Petropoulos, M. Ibsen, M. R. Mokhtar, B. C. Thomsen and D. J. Richardson, "All-optical TDM add-drop multiplexer based on Time to Wavelength conversion", *Tech. Dig. European Conference on Optical Communication (ECOC)*, paper We3.5.5, 2004.

[15] A. D. McCoy, P. Horak, B. C. Thomsen, M. R. Mokhtar and D. J. Richardson, "Optimising signal quality in a spectrum-sliced WDM system using SOA-based noise reduction", *Tech. Dig. European Conference on Optical Communication (ECOC)*, paper Tu4.6.4, 2004.

[16] J. K. Sahu, M. R. Mokhtar, N. Y. Voo, D. N. Payne and M. Ibsen, "Photosensitivity in germanium-free antimony doped alumino-silicate optical fibre prepared by MCVD", *Tech. Dig. European Conference on Optical Communication (ECOC)*, paper Th3.3.5, 2004.